

# **Sensing and Actuation in Electroactive Elastomeric Bodies**

by

Richard James Morrin Ellingham

A thesis submitted for the degree of  
Doctor of Philosophy

in

Mechanical Engineering

at the

**UNIVERSITY OF CANTERBURY**

September 2024

# Declaration of Authorship

I, AUTHOR NAME, declare that this thesis titled, 'Sensing and Actuation in Electroactive Elastomeric Bodies' and the work presented in it are my own. I confirm that:

- This work was done wholly or mainly while in candidature for a research degree at this University.
- Where any part of this thesis has previously been submitted for a degree or any other qualification at this University or any other institution, this has been clearly stated.
- Where I have consulted the published work of others, this is always clearly attributed.
- Where I have quoted from the work of others, the source is always given. With the exception of such quotations, this thesis is entirely my own work.
- I have acknowledged all main sources of help.
- Where the thesis is based on work done by myself jointly with others, I have made clear exactly what was done by others and what I have contributed myself.

Signed:

---

Date:

---

*“When do you think you can submit your thesis?”*

T. Giffney, April 2024

*“Today.”*

R. Ellingham, September 2024

UNIVERSITY OF CANTERBURY

*Abstract*

College of Engineering  
Mechanical Engineering

Doctor of Philosophy

by Richard James Morrin Ellingham

Some of the world's most advanced technology is rigid due to various factors such as; manufacturability, miniaturisability, physical linearity, and more ideal physics in general. In parallel industries is also looking to use automation to improve and replace laborious tasks whether they be domestic, commercial, or industrially related tasks. There is a growing need for new innovations in technology to utilise the soft robotic solutions that mimic biological solutions seen in nature. This thesis is part of many to improve an understanding of the electroactive polymer subset of soft robotics and the limitations of specific implementations of artificial skin and artificial muscle technologies.

This thesis explores the integration of Electrical Impedance Tomography (EIT) with advanced soft sensing technologies, focusing on carbon black silicone rubber (CBSR) elastomer composites and Dielectric Elastomer Actuators (DEAs) to enhance pressure mapping, strain sensing, and actuation.

CBSR elastomer composites, noted for their high stretchability and biocompatibility, were investigated to understand their resistance relaxation behavior. This research contributes to optimizing the design of flexible dynamic strain sensors by modeling the response of resistance to transient strain inputs. The study developed an EIT-based pressure mapping system using a silicone CB nanoparticle sensing domain that mimics pressure mapping qualities human skin. This system was evaluated for its spatial and temporal resolution, showing potential for creating artificial pressure-sensitive skin with practical applications. Furthermore, the integration of EIT with DEAs was examined to improve the mapping of compressive forces across electrode surfaces. Despite some trade-offs in accuracy due to electrode compliance, this approach offers promising advancements for applications requiring precise actuation and pressure mapping. This work has majorly contributed towards filing a patent for an DEA-EIT actuator-sensor device. Additionally, the research uncovered unintentional power generation in DEAs, which could function as Dielectric Elastomer Generators (DEGs) due to mechanical strain. This finding highlights the dual functionality of DEAs and suggests opportunities for energy harvesting applications. Finally, a portable, low-cost EIT-based hardware system for pressure mapping was introduced. This system enables comprehensive characterization of various sensing domains and supports advancements in EIT-based soft sensor technology, with implications for biomedical devices, robotics, and energy harvesting.

Overall, this research advances the field of soft sensors by integrating EIT with innovative materials and technologies, providing new insights and applications in dynamic sensing and actuation.

## *Acknowledgements*

People to thank:

- UC Bioengineering office - Lung lads, Lung Ladies, IPC, Hamish for infinite beers, Nic's abstract art.
- Geoff Chase - for a constant stream of stories and advice always within earshot.
- Other office - for ping pong madness, bikkies and fruit.
- Supervisor Tim - for time, money, lack of time, and support on a project that slightly diverged from his research till the end.
- Co-supervisors Chris, and late comer Lui - for advice and casual yarns.
- Summer students Toby and Yeni - for great work towards my PhD topic.
- UC mechanical and electrical department technicians (Julian Murphy, Julian Phillips, Tony Doyle, Scott Lloyd, amongst others) - for general support and yarns throughout my maddness.
- Juan Jose and Anastasia at IMDEA Materiales - for help with me going down a wonderful materials science rabbit hole.
- Markus Vorrath and co. at TU Dresden - for giving me a home to type out words and a group to discuss soft robotics with.
- Johannes Mersch - For helping with some final (hopefully groundbreaking) experiments when I was in strife towards the end of my PhD.
- Tess - for general oddities, support, and love.
- Friends - for constantly questioning "so when are you finishing again?"
- Family - for being supportive.

# Contents

<b>Declaration of Authorship</b>	i
<b>Abstract</b>	iii
<b>Acknowledgements</b>	v
<b>List of Figures</b>	viii
<b>List of Tables</b>	x
<b>Abbreviations</b>	xi
<b>Symbols</b>	xii
<b>1 Introduction and Motivation</b>	1
1.1 Why Go Soft and Not Rigid? . . . . .	1
1.2 Research Objectives . . . . .	2
1.3 Chapter Contributions . . . . .	3
<b>2 Literature Review</b>	4
2.1 Biological Skin form and function . . . . .	4
2.1.1 Skin Construction and Types . . . . .	6
2.1.2 Characterising skin . . . . .	7
2.1.3 Skin Modelling . . . . .	9
2.2 Pressure Mapping Artificial Skin Devices . . . . .	9
2.2.1 Soft Pressure mapping technology . . . . .	9
2.2.1.1 Resistive . . . . .	10
2.2.1.2 Capacitive . . . . .	10
2.2.1.3 Magnetic . . . . .	11
2.2.1.4 Optical . . . . .	11
2.2.1.5 Acoustic . . . . .	11
2.2.1.6 Soft Pressure mapping technology comparison . . . . .	11
2.3 Biological Muscle form and function . . . . .	13
2.3.1 Characterising a muscle . . . . .	13
2.3.2 Muscle Mechanics . . . . .	15
2.3.3 Electrical Muscle Models . . . . .	16

2.4	Artificial Muscle Technology . . . . .	16
2.4.0.1	Ionic polymer–metal composite actuator . . . . .	16
2.4.0.2	HASEL actuator . . . . .	17
2.4.0.3	Dielectric Elastomer Actuators . . . . .	19
2.4.0.4	Magnetorheological Elastomer . . . . .	20
2.5	Soft Conductive Particle Piezoresistive Composites . . . . .	21
2.5.1	Fabricating Conductive Particle Elastomer Composites . . . . .	21
2.5.2	Conductive Particle Elastomer Conduction Mechanisms . . . . .	22
2.6	Literature Review Conclusions . . . . .	25
<b>3</b>	<b>Characterising Non-Linear Behaviour in Carbon-Black Conductive Particle Elastomer Composites</b>	<b>26</b>
3.1	Introduction . . . . .	27
3.1.1	Background . . . . .	27
3.2	Methods . . . . .	29
3.2.1	Composite Fabrication . . . . .	29
3.2.2	Material Imaging . . . . .	30
3.2.3	Stress-Strain-Resistance Measurement . . . . .	32
3.3	Results and Analysis . . . . .	34
3.3.1	Stress-Strain and Viscoelasticity . . . . .	35
3.3.2	Quasi-Static Tensile Resistance-Strain . . . . .	35
3.3.3	Dynamic Resistance-Strain-Rate Response . . . . .	36
3.3.4	Falling Edge Strain-Rate-Resistance . . . . .	37
3.3.5	Resistive Relaxation Fitting . . . . .	40
3.3.6	Resistance-Stress Relationship . . . . .	42
3.4	Discussion . . . . .	43
3.4.1	Fabrication . . . . .	44
3.4.2	Quasi-static Tensile Resistance-Strain . . . . .	44
3.4.3	Dynamic Resistance-Strain-Rate Response . . . . .	44
3.4.4	Falling Edge Strain-Rate-Resistance . . . . .	44
3.4.5	Resistive Relaxation Fitting . . . . .	45
3.4.6	Resistance-Stress Relationship . . . . .	45
3.4.7	Viscoelasticity . . . . .	45
3.4.8	Repeatability . . . . .	45
3.4.9	Further Discussion and Future Work . . . . .	46
3.5	Conclusions . . . . .	47
<b>A</b>	<b>Thesis Crossword</b>	<b>49</b>
<b>B</b>	<b>Strain-Stress-Resistance Experiments</b>	<b>50</b>
<b>C</b>	<b>Chapter Title</b>	<b>52</b>
<b>Bibliography</b>		<b>53</b>

# List of Figures

2.1 Examples of the locations of proprioceptors and cutaneous mechanoreceptors in the human body. . . . .	5
2.2 Clockwise from top left: IMU pose estimation[1] (© 2022 MDPI), stretch sensor knee joint pose estimation[2] (© 2020 IEEE), encoder elbow pose joint estimation[3], stretch sensor hand joint pose estimations[4]. . . . .	5
2.3 Various pressure mapping devices. From top-left then clockwise: XSsensor wheelchair pressure mapping sheet (© 2024 XSENSOR® Technology)[5], Pressure Profile Systems pressure sensors on a robotic hand (© 2023 PPS UK limited)[6], Soft pressure mapping gripper(© 2023 PowerON)[7], Tekscan thin pressure mapping platform[8](© 2024 Tekscan Inc.), Tactilus seat pressure mapping system[9](© 2024 Sensor Products Inc.) . . . . .	6
2.4 Two grey electrodes across a blue dielectric medium. Left: Uncompressed state. Right: Compressed state exhibiting larger electrode areas and a thinner dielectric thickness. . . . .	10
2.5 Components of a biological muscle contractile unit and meta-structure. . . . .	13
2.6 Stress and strain of active and passive muscles (© J. Teran   ACM 2003)[10] . . .	15
2.7 Diagram of the typical architecture of an IPMC actuator[11] (© 2018 Yanjie Wang and Takushi Sugino) . . . . .	17
2.8 Diagram of the typical architecture and the contraction stages of a HASEL actuator[12] . . . . .	18
2.9 Diagram of the simplified stages of HASEL actuator production[12] . . . . .	18
2.10 DEA with two compliant light-grey electrodes and a transparent light blue dielectric elastomer. Showing deformation without and with a voltage applied across the electrodes. . . . .	19
2.11 Diagram showing MRE contraction actuation when a magnetic field is applied[13]	21
2.12 Two grey highly conductive electrodes across a CPEC cuboid showing enlarged black conductive particles within a blue polymer matrix. Left: An uncompressed CPEC. Right: A compressed CPEC. . . . .	22
2.13 Example of a randomised cube percolation with a volume percentage of 8% of $1\mu\text{m}$ particles . . . . .	23
2.14 Electrical conduction and tunneling representation diagram. . . . .	23
2.15 AC conduction RC network representation diagram. . . . .	24
3.1 Mechanical spring dashpot diagram of the generalised Maxwell body model adapted from Fung et al. [14] . . . . .	28
3.2 The steps involved in creating the CBSR composite material . . . . .	29
3.3 Microscope images at x20 magnification of a CBSR specimens with cross-sections made by; Left: Cutting with a scalpel. Right: Inducing an embrittlement fracture. .	30
3.4 SEM images of; (A): CB agglomerated particles $\times 40,000$ . (B): CBSR cross-section top surface edge site 1 $\times 250$ . (C): CBSR cross-section site 1 $\times 2000$ . . .	31

3.5 (A): Typical screenshot from the focused Raman microscope. Normalised Raman spectrum of (B) the plain SR. (C) the top surface of CBSR specimen. (D) the cross-sectional surface of CBSR specimen. . . . .	32
3.6 The composite dog-bone test specimen pierced by 4 metal pin electrodes. The outer and inner electrodes connected to an SMU current source and voltmeter respectively . . . . .	33
3.7 Photo of test measurement setup . . . . .	33
3.8 System architecture for the electromechanical tensile test rig showing data/physical connections . . . . .	34
3.9 The loading and unloading of 30% strain on a composite test specimens with CB weight percentages from top to bottom of 10%, 7.5%, and 0% with data collected over five loading and unloading cycles . . . . .	35
3.10 Linear quasi-static resistance-strain fit for 7.5 w.t.% CBSR specimen . . . . .	36
3.11 Strain input waveform for investigating strain-rate dependent resistance . . . . .	36
3.12 Resistance response from saw-tooth strain input Figure 3.11. . . . .	37
3.13 Resistance vs strain hysteresis loops from from a saw-tooth strain input. . . . .	37
3.14 Left: Singluar tensile strain pulse with resulting stress and resistance reponse. Right: Zoomed to higlight falling edge shoulder phenomena. . . . .	38
3.15 Strain-rate resistance relationship showing the specimen returning to a 0% tensile strain state from 10% at a strain-rate of $3.33\%\cdot s^{-1}$ from four tests for a 7.5% CBSR specimen . . . . .	39
3.16 Fitting curves to a range of different tensile falling edge strain strain-rates. . . . .	39
3.17 Comparing the relaxation decay time constants of stress and resistance for a 7.5 w.t.% CBSR composite after a 10% strain step input and fitting generalised maxwell body models to each. . . . .	41
3.18 Comparing resistance and stress relaxation data against each other occurring during 30 pulses of a 10% strain step input for a 7.5 w.t.% CBSR composite . . . . .	43
3.19 A typical test sequence of a 30 pulse strain train recording the calculated resistance and stress of a 7.5 w.t.% CBSR composite . . . . .	46
3.20 Three identical 15% strain pulses at three different current values ,in order, $10\mu A$ , $15\mu A$ , and $20\mu A$ . . . . .	47
B.1 Strain test sequence showing the shoulder phenomena correlation for varying magnitudes of strain for a 7.5 wt% CBSR specimen dogbone sample. This experiment had an unintentional offset of 1 mm, hoever this showed a drastic decrease shoulder phenomena when the falling edge is crossing the x-axis. . . . .	50
B.2 Strain test sequence showing the shoulder phenomena correlation for varying magnitudes of strain for a 7.5 wt% CBSR specimen dogbone sample. This experiment used DC measurements, so the macro downward trend in resistance is more obvious than other experimental data given in this work with used a switched AC signal. . . . .	51
B.3 AC vs DC downward trend in resistance for an unstrained 7.5 wt% CBSR composite dogbone specimen. . . . .	51

# List of Tables

2.1	Comparison of typical mammalian mechanoreceptor characteristics [15]. . . . .	7
2.2	Comparison of different potential piezo-resistive sensor materials. Ranked 1 to 5, where 1 is desirable and 5 is undesirable. WIP - need to redo properly and find a reference for each box! . . . . .	10
2.3	Comparison of soft sensor technologies. . . . .	12
3.1	Strain-rate dynamic resistance offset comparison. Using S1 as the reference resistance loop. . . . .	37
3.2	The fitted parameters for relationship between the specimen tensile strain-rate the resulting resistance peak for a strain signal falling edge. . . . .	40
3.3	Fitted constants and their mean, $\mu$ , standard deviation values for 0%, 7.5%, and 10% CBSR composite specimens using Equation 3.7. . . . .	41
3.4	Fitted constants and their mean, $\mu$ , and standard deviation values for 0%, 7.5%, and 10% CBSR composite specimens using Equation 3.8. . . . .	42
3.5	Fitted constants and their mean, $\mu$ , standard deviation, $\sigma$ , and coefficient of variation, $CV$ , values for 7.5%, and 10% CBSR composite specimens using Equation 3.9 . . . . .	43

# Abbreviations

<b>ADC</b>	Analog-to-Digital Converter
<b>CAD</b>	Computer Aided Design
<b>CB</b>	Carbon Black
<b>CFA</b>	Cartesian Force Applicator
<b>CE</b>	Compliant Electrode
<b>CoM</b>	Center of Mass
<b>DE</b>	Dielectric Elastomer
<b>DEA</b>	Dielectric Elastomer Actuator
<b>DEG</b>	Dielectric Elastomer Generator
<b>DUT</b>	Domain Under Test
<b>EIT</b>	Electrical Impedance Tomography
<b>ERT</b>	Electrical Resistance Tomography
<b>FEA</b>	Finite Element Analysis
<b>FEM</b>	Finite Element Modelling
<b>FPC</b>	Flexible Printed Circuit
<b>IDF</b>	IoT Development Framework
<b>MUX</b>	Multiplexer
<b>PCB</b>	Printed Circuit Board
<b>PCBA</b>	Printed Circuit Board Assembly
<b>PDMS</b>	Polydimethylsiloxane (AKA silicone)
<b>PNEC</b>	Piezoresistive Nanoparticle Elastomer Composite
<b>SMU</b>	Source Measure Unit
<b>SMD</b>	Surface-Mount Device
<b>SR</b>	Silicone Rubber
<b>THT</b>	Through-Hole Technology
<b>EAP</b>	Electro-Active Polymer

# Symbols

$A$	Area	[m <sup>2</sup> ]
$C$	Capacitance	[F]
$\epsilon_0$	Vacuum Permittivity	[Fm <sup>-1</sup> ]
$\epsilon_r$	Relative Permittivity	[a.u.]
$K$	Bulk Modulus	[Pa]
$\nu$	Poisson's Ratio	[a.u.]
$Q$	Electrical Charge	[C]
$U_E$	Electrical Potential Energy	[J]
$U_\epsilon$	Elastic Potential Energy	[J]
$R$	Resistance	[\Omega]
$\sigma$	Stress	[Pa]
$S$ or $\epsilon$	Strain	[a.u. or %]
$\dot{\epsilon}$	Strain Rate	[%s <sup>-1</sup> ]
$V$	Voltage	[V]
$Y$ or $E$	Young's Modulus	[Pa]
$z$	Thickness	[m]

*Dedicated to tinned baked beans in all their glory... .*

# Chapter 1

## Introduction and Motivation

Rigid robotic systems often have multiple rotary motors and various sensors integrated together for precise control of the robot, this is mirrored in biology with the animals having many actuator units in the form of muscles and a multitude of various receptors for sensing their environment. The rigidity of rotational motors is stifling creativity in the creation and development of devices amongst many other unforeseen future technology. Engineers are often constrained to solving problems and designing solutions using typical rigid sensors and actuators due to their current ubiquity and their evolved increased efficiency. With the rise of research into soft sensor and actuator devices, these such device need to follow suit of the traditional rigid sensors and actuators and become ubiquitous and viable option for general and specialised engineering design solutions.

This thesis has developed methods and tools for creating and characterising artificial pressure sensitive skin technology. The thesis then continues to explore the integration of this artificial skin technology into an artificial muscle technology. The work in this thesis has ultimately contributed towards a patent for DEA-EIT actuator-sensor technology in a quest to bring this work out of the academic realms into real-world applications.

### 1.1 Why Go Soft and Not Rigid?

The requirement for soft robotics in general has been driven by the limitations of current rigid robotic solutions to interact with natural organic material. Manipulation of natural organic objects such as animals, plants, fruit, vegetables, and meat have traditionally been handled by humans by hand due to our ability to use our dexterity and intelligent control systems to ensure minimal undesirable damage. With the advance in in technology in various soft robotic actuators[16–20], sensors[21], and soft robotics control[22, 23]. The use of soft robotics in place of rigid alternatives, amongst other benefits, has the opportunity to be more sustainable by decreasing waste products during fabrication, using biodegradable or recyclable materials, shelf life, and use of renewable resources[18]. The use of soft robotics brings opportunity of creating devices with a reduced bill of materials size and less moving parts for maintenance. The use of soft robotics in biomedical and aerospace applications is especially desirable due to the difficulties experienced when designing with regular motors in the outer space and near sensitive biological tissue environments such as heat dissipation, lubrication, and mass[24–27].

The most common rigid actuator is the rotary electric motor and the global market was valued at USD 142.2 billion in 2020, with a predicted growth rate of 9.5% until 2032[? ]. Although this

market is dominated by automobiles which currently require the traditional form of rotary electric motors, growing sectors of this market such as medical, factory automation, and aerospace have potential interest in adopting soft actuator alternatives for the reasons given above. In parallel, rigid strain sensors of types metallic foil and semiconductor, was given a global market value of USD 190.66 million in 2022 with a compound annual growth rate of 3.9% until 2029[? ]. Adjacently the pressure mapping global market value, focused mainly on the health sector, was valued at USD 480 million in 2023 with an expected growth rate of 5.1%[? ? ]. Many soft actuator technologies could be used in these growing medical, aerospace, factory automation, and agricultural sectors.

Soft robotic actuation can be achieved through various mechanisms including thermal, electrochemical, fluidic, magnetic, and electrostatic. Similarly soft stress-strain sensing can be achieved through various physical principles such as resistive, capacitive, magnetic, and optical sensing methods. Often the function of soft actuators can be inverted such that the deformation of the actuator can produce a signal used for self sensing, in electroactive polymer (EAP) technologies such as dielectric elastomer actuators (DEAs)[28–31] and ionic polymer-metal composites (IPMCs)[32]. EAPs have the benefit of electronic control over other soft actuator and sensor technologies controlled by fluids, heat, or light which contain the complexity of another energy transfer process.

Proprioception in artificial muscle technology has been made a reality. This is seen in the self-sensing of one dimensional strain of DEAs usually through capacitive measurement between the compliant electrodes during operations to obtain the magnitude of a contraction. However, the pressure mapping done similar to the mechanosensation performed by cutaneous mechanoreceptors on an artificial muscle device has not been explored as of writing this thesis.

Publications towards this thesis include three conference papers, one journal paper, and one provisional patent filed. This thesis has converged on the use of conductive particle based elastomer composites and their use in sensors and actuators, in particular an electrical impedance tomography (EIT) based artificial skin and it's integration into the artificial muscle technology, dielectric elastomer actuators. The composite type used throughout the thesis is simple to fabricate but not well understood in terms of its electromechanical transient and dynamic characteristics. The modelling of such conductive particle composites would elucidate the feasibility of inverting the model to create a responsive strain sensor. This composite has been characterised in one-dimension several times in literature already however, if a two dimensional sensing application of this composite is desired the characterisation of the sensor in two dimensions must be completed. A method to do such 2D sensing is using EIT. EIT has been used in the past for a huge range of applications, with few exploring the use of EIT as a pressure mapping sensor. Although EIT-based pressure mapping was first discovered 30 years ago, the technology is still in its infancy with several problems needing to be resolved before the technology can be used reliably in real-world applications.

## 1.2 Research Objectives

The research objectives and questions for this thesis are given below:

1. Quantify and analyse static, dynamic, and transient phenomena seen in conductive particle composites.
2. From the characterisation in objective 1 mitigate the effects of the transient phenomena.

3. Create a set of metrics for quantifying the performance of an electrical impedance tomography based artificial skin.
4. Simulate and integrate an electrical impedance tomography based artificial skin onto a dielectric elastomer actuator.
5. Investigate the energy harvesting of a device that is both a dielectric elastomer actuator and electrical impedance tomography device.

### 1.3 Chapter Contributions

Chapters 3 - ?? contain the core novel research contributions. Chapters 2 and ?? provide essential background knowledge and future research directions for the thesis respectively.

**Chapter 2 - Literature Review:** This chapter explores the nature of biological skin and muscle from an engineering perspective, quantifying necessary functions and properties desired to replicate or supersede for their artificial equivalents. The thesis then describes state-of-the-art soft sensors and actuators and their function.

**Chapter 3 - Characterising Non-Linear Behaviour in Carbon-Black Elastomer Nano-Composites:** This chapter uncovers the electromechanical tensile and compressive properties of carbon black silicone composites, in order to understand the material before it's use in sensors and actuators.

**Chapter 4 - An Improved an Electrical Impedance Tomography Based Artificial Soft Skin Pressure Sensor:** This chapter discusses the use of electrical impedance tomography to create a pressure mapping sensor and provides tools for analysing the suitability to various applications and choosing a suitable sensing domain.

**Chapter 5 - Giving Artificial Muscles the Sense of Touch:** This chapter describes the integration of the pressure mapping technology discussed in the previous chapter, how it can be integrated into dielectric elastomer actuators, and the trade-offs.

**Chapter 6 - Unintentional Power Generation in a DEA-EIT Sensor-Actuator Device:** This chapter discussed the unintended power generation of the simultaneous sensor actuator device discussed in the previous chapter.

**Chapter 7 - A Portable Electrical Impedance Tomography Based Pressure Mapping Sensor and Validation System:** This chapter discusses the small form factor, low-cost hardware design for a hybrid artificial muscle - artificial skin based device.

**Chapter 8 - ?? Modelling of DEA-EIT Capacitively driven Hybird Sensing and Actuation Device:** The is chapter models the a DE-EIT device in order to find an optimal range of parameters at which capacitive shunting can be used to improve the DE-EIT pressure mapping device responsiveness.

**Chapter 9 - The Biomimetic Re-Evolution:** This chapter discusses the future direction of the technology discussed in the thesis and acknowledges the future of the broad field of soft robotics.

# Chapter 2

## Literature Review

Humans can complete complex tasks due to their intelligence, dexterity, and physical make up. These complex tasks include agricultural picking, culinary preparation, factory goods processing, and biomedical practice. To complete these tasks with machines it is important to quantify these human qualities that the technology must match or supersede. The first part of this section is focused on understanding and quantifying human skin and muscle tissue often required for these complex human tasks. In parallel, artificial skin and artificial muscle state-of-the-art technology is reviewed. Finally, background theory on piezoresistive elastomer composites which will be utilised with specific sensor and actuator technology is given to setup foundational knowledge base and reference for the rest of the thesis.

### 2.1 Biological Skin form and function

Skin is the largest organ in the human body with many functions, however this thesis only aims to replicate some pressure-sensitive functions of skin. Two pressure-sensitive categories of skin and muscle tissue transducers which allow for dexterous manipulation of objects are:

1. Proprioceptors: respond to internal mechanical stimuli in a joint capsule, tendon, or muscle to give the sense of motion.
2. Cutaneous mechanoreceptors: respond to mechanical stimuli usually external to the body, including pressure and vibration, for the localisation of sensations.

Locations of both proprioceptors and cutaneous mechanoreceptors are shown diagrammatically in Figure 2.1. Proprioceptors aid in determining pose estimates of body parts in space, acting as sensors providing feedback closed-loop control for the neurological motion control of body parts. Whereas cutaneous mechanoreceptors have various roles including object recognition, manipulation control, as well as motion control.

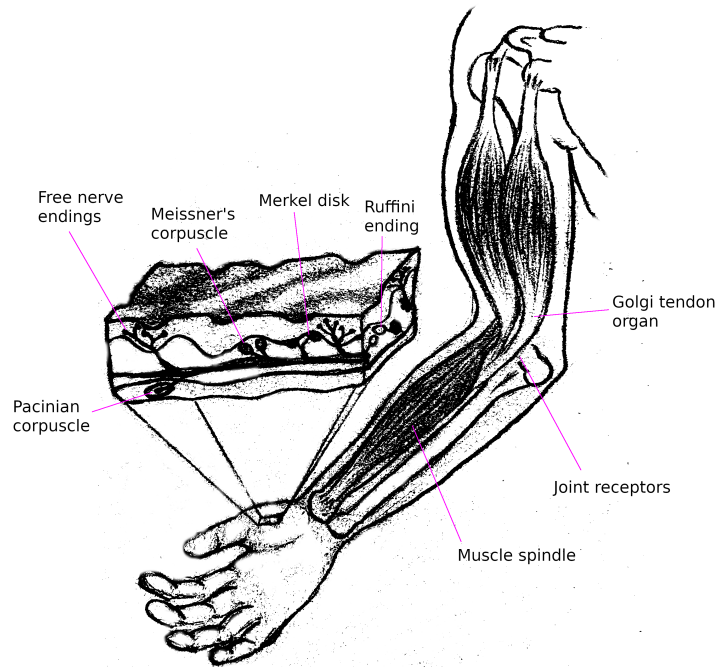


FIGURE 2.1: Examples of the locations of proprioceptors and cutaneous mechanoreceptors in the human body.

The function of both kinds of receptor have been mimicked by certain device technologies. For example proprioceptors have been mimicked in wearables and human assistive devices where joint motion has been estimated by sensors such as rotary/linear encoders, inertial measurement units (IMUs), and stretch sensors fixed adjacent to joints to calculate pose estimates of limbs[1–4]. Examples of such devices are displayed in Figure 2.2

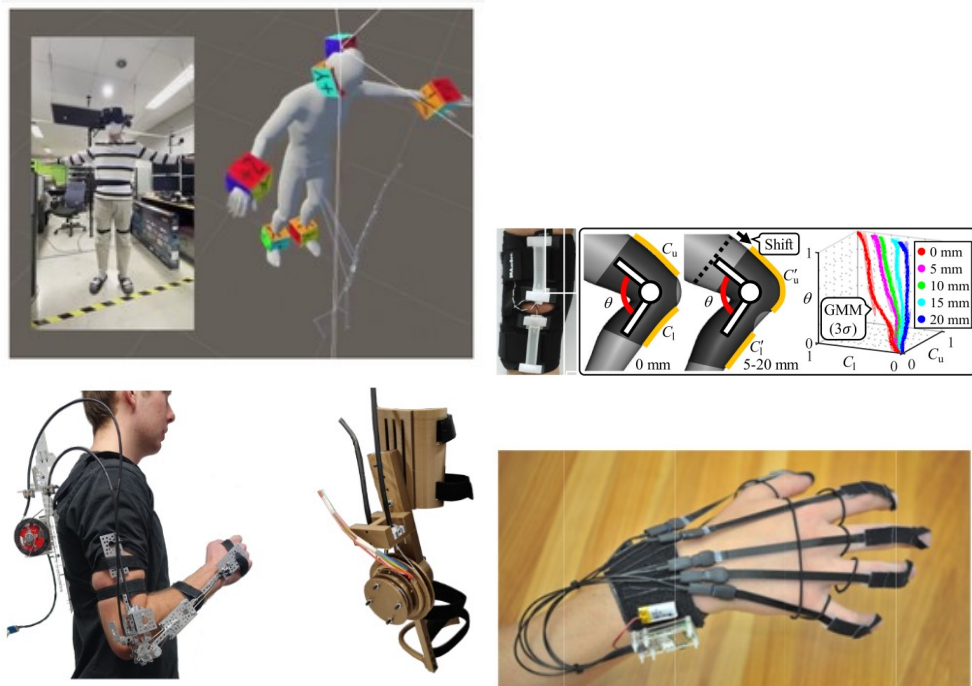


FIGURE 2.2: Clockwise from top left: IMU pose estimation[1] (© 2022 MDPI), stretch sensor knee joint pose estimation[2] (© 2020 IEEE), encoder elbow pose joint estimation[3], stretch sensor hand joint pose estimations[4].

Cutaneous mechanoreceptors have been mimicked by the development of pressure mapping of flexible surfaces. Examples of such technologies include, foot pressure based gait analysis, wheelchair seat pressure mapping. Commercially available examples of these sensors are shown in Figure 2.3.



FIGURE 2.3: Various pressure mapping devices. From top-left then clockwise: XSensor wheelchair pressure mapping sheet (© 2024 XSENSOR® Technology)[5], Pressure Profile Systems pressure sensors on a robotic hand (© 2023 PPS UK limited)[6], Soft pressure mapping gripper(© 2023 PowerON)[7], Tekscan thin pressure mapping platform[8](© 2024 Tekscan Inc.), Tactilus seat pressure mapping system[9](© 2024 Sensor Products Inc.)

Many of these pressure mapping technologies don't accurately mimic desirable qualities of regular biological skin and are specialised for their specific use cases. The following sections quantify characteristics of pressure sensitive skin.

### 2.1.1 Skin Construction and Types

Skin is a laminate structure consisting of three main layers, the epidermis, dermis, and hypodermis. The top two layers the epidermis and dermis are a subset of the cutaneous layer which contain the majority of the pressure-sensitive mechanoreceptors [33].

The skin can be categorised as glabrous/hairless or non-glabrous/hairy. Glabrous skin contains many of the mechanoreceptors given in Figure 2.1 whereas non-glabrous skin will also contain C-tactile afferent receptors for obtaining sensations through hair follicles. However this work is exploring simple monolithic/homogeneous-composite bodies so will not be replicating the sensor function of non-glabrous skin.

Depending on the region of skin different force resolution and spatial resolution will incur. Relevant cutaneous mechanoreceptors and their functions are given in Table 2.1. The tensile properties of skin is governed by skin tension lines, also called Lager's lines, which show the direction in which the maximal stretch can occur.

TABLE 2.1: Comparison of typical mammalian mechanoreceptor characteristics [15].

Receptor	Meissner corpuscle A1	Ruffini Corpuscle A2	Pancian Corpuscle B1
<b>Perceptual sensory functions</b>	Skin movement, handling objects	Skin stretch, movement direction, hand shape, and finger position	Fine tactile discrimination, form and texture perception
<b>Skin stimulus</b>	Dynamic deformation	Skin stretch	Indentation depth
<b>Localisation</b>	Dermal papillae	Dermis	Basal layer of epidermis / around guard hair
<b>Conduction velocity</b>	35 - 70 m/s	35 - 70 m/s	35 - 70 m/s
<b>Receptive field</b>	22 mm <sup>2</sup>	60 mm <sup>2</sup>	9 mm <sup>2</sup>
<b>Receptor density</b>	150 / cm <sup>2</sup>	10 / cm <sup>2</sup>	100 / cm <sup>2</sup>

### 2.1.2 Characterising skin

The sensing qualities of skin is crucial for the sensory feedback in complex manipulation tasks. To aid the creation of technology that mimics qualities of biological pressure sensitive skin, the mechanical properties must be characterised. Biological human skin is highly variable in terms of its mechanical and sensing properties depending on the region of skin, giving large variation in skin characteristics. Skin can be characterised in terms of the following mechanical characteristics:

1. Elastic modulus - The static elastic properties determined by a linear region of stress and strain of the material. [Pa]
2. Storage and loss modulus - The dynamic elastic and viscoelastic properties determining the relationship between stress and strain. [Pa]
3. Ultimate tensile stress (UTS) - The maximum tensile stress that a material can tolerate before breaking [Pa]
4. Life cycle - The time or number of actuation cycles in which it takes for the actuator to degrade such that it cannot perform its intended purpose to specified standards.

5. Viscoelastic creep and relaxation - All viscoelastic materials will experience strain creep and stress relaxation to varying degrees depending on the viscoelastic properties of the material. [ $\text{mm} \cdot \text{s}^{-1}$  and s]
6. Skin thicknesses - the thickness of all layers of skin the cutaneous epidermis and dermis and thickness of the hypodermis. [mm]
7. Skin surface area - Biological skin has a large surface area and can also be regionalised to map skin function and sensitivity. [ $\text{m}^2$ ]
8. Isotropy/Anisotropy - The directionality of skin properties, also known as skin tension lines, give a topological map of the maximal stretch (i.e. minimal elastic modulus) direction of regions of skin.

Some of the functional properties in terms of pressure mapping include:

1. Spatial resolution and touch acuity - The spatial resolution of biological skin, which is mainly dependent on the innervation, mechanoreceptors density, and thickness of the cutaneous layers of skin [34–36].
2. Static force resolution - This is the detection resolution of static or slow-acting forces acting upon the skin [36].
3. Temporal resolution - This is the detection resolution of fast-acting forces acting upon the skin often required for texture recognition [34, 36].

A quantitative characterisation of mechanical and pressure sensing functional skin properties include:

1. Elastic modulus - varies largely depending on test method, test skin type, and subject. Values found in literature include  $83.3 \pm 34.9$  MPa [37], 0.1 - 2.4 MPa [38], and 10.4 - 89.4 kPa [39].
2. Storage and loss modulus - varies largely depending on test method, test skin type, and subject. Values found in literature range include  $141.9 \pm 34.8$  Pa and  $473.9 \pm 42.5$  Pa at 0.8 Hz [40],  $473.9 \pm 42.5$  Pa and  $32.3 \pm 10.0$  Pa at 205 Hz [41].
3. Ultimate tensile stress -  $21.6 \pm 8.4$  MPa [37].  $28.0 \pm 5.7$  MPa [42]
4. Life cycle - Skin cells are constantly growing, dying, and shedding. Skin is always actively remodelling based on external stimuli [33].
5. Strain creep - The strain creep was found to be 2.7 kPa.s for a 10 Pa step input on a dermis skin sample [40].
6. Skin thicknesses - The thickness of human cutaneous skin ranges from 0.6 to 2.6 mm with an average skin thickness of 2 mm [34].
7. Skin surface area - The average surface area of skin in adult humans is  $1.7 \pm 0.1 \text{ m}^2$  [34].
8. Isotropy/Anisotropy - The tension lines in skin are determined by collagen fibre orientation and dynamic stretch events [43, 44]. The elastic modulus of human skin was reported to be  $160.8 \pm 53.2$  MPa parallel to the skin tension lines and  $70.6 \pm 59.5$  MPa perpendicular to the tension lines [42]. The UTS of human skin was reported to be  $28.0 \pm 5.7$  MPa parallel to the tension lines and  $15.6 \pm 5.2$  MPa perpendicular to the tension lines [42].

1. Spatial resolution and touch acuity - The tactile field area increases with indentation depth for certain mechanoreceptors with a range of  $5 - 12.6 \text{ mm}^2$  [45]. Two point discrimination is another metric for determining spatial resolution and has been determined as  $3.7 \pm 0.7 \text{ mm}$  [46]. The receptive field varies depending on the mechanoreceptors used so has been reported to be between 1 and  $60 \text{ mm}^2$  as another methods of inferring spatial resolution [15].
2. Force resolution - Minimum force detection on various regions of human skin was found to be between  $67 - 1007 \text{ mg}$  [47], and various mechanoreceptors  $0.73 - 122.6 \text{ mN}$  [48].
3. Temporal resolution - Depending on the mechanoreceptor sensing the force input, a frequencies ranges of 0 to 800 Hz can be perceived by human skin [45]

### 2.1.3 Skin Modelling

Developing robust mechanical models for human skin is non-trivial for three main reasons:

1. High degree of viscoelasticity
2. Self-regeneration and healing
3. Constructed from various types of cells in a laminate structure

To solve the complexity of modelling such a material a review by Landry et al.[34] shows that many researchers have applied various non-linear mechanical models including Ogden, Mooney–Rivlin, Neo-Hookean, Yeoh, Humphrey, and Veronda–Westmann. When recreating an artificial muscle it is desirable to minimise the mechanical material model complexity so that the material can be more easily integrated into a control system with known behaviour. Similar modelling techniques can be used to model conductive particle elastomer composites due to the similar hyper-elastic and visco-elastic behaviours observed.

## 2.2 Pressure Mapping Artificial Skin Devices

This section outlines some of the main technologies which are flexible and/or soft a comparable softness to human skin tissue and can map force events throughout a surface. A particular focus on electro-active polymer (EAP) based sensing is present due to the potential of miniaturising the technology and the range of miniaturised electronics currently available. EAPs are essentially polymer materials which can be used as transducers which change electrical properties based on a mechanical input, vice versa.

### 2.2.1 Soft Pressure mapping technology

Pressure mapping devices can be categorised into their various sensing technology, such as resistive, capacitive, inductive, magnetic, optical, and acoustic. Transduction methods have been compared by Tiwana et al.[49], with recommendations to pursue ‘capacitive, resistive, piezoelectric, piezoresistive or a combination’ of methods to replicate mechanoreceptors in the human skin. However, additional optical and magnetic/inductive methods will also be considered in the following sections.

### 2.2.1.1 Resistive

Soft resistive pressure mapping has been commonly achieved in the past by using arrays of piezoresistive sensor elements, some of which are shown in Table 2.3. The resistive elements can be made using several different flexible piezoresistive materials, such as conductive particle polymer composites[50–52], intrinsically conductive polymers[51, 53? ], microfluidic metals[54–56], hydrogel structures [57–59], and flexible piezoresistive semiconductors[60, 61].

TABLE 2.2: Comparison of different potential piezo-resistive sensor materials. Ranked 1 to 5, where 1 is desirable and 5 is undesirable. WIP - need to redo properly and find a reference for each box!

Material:	Conductivity	Piezo-resistivity	Hardness	Manufacturability	Cost	Durability	Toxicity	Drift
Conducting polymer	5	3	3	2	2	3	2	3
Electrolytic hydrogel	1	2	4	3	4	2	2	2
Conductive particle polymer	2	4	4	4	4	4	2	
Conductive particle paste	3	2	4	3	4	2	3	2
Conductive textile	4	4	3	2	4	5	4	3

### 2.2.1.2 Capacitive

Similar to resistive pressure mapping, capacitive pressure mapping has more commonly been done using arrays of capacitive elements. Many capacitive touch sensors use the human body to shunt the electric field between the capacitor electrode(s) to a common ground. However, the operating principle of capacitive-based strain sensors rely on the deformation of the capacitor dielectric and/or the capacitor electrodes [62? , 63]

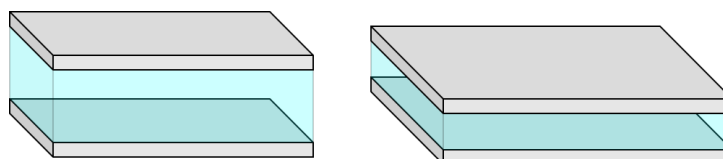


FIGURE 2.4: Two grey electrodes across a blue dielectric medium. Left: Uncompressed state. Right: Compressed state exhibiting larger electrode areas and a thinner dielectric thickness.

### 2.2.1.3 Magnetic

Magnetic strain mapping devices can be achieved using several methods. One method is to have a three layer stack with hall effect sensors [64]. The stack is made up of a the bottom layer full of rigidly connected three dimensional hall effect sensors, the second layer is made from an elastomer, and the top layer has a magnetic particle unit placed at a set distance above each of the hall effect sensors. The movement of the magnets alters the magnitude and direction of magnetic field sensed and data can be interpolated to create a map of strain deformation. The main advantages of this method is that each hall sensor can detect in three dimensions, hence normal and shear forces can be detected, and using magnetismfor sensing means less electrical noise in the system. The main disadvantages of this method of sensing is the added complexity in scaling the system and the electronics required and the rigid surface required.

### 2.2.1.4 Optical

There are various methods for making a optically driven artificial skins. A recent review has been curated by Lee et al. [65] all of the different methods of using optics for creating tactile sensors. The main advantages of optical sensors include the high speed sensor response, immunity to electrical noise, and their non-invasive nature. The main disadvantages include, the bulky hardware required for driving the optics and signal processing, the potential interference of external light sources, and the materials that can carry optical signals.

### 2.2.1.5 Acoustic

Acoustic soft tactile sensing has not been explored much compared to the other forms of sensing given. Park et al., Hughes and Correll [58, 66] have created a system which uses passive acoustic tomogrphy (PAT) to localise and and classify different types of touch. This form of tactile sensing is the most similar to the biological system of mechanoreceptors which are specialised to detect certain frequencies of vibration.

### 2.2.1.6 Soft Pressure mapping technology comparison

The softness of biological human skin has a large range as discussed in Section 2.1.2. There have been a range of works investigating sensors with a range of softness' and performance. A comparison of these start-of-the-art soft sensor works is given in Table 2.3.

TABLE 2.3: Comparison of soft sensor technologies.

1st Author	Sensing principle	Sensing region material	Sensing region elastic modulus or shore hardness	Electrodes per sensing position	Repeatability	Time series data shown	Spatial resolution	Temporal resolution
Gilanizadehdizaj [67]	Piezo-resistive	Ecoflex30-00 rGO composite sponge	40 kPa	2 sensels / electrode	10 cycles for each stress	-	10 x 10 mm	-
Fu[68]	Piezo-resistive	Carbon black silicone composite	1.5 Mpa	0.625 sensels / electrode	50000 cycles	Yes.	12 x 12 mm	60 ms
Yang[69]	Piezo-resistive	Ecoflex graphene composite sponge	-	2 sensels / electrode	800 cycles	Yes.	10 x 10 mm	150 ms
Liang[63]	Capacitive	PDMS, PET, Si, Sio2, Cu laminate	4000 Mpa	1 sensel / electrode	-	Real-time use of sensor shown. No explicit time-series data.	4 x 4 mm	-
Yan[64]	Magnetic	Ecoflex 00-50	83 kPa	11 IC pins / sensel	30,000 cycles	Yes.	0.1 x 0.1 mm	15 ms
Rossiter[70]	Optical	Polymer foam	-	2 sensels / electrode	-	-	10 x 10 mm	-
Shimdera[71]	Optical	Super clear silicone	40 A	N/A. One fiber optic LASER and one camera.	Error increase of 1.7% over 30 days	Yes.	approx. 20 x 20 mm / 0 - 1100 um	Sample rate 1.6s. Training required.
Ramuz[72]	Optical	PDMS	-	N/A. Two arrays of OLEDs and Organic Photo Detectors used.	900 cycles	Yes.	Not localised.	300 ms

## 2.3 Biological Muscle form and function

Biological muscles are a product of millions of years of evolution and the motion and other mechanical characteristics of biological structures is yet to be outperformed by artificial muscle technology. To determine how to quantify the performance of a biological muscle this section gives foundational knowledge about muscle function, structure, and how it can be characterised from an engineering perspective rather than the typical biological perspective, so that similar actuator devices with similar attributes can then be investigated.

Biological muscle is a naturally occurring tissue comprised of muscle fibres bundled together to apply a contractile force on connecting tissue or, in the case of smooth muscle, applying a force on itself. The base actuator units of muscle are proteins myosin and actin filaments, which effectively slide against each other to produce a contractile motion. The root cause of a muscle contraction is an electrochemical signal sent from the central nervous system to a motor neuron/s which travel to the muscle where electrochemical reactions take place for the contraction to occur[73]. The sliding motion of the myosin and actin filaments is due myosin

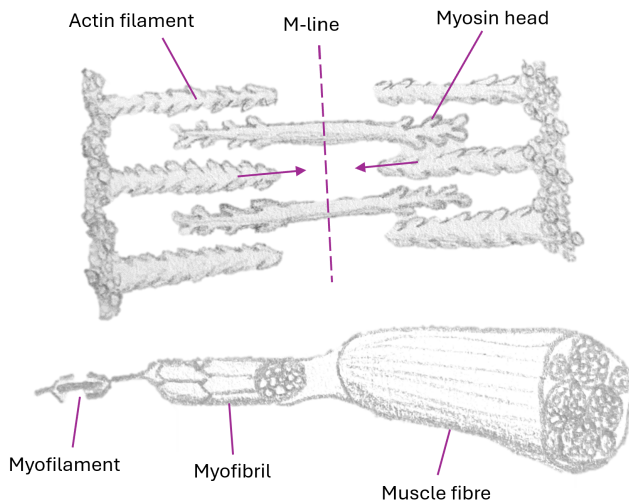


FIGURE 2.5: Components of a biological muscle contractile unit and meta-structure.

heads binding to the actin and pulling the actin towards a middle line (M-line) in multiple stroke actions. These filament actuators are stacked in three dimensions within a muscle fibre to amplify contractile stress and strain as shown in Figure 2.5.

On a macro scale, muscle is made up of bundles of fascicles connected together with a tissue called perimysium. Within the fascicles are many muscle fibres (i.e. muscle cells) which are surrounded by a connective tissue called endomysium. Within the muscle fibres there are many sacromeres stacked within a cylindrical-like structure called a myofibril. Each sacromere contains a contractile unit of myofilaments.

### 2.3.1 Characterising a muscle

To quantify the performance of a biological muscle, certain metrics are compared. An artificial and biological muscle can be characterised using typical mechanical material parameters such as:

1. Stress - Force that is applied to the normal of the cross section of the muscle through various states of muscle excitation.  $[Pa]$
2. Strain - The muscle change of length due to the stress applied through various states of muscle excitation.  $[\%]$
3. Elastic modulus - The elasticity determining the relationship between stress and strain for the linear region of the stress strain characteristic curve.  $[Pa]$
4. Energy density - The work done by the muscle per unit volume or mass.  $[J.kg^{-1}]$
5. Power density - The work done by the muscle per unit volume or mass per unit time.  $[W.kg^{-1}]$
6. Ultimate tensile strength - The maximum tensile stress that a material can tolerate before breaking.  $[Pa]$
7. Efficiency - The work done by the muscle compared to the energy put into the system, known as metabolic cost in biological muscles.  $[\%]$
8. Actuation frequency - The frequency range of actuation cycles using the system's method of excitation.  $[Hz]$
9. Stroke - The maximum displacement an actuator can achieve  $[m]$
10. Life cycle - The time or number of actuation cycles in which it takes for the actuator to degrade such that it cannot perform its intended purpose to specified standards.

As well as the commonly used medical/biological muscle metric:

11. Maximum isometric contraction force - the maximum force a muscle can apply without changing strain. This is also related to the ratchet-like mechanism and muscle locking where a muscle can apply a much larger force in a static state, as seen in the myosin binding[74].

Other qualities of muscle should be quantified on a case by case basis depending on the artificial muscle technology being investigated. For example, a major issue with dielectric elastomer actuators is the excitation voltage required for actuation is too large for many applications. Hence, excitation voltage could be another parameter considered for some electroactive artificial muscles.

Some of the biological muscle metrics have been quantified by previous research as seen below:

- Energy density - energy densities ranging from 0.4 - 40  $J.kg^{-1}$ [75].
- Power density - power densities ranging from 9 - 284  $W.kg^{-1}$ [76]
- Actuation frequency - natural actuation frequencies ranges 1 to 180  $Hz$ [76].
- Strain - ranging from 5 - 30%[77].
- Efficiency - Thermodynamic efficiency of human muscle is typically between 20-35%[78]. However other biological muscle has been seen to reach efficiencies of up to 77%[78].

### 2.3.2 Muscle Mechanics

Before attempting to recreate a bio-mimetic actuator it is important to acknowledge the numerous simplified electro-mechanical system models of parts of the muscle actuation process. These models need to be understood to gain an understanding of the application of biomimetic actuators can be used in assistive soft robotic devices. From here we will present basics of the subject of bio-mechanics.

The stress and strain involved in muscle contraction is more complex than uniform materials and is non-linear. The stress and strain of a passive muscle (i.e. contractile units are not producing internal muscle tension) can be modelled with the following equation;

$$\frac{d\sigma}{d\varepsilon} = \alpha \cdot (\sigma + \beta) \quad (2.1)$$

Where  $\varepsilon$  &  $\sigma$  are strain and stress respectively. A solution for this is first order ODE is;

$$\sigma = \mu e^{\alpha\varepsilon} - \beta \quad (2.2)$$

Where  $\mu$  is a free parameter determined empirically. The stress-strain of a passive muscle can be likened to tension being applied yarn. As more strands of the yarn are pulled into tension the stress increases, then as the last strands are brought into tension a maximum stress is reached, until the yield stress is reached. Linear approximations can still be made over regions of elongation depending on accuracy required for application. The stress-strain of an active muscle (i.e. when it is tetanised) is approximated to a piece-wise quadratic function or bell curve. It is important to note that the stress for both active and passive muscle is zero when the strain is less than 0.4, demonstrating the yarn-like nature of the muscle stress-strain as shown in Figure 2.6.

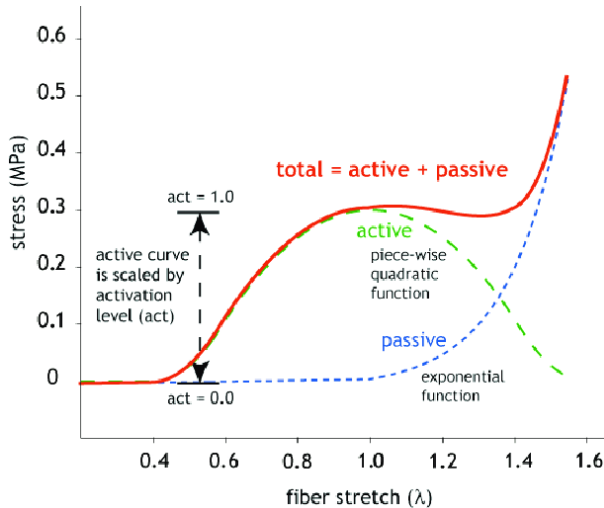


FIGURE 2.6: Stress and strain of active and passive muscles (© J. Teran | ACM 2003)[10]

Hill's muscle models commonly refer to a mechanical three element model [79] composed from, one parallel non-linear spring element, one series non-linear spring element, and a contractile unit.

### 2.3.3 Electrical Muscle Models

Similar to EAP-based artificial skin and artificial muscles, biological muscles also require electrical stimulation to function. The main method for providing an artificial electrical stimulation to a muscle, to simulate the signal a motor neuron would give to a muscle, is functional electrical stimulation (FES). Due to the biochemical nature of the motor neuron signal transport and the purely electrical stimulation provided by the FES device, the process isn't as efficient as the naturally occurring electro-chemical muscle activation, often resulting in increased muscle fatigue when compared to equivalent voluntary muscle contractions [80]. FES applies a voltage across between two electrodes on the user's skin above a specific muscle. The voltage simulates the signal form and frequency of action potentials between 4 - 12Hz[81]. The threshold for a muscle action potential to cause a muscle contraction is approximately 70 mV [82]. To artificially sense an intended muscle contraction electromyography (EMG) can be used. EMG also commonly uses two electrodes on the surface of the skin above a desired muscle. This EMG signal can be used as a sensor input for joint pose estimation. EMG senses the action potential impulses conducted along motor neurons to the muscle. There are many models for limb motion and EMG- and FES-based therapies [83–86].

## 2.4 Artificial Muscle Technology

There are many types of electrically actuated artificial muscles technology. Artificial muscle actuator technology that has gained particular interest in recent years include, the ionic polymer-metal composite (IPMC) actuator, the hydraulically amplified self-healing electrostatic (HASEL) actuator, magnetorheological elastomer (MRE) actuators, and dielectric elastomer actuators (DEAs). Each of these having qualities very similar to that of biological muscle usually with a trade-off in actuation response time, actuation force, and actuation strain for their various possible topologies. This section gives a brief overview of four state-of-art soft electromagnetically driven actuator technologies.

### 2.4.0.1 Ionic polymer–metal composite actuator

Ionic polymer-metal composite actuators (IPMCs) are soft actuators that can be actuated at a much lower excitation voltage than DEAs, commonly less than 10V. IPMCs are also desirable as artificial muscles they have shown large bending deformations, simple to fabricate, light weight and thin in design, and can have a fast actuation response time ( $>15\text{Hz}$ ) at small displacements[87]. IPMCs also have a high work density and maintain a constant volume during actuation like biological muscles[88]. An IPMC is made up of an ionic polymer interlayer, two electrode conductive layers, and a voltage source. The ionic polymer interlayer allows for ionic transport and is typically made of treated Nafion or Flemion. These materials are typically used as ion exchange membranes so have the characteristics desired for the transporting ions during the actuation of the IPMC actuator. The two electrodes are made of a suitably conductive and flexible material. The interlayer is treated such that it is filled with water molecules and cations, with the chemical backbone of the interlayer being slightly negatively charged. When a voltage is applied across the electrodes the cations are repelled from the cathode and travel towards the anode while the water molecules are displaced in the opposite direction towards the cathode. The ionic polymer then swells as the cations repel each other along the anode side of the interlayer, while the polymer elements on the cathode side effectively shrink[89]. This swelling adjacent to the cathode provides the device's bending actuation.

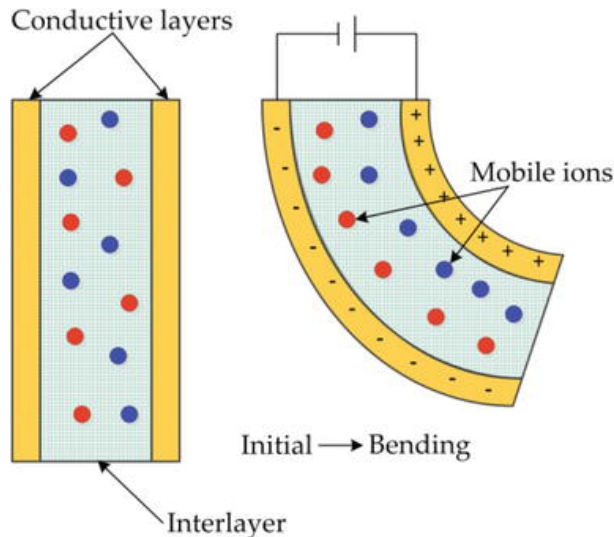


FIGURE 2.7: Diagram of the typical architecture of an IPMC actuator[11] (© 2018 Yanjie Wang and Takushi Sugino)

There are many variations of the design and manufacturing of IPMCs to optimise the actuator for an application as shown by [90]. Although the process of manufacturing IPMCs is simple, it takes a long amount of time (often >48 hours[87]) for the ionic polymer interlayer to absorb the necessary ions and undergo the necessary reactions. There has been much research into the optimal manufacturing of an IPMC [90–92]. The use of additive manufacturing has been used successfully to generate more complex geometries using fused filament deposition[93].

IPMCs can also be used as sensors. When an IPMC undergoes bending due to an external force there is a potential generated across the electrodes, which indicates bending direction and magnitude[94].

Two key deficiencies of current IPMC actuator technology are the maximum force output achievable and the life cycle of the actuator in a dry (non-aqueous) environment. The force output optimisation of IPMCs has been investigated by several researchers, all of which having a maximum actuation force in the milli-newton scale [94–96]. Because the IPMC actuators rely on hydrated ionic transport to actuate this means if the IPMCs are in a dry environment then over time they will decrease their maximum actuation force.

The applications of this actuator is limited to applications requiring a small actuation force and a wet environment. Current applications include flexible catheters [97], small biomimetic robotics [98, 99], aquatic robotics[100, 101], with many other applications yet to be discovered.

#### 2.4.0.2 HASEL actuator

A hydraulically amplified self-healing electrostatic (HASEL) actuator is a recent soft actuator technology developed in 2018[12] which displays many qualities that are better than current artificial muscle technology. HASEL actuators are made up of three main components: electrodes, dielectric fluid, and an elastomeric shell. The electrodes need to be highly conductive, able to handle high electric potential, and can be solid or flexible. Hydrogel electrodes have been proven to be a good material for the electrodes because of their elasticity while still maintaining a high conductivity[102]. In one application the hydrogel material is bonded to a polydimethylsiloxane (PDMS) substrate for mechanical strength and for ease of bonding to the actuator biaxially-oriented polypropylene (BOPP) shell[12, 57]. HASEL actuators use high electric potential across

two electrodes to create an electrostatic force. This force induces a zipping effect which pulls the electrode together from one end to the other as the electric field strength increases. The zipping of the two electrodes pushes the dielectric fluid into the reservoir increasing the pressure which alters the shape of the reservoir bounds providing an actuation motion. When the electrodes have displaced all of the fluid between them the actuation displacement is at a maximum. The electrostatic zipping action allows a large force to be generated due to snap-through transition. Snap-through transition is an actuation instability which has been discussed in previous research as a means of amplifying DEA actuation strain[103]. Recorded efficiency values of HASEL actuators

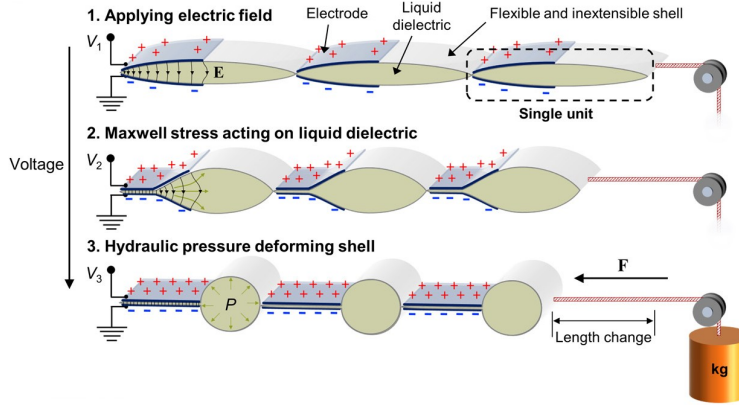


FIGURE 2.8: Diagram of the typical architecture and the contraction stages of a HASEL actuator[12]

actuators of 21% are comparable to that of human muscles of 20 - 35% [78]. The actuators have had a frequency response of up to 20Hz. Large strains of 124% have been recorded, but can only be achieved when actuating at a resonant frequency. Strains of up to 79% have been recorded using a linear planar HASEL actuator configuration and DC voltage stepping. Else, strains of only 10% have been recorded for static steady strain[12]. Because there is a relationship between the motion of the actuation and capacitance between the electrodes, this means self sensing can be achieved through the electrodes. Although due to the flexible and fluid nature of the device, modelling of the HASEL is difficult and limited in accuracy.

The simple and commonly used manufacturing process for HASEL actuators is completed in six steps as shown by the diagram below:

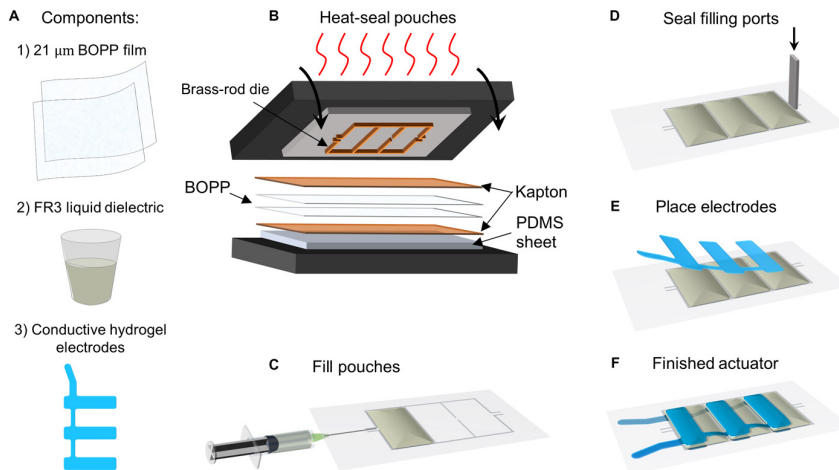


FIGURE 2.9: Diagram of the simplified stages of HASEL actuator production[12]

Other attempts have been made to use polyjet inkjet based additive manufacturing to make the whole HASEL actuator and have been successful with proof of concept, but are yet to be developed from prototype stage[104].

The cyclic life of HASEL actuators are high, because of their self-healing properties. When there is a dielectric breakdown through the liquid dielectric the damage caused is not permanent like when a DE breaks down. The liquid may form some small air bubbles, however these may not effect the operation of the actuator, instead this can increase the likelihood of another dielectric breakdown. The cycle life of the HASEL actuator was seen to be larger than one million with a given torus shaped HASEL actuator[102]. The HASEL technology is promising with a number topologies possible, some topologies include toroidal, planar linear[102], and scorpion metasoma(tail)[105].

#### 2.4.0.3 Dielectric Elastomer Actuators

The dielectric elastomer actuator (DEAs) are often called artificial muscles because they share similar characteristics to biological muscle such as, the large strains achievable, the high elastic energy density, many topologies/configurations achievable, and constant volume during its contraction.

A DEA consists of a dielectric elastomer (DE) film sandwiched between two compliant electrodes. To excite the actuation, a high electric potential is applied to across the electrodes creating an electrostatic force between the two compliant electrodes. This force pulls the two electrodes together applying stress (known as Maxwell's stress) to the elastomer and hence strain parallel and perpendicular to direction of the electrostatic force. When the DEA is contracted the surface area of the electrodes increases and the thickness of the DE decreases causing a change in capacitance and Maxwell's stress. A dielectric elastomer actuator can be modelled

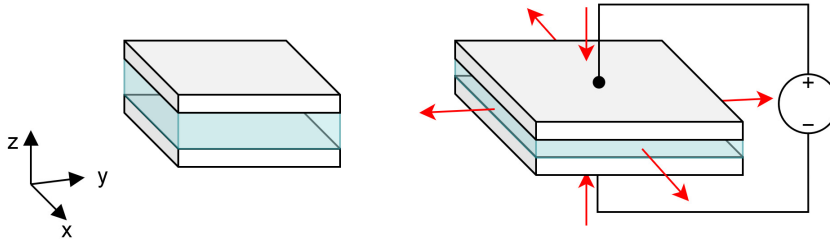


FIGURE 2.10: DEA with two compliant light-grey electrodes and a transparent light blue dielectric elastomer. Showing deformation without and with a voltage applied across the electrodes.

as a flexible parallel plate capacitor in its simplest form. Using this we can determine the electrostatic pressure to be:

$$\sigma_{es} = \epsilon_0 \epsilon_r \frac{V^2}{z^2} \quad (2.3)$$

Where  $\sigma_{es}$  is the electrostatic pressure,  $\epsilon_0$  and  $\epsilon_r$  are the vacuum and relative permittivity constants,  $V$  is the voltage potential applied across the electrodes and  $z$  is the thickness of the DE. The electrodes used for a DEA need to be made of a conductive material, but require similar elasticity to the dielectric material. An ideal material for these electrodes would have high conductivity. This conductivity would change minimally and predictively under large strains. Many composites have been used in practice for these electrodes, with the most common in early development being a silicone rubber and carbon powder composite. However, the unpredictable nature of carbon powder elastomer composites has lead to research into many

other materials/silicone additives such as hydrogels, graphene sheets, metallic nanostructures, carbon nanotubes, liquid metal[106–109]. The ideal material for the dielectric elastomer should have a high elastic modulus and a high electric breakdown voltage. The elastic modulus needs to be sufficiently high so that less electrostatic pressure can create a larger strain. While the breakdown voltage of the material needs to be sufficiently high such that the material will not break down at the maximum desired strain. If a material can be found with a high enough electric breakdown strength at a smaller thickness than current research prototypes then a higher stress can be achieved giving a larger or equivalent actuation force at a lower voltage.

Many other topologies exist to generate different actuation motions using the same electrostatic pressure generation principle. These include actuator topologies such as stack[110, 111], helical[112], bending[113], lens[114], cylindrical, and rolled shaped actuators[115]. Each of which having a range of applications.

DEAs are often fabricated in a laboratory environment using a pre-strained elastomer. The pre-straining accomplishes four key qualities; stores elastic strain energy, ensures DE is planar within the bounds of the jig, controls the initial thickness of the DE, and puts the DE in an optimal stress-strain region, often taking advantage of elastomer hyper-elasticity. There is no standard practice for the fabrication of DEAs, other methods such as additive manufacturing have also been explored to generate more complex geometries and to increase production speed[116, 117].

As well as actuating, DEAs can also be used for sensing. DEAs can be used as sensitive capacitive sensors, where any strain applied to the DE will relate to the effective capacitance between the two electrodes[28, 118, 119].

Currently dielectric elastomer actuators all require voltages within the kilo-volt range to generate an adequate stress and strain for a range of applications. A key problem encountered by researchers designing DEAs is the trade-off between actuation force and strain magnitude [110]. This high voltage requirement may deem the technology dangerous for use where there is a possibility that a human may come into physical contact with the high voltage electrodes.

#### 2.4.0.4 Magnetorheological Elastomer

Magnetorheological elastomer (MRE) actuators, also known as magnetoactive soft materials (MSMs), are a relatively new form of actuator however the theory reinforcing operating principle has been known since at least the 1980s [120]. The structure of an MRE actuator generally consists of a ferromagnetic elastic composite and a driving magnetic field. An example of this is a composite of iron-carbonyl powder and PDMS. The operating principle of MREs is that magnetic flux travelling through the MRE will change mechanical characteristics within the elastomer (i.e. stiffness or displacement of the body). The operation of a MRE actuator is similar to a DEA however instead of having an electric field cause a contraction it is a magnetic field causing a deformation. An MRE is typically made of silicone rubber containing magnetic ferrite based particles uniformly distributing throughout its volume. This kind of actuator is current controlled and can hence operate at a low voltage. This helps mitigate the risk of electric shock of a device in close proximity to humans (unlike HASEL actuators and DEAs). A key issue with using magnetorheological elastomers as soft actuators is that they require heavy gauge conductors for the high current they require for generating a magnetic field. The high current requirement means that actuators have only been created that have a solid electromagnet driving a soft MRE[121].

When manufacturing MREs, uncured liquid silicone rubber is mixed with magnetic (commonly carbonyl iron) particles to form a 3 dimensional matrix of crosslinks with the magnetic particles

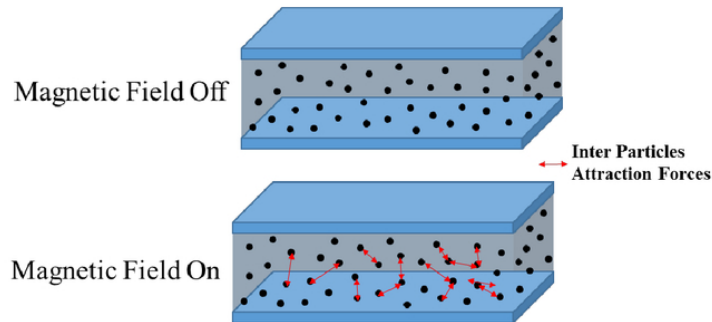


FIGURE 2.11: Diagram showing MRE contraction actuation when a magnetic field is applied[13]

fixed between the crosslinked polymers. A core issue when creating an MRE is the agglomeration and corrosion of magnetic particles due to residual water within the mixing operation. The magnetic particles can be processed to have a hydrophobic quality to mitigate this issue [122, 123]. During the curing process a magnetic field can be applied to align the particles within the elastomer to control the particle isotropy[123, 124].

There have been attempts to use additive manufacturing to make MREs[123, 125], however the method described has not optimised the structure of MRE for any application and the particle dispersion throughout the MRE has not been proven uniform throughout the print volume.

The current applications of MRE actuators are limited, however magnetorheological fluid (MRF), is a fluid which becomes more viscous with an applied magnetic field as currently has many modern applications. This fluid substance is largely used in applications where damping control is desired such as vehicle suspension[126], medical assistive devices[127] and helicopter seat damping [128]. Potential MRE actuator applications include fluid valve control[121] and active vibration control similar to that mentioned for MRFs[126].

## 2.5 Soft Conductive Particle Piezoresistive Composites

Soft sensors and actuators require low-stiffness materials for their active sensing/actuation domains. The requirement of softness is governed by the mechanical modulus values depend on the application requirements. The use of conductive particle elastomer composites is explored in this work due to the customisability of the electromechanical characteristics. A core part of this thesis is understanding the behaviour of conductive particle elastomer composites for their use as a range of EAP-based sensing and actuating devices. The characteristics that make conductive particle elastomer composites (CPECs) ideal for soft sensor and actuator devices often include, low stiffness, controllable conductivity, controllable piezoresistivity, mouldable, 3D printable, low toxicity, durable, inexpensive, easy to obtain, simple fabrication process, and sustainable[123, 129–131].

### 2.5.1 Fabricating Conductive Particle Elastomer Composites

Before exploring the known conduction and piezoresistive mechanisms and models for CPECs, it is important to understand how the fabrication process of a CPEC may affect its physical structure.

CPECs are made by dispersing conductive particles through a curable liquid elastomer matrix. To change the electromechanical properties of the material, the dispersion of the conductive

particles throughout the matrix can be optimised through various methods. To minimise the agglomerations of primary conductive particles often a sonication step is completed. This involves a mixture of the conductive particles and a liquid, usually in the form of a solvent, to be placed in a ultra-sonication bath.

The sonication bath performs a frequency sweep and it has been shown that sudden implosion cavitation near the agglomerates help cause the separation of the agglomerates into their primary particles[132, 133]. The degree of deagglomeration and dispersion is affected by various factors including sonication time, frequency of oscillations, oscillation intensity, particle wettability, and liquid matrix viscosity[133, 134].

This sonication usually occurs before the the particles are added to the elastomeric matrix due to the large viscous damping effects of liquid elastomers. The next step involves mixing the dispersed conductive particles throughout the liquid elastomer, this can be done using a variety of mixing methods, including a planetary mixer, magnetic mixer, screw mixer, static mixers, amongst others [131, 135–137]. During the mixing process often the liquid solvent used in the dispersion stage is evaporated, leaving only the curable elastomer and the conductive particles. Although often impurities and voids are a by-product of the previous processes which can give undesirable qualities.

When sufficient mixing of the liquid elastomer and conductive particles have been completed the material is formed into a desired final shape using advanced additive manufacturing methods [117, 125, 138–142] or traditional moulding [143] or film making techniques [144]. During the moulding process the material undergoes a form of curing, such as UV, catalysed, or moisture curing. If the composite material has not already been integrated into a device containing electrodes and other mechanical support structures these are integrated at the end of the process.

### 2.5.2 Conductive Particle Elastomer Conduction Mechanisms

Depending on the fabrication process stages stated in Section 2.5.1 for fabricating CPECs, the dispersion of conductive particles will always vary.

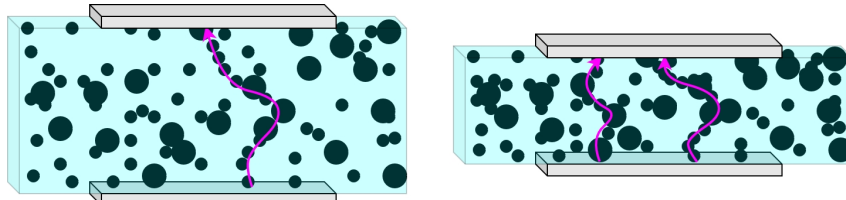


FIGURE 2.12: Two grey highly conductive electrodes across a CPEC cuboid showing enlarged black conductive particles within a blue polymer matrix. Left: An uncompressed CPEC. Right: A compressed CPEC.

Some of the physical features of these conductive percolation networks can be quantified and directly relate to the macro-level electromechanical properties of the material. Such characteristics of a conductive percolation network include, the type of conductive particle(s) used, particle dispersion, the elastomeric matrix, and any impurities or voids. The aspect ratio of a conductive particle filler can drastically change the conductivity and piezoresistivity of a CPEC. For example the aspect ratio of carbon nanotube particles (CNTs) is very large compared to that of regular carbon black (CB) particles, this has been shown to give improved conductivity for smaller weight volume percentages[145, 146], among other electromechanical property changes.

Also the inherent particle conductivity a core parameter to consider when choosing a conductive particle composite.

Conductive particle dispersion is an important characteristic of CPECs when optimising the electrical properties of a CPEC. Particle dispersion includes the inter-particle distance distribution[131], particle agglomeration distribution[135], particle isotropy/anisotropy [147], and sedimentation[148]. The filler elastomer matrix also contributes to the piezoresistive effect, through it's viscoelasticity, elastic modulus, and dielectric permittivity within the CPEC.

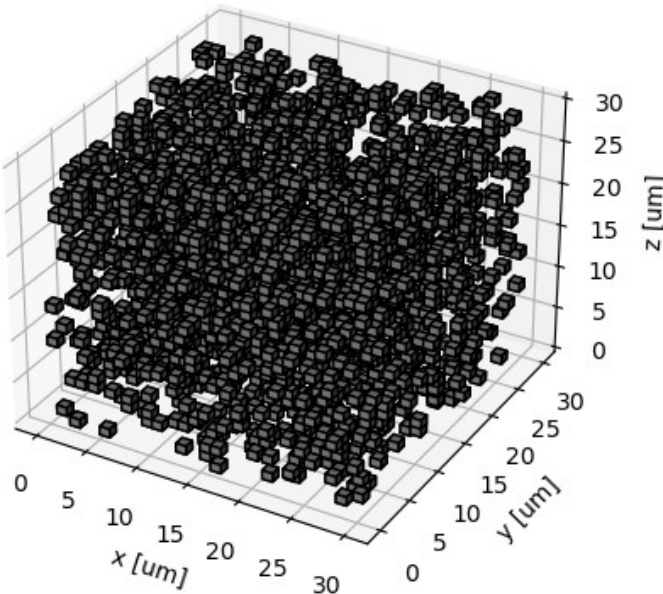


FIGURE 2.13: Example of a randomised cube percolation with a volume percentage of 8% of  $1\mu\text{m}$  particles

Microscale models for CPECs and the relationship between particle and electric charge motion are often computationally heavy, overly idealised, and non-invertible [149]. A microscale model example can be seen in Figure 2.13. However, microscale modelling of CPECs may give insight into understanding complex physical phenomena that may relate to the macroscale models made for CPECs. An alternate method for modelling CPECs is the formation of macroscale models[150].

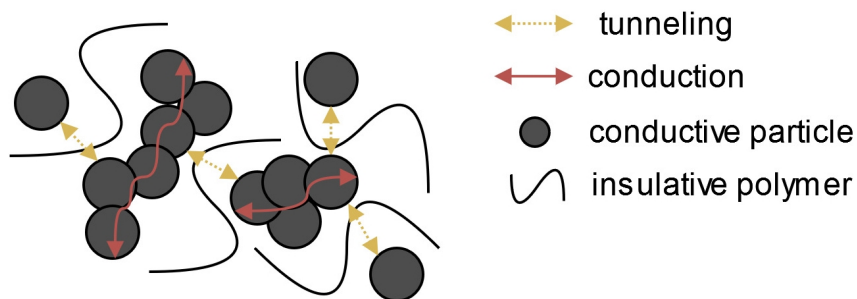


FIGURE 2.14: Electrical conduction and tunneling representation diagram.

Electrical DC conduction through a CPEC occurs via two main mechanisms, electrical conduction and quantum tunneling [151–154]. Electrical conduction uses the conduction band electrons

shared by adjacent atoms to allow movement of electrons throughout chains of cascading these conductive atoms. The second mechanism of conduction is through quantum tunneling which is stochastic in nature and allows for conduction through insulative boundaries between the percolative network of conductive particles [155, 156].

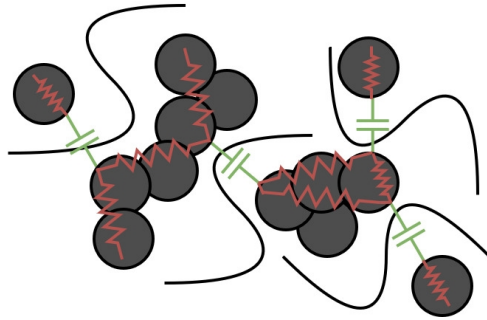


FIGURE 2.15: AC conduction RC network representation diagram.

The a CPEC can be modelled with an RC network as shown in Figure 2.15. Electrical AC conduction can occur through a CPEC through capacitive means depending of particle spacing with a decrease in reactance becoming more prominent for composites near the percolation threshold[130].

## 2.6 Literature Review Conclusions

The original purpose of this thesis was to develop novel sensor and actuator technology that mimics the pressure mapping capabilities of human skin and combine this with the actuation properties of human muscle. Through this review of current literature, several key conclusions can be drawn that will lay the foundational knowledge for the rest of this work.

The review of biological skin has revealed quantitative parameters that define its mechanical and sensory capabilities. This review highlighted mechanical characteristics such as the elastic modulus, viscoelastic creep, and surface area, as well as functional properties like spatial and temporal resolution. These factors provide a foundation for designing artificial skin that can replicate or even surpass the sensing functions of soft human skin. The review on pressure mapping technologies was then completed showing a range of different transduction methods for similarly soft sensing domains, showing that replicating human mechanoreceptor sensation is a multifaceted problem. Human skin uses various mechanoreceptors with different qualities and trade-offs and similarly different pressure mapping technologies use different pressure transduction methods each with different performance characteristics and limitations. The parallel review on biological and artificial muscles showed that DEAs and HASEL actuators are promising technologies for mimicking biological muscle quantitatively. Although characteristics common to both technologies such as high actuation voltage and limited device lifetime limit the applications of them.

The thesis has converged on using CPECs to fabricate EAP sensor and actuator devices, hence a brief literature review highlighting CPEC fabrication techniques and electromechanical characterisation has been given. These composites exhibit beneficial properties like flexibility, tunable electromechanical behavior, and ease of fabrication, which make them suitable for integrating into soft robotic systems. However, challenges such as achieving uniform particle dispersion, minimising agglomeration, and optimising the conductive network for stable long-term operation are still active areas of investigation.

This literature review has given a brief overview of some of the devices and theory related to the thesis, throughout the thesis there will be more background theory given on a need-to-know basis for each chapter.

## Chapter 3

# Characterising Non-Linear Behaviour in Carbon-Black Elastomer Nano-Composites

### Abstract

This work has converged on using conductive particle elastomer composites (CPECs) as the electroactive base for creating improved sensor-actuator devices, due to their superior qualities outlined in the Literature Review. Understanding the dynamic characteristics of a CPEC is critical for using the material in dynamic sensor and actuator devices. Although the fabrication of a CPEC can be simple, the characterisation and optimisation of such a material for various soft robotic applications can require complex models and display non-linear time-dependent behaviour. In this work we uncover several repeatable mathematical relationships seen within the material concerning dynamic time series behaviour between tensile strain, stress, and resistance data.

First a linear quasi-static model is generated to give a simple formula for estimating strain given a resistance input for a steady state system. Then the time-dependent and dynamic phenomena of the CPEC material were explored. Analogously to fitting stress relaxation to a two-unit generalised Maxwell mechanical model, this work has fitted the resistive relaxation seen after a strain step input to a three-unit generalised Maxwell model. No linear correlation was found between resistive and stress relaxation. For a strain falling edge signal, a positive correlation was found between increased strain-rate and the resistance peak seen in the tensile specimens. Similarly a positive correlation was found between the pre-strain amplitude and the resistance peak generated, for a strain falling edge signal. We have demonstrated a technique to reduce apparent resistance measurement drift in resistance experiments by using a switched AC current source instead of DC.

All of the behaviours determined in this work set a foundation for understanding the viscoelastic electromechanical nature of a CPEC for further development of the material in more complex sensor and actuator systems. Future work aims to generate a non-linear inverse model to more accurately determine the strain of the CPEC material given a resistance input. With this inverse model the CPEC material would be suited to a plethora of biomedical and agricultural applications which require delicate and non-toxic sensing systems.

### 3.1 Introduction

As discussed in the Literature Review chapter, conductive particle elastomer composites are desirable for soft sensor and actuator applications for a variety of reasons. However, it is crucial to understand the electromechanical behaviour of these composites if we wish to create complex control systems with such materials. Although conductive particle elastomer composites (CPECs) are simple in concept, consisting of dispersed particles through an elastomer matrix, the electromechanical behaviour is not well understood on a macro or micro-scale. This chapter will focus on only tensile stress of the specimen, and how it relates to the electrical resistive relaxation. Compressive characterisation and modelling is covered in the subsequent chapters. This work endeavours to understand the material behaviours of carbon black silicone rubber composites on a macro-scale to help create better inverse models so that the material can be used more accurately for stress/strain sensors.

#### 3.1.1 Background

Carbon nanoparticle-silicone elastomer composites are stretchable conductive materials with diverse applications such as, highly elastic strain sensors [52, 143, 157], dielectric elastomer actuators [158, 159] and electromyography electrodes [143, 160, 161]. Understanding the dynamic resistive relaxation characteristics of carbon black (CB) silicone rubber (SR) elastomer composites would improve performance in fields which require high efficiency of space, power and accuracy, such as the devices used in biomedical and aerospace fields. Unlike many common strain gauges, CBSR composites can have strains of over 300% without yielding [162] depending on the type of SR and CB used and the method of fabrication. This strain and the strain used in this work is higher than commonly used constantan strain gauges, which typically have a maximum strain of  $\pm 3\%$  [163], with traditional metal alloy based strain gauges often having significant plastic deformation after less than  $10^4$  cycles [163] at this 3% strain.

Some characteristics of CBSR composites which make it suitable for strain sensors include that, the material is relatively inexpensive, readily available, non-toxic, bio-compatible, and can have a high gauge factor. Other alternative composite conductive particles, such as carbon nanotubes (CNTs) [164, 165] and metallic particles [109, 166], have been seen to be more carcinogenic than CB alternatives [167–169]. The fabrication of CBSR composites requires a degree of optimisation to ensure that the carbon particles are adequately dispersed to ensure high conductivity and high yield strength of the material. More importantly the homogeneous dispersion of CB particles means improved repeatability of experimental results and more accurate models for the eventual applications of CBSR composites. A comprehensive model of how the resistivity changes with strain has not yet been developed.

While previous work from our research group [170, 171] has focused on the response to quasi-static and low-strain-rate behaviour, these materials show dynamic effects where a significant resistance strain-rate relationship is present. The main characterisation investigated in this work for CBSR sensing involves understanding the relationship between the mechanical stress relaxation, electrical resistive relaxation and strain in time. A difference in time constants between the stress and resistive relaxations have been noted before in literature [164, 165, 172, 173], but never accurately modelled with the physical theory explained. Mersch et al. [174] have classified several transient ‘shoulder’ events and their related deformation events, compressive, tensile, and bending. These transient peaks have been observed by several researchers using the similar CBSR materials, however there is no conclusive mathematical model relating these transient peaks to strain in time. An understanding of this resistive relaxation and other

transient phenomena would mean an accurate model could be made to predict the relationship between stress, strain and resistance within a CBSR composite.

Determining a stress-strain-resistance model would also allow us to understand the limitations of using this composite in sensing and actuation applications, so that the material can be used simultaneously as an actuation excitation electrode and a strain sensor. Understanding these characteristics may give rise to new applications of the composites material, for example, if the resistive relaxation properties of the material were known, it could be used as a mechanically activated timing device. An oscillatory flexible dynamic circuit has been demonstrated when mimicking the motion of a caterpillar as shown by Henke et al. [158], where the resistive relaxation modelling is useful for more accurate electrical circuit dynamics. The theory behind mechanical stress relaxation is widely known and has been modelled using a variety of mathematical models [14] depending on the material modelled.

It is known that silicone rubber composites are viscoelastic materials and clearly exhibit the three traits of a viscoelastic material [14]: stress relaxation, strain creep, and stress-strain hysteresis. Stress relaxation is an effect observed when a step input of strain is applied to a material and there is a transient stress decay response which converges to a steady state value. A commonly used model for viscoelasticity is the generalised Maxwell body model of order  $n$  shown in Figure 3.1.

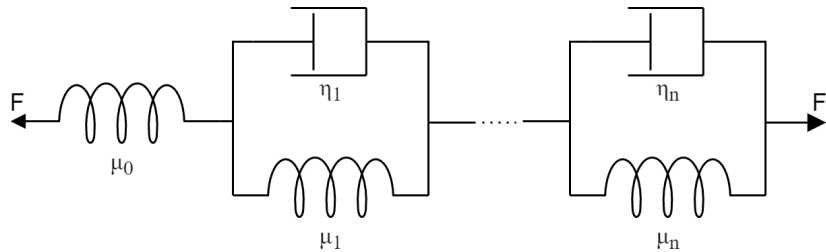


FIGURE 3.1: Mechanical spring dashpot diagram of the generalised Maxwell body model adapted from Fung et al. [14]

Where  $F$  is the force applied to the material, and  $\mu$  and  $\eta$  values represent the spring and damping component constants, respectively. The stress relaxation function for this model is found in Equation 3.1, for,  $n$ , serial repeating units.

$$G(t) = a_0 + \sum_{i=1}^n a_i \cdot e^{-t/\tau_i} \quad (3.1)$$

Where  $a_0$ ,  $a_i$  are the magnitudes of relaxation and  $\tau_i$  are the relaxation decay time constant components. All of the constants  $a_0$ ,  $a_i$ , and  $\tau_i$  are functions of  $\eta$  and  $\mu$ .

We initially assume that there is a relationship between the stress relaxation and resistive relaxation of the material. However, the generalised model can easily over-fit the data, if  $n$  is too high. To mitigate over-fitting, a generalised model with the minimum amount of repeating units while maintaining a high  $R^2$  is used.

Few mathematical models describing the viscoelastic-resistance relationship have been formulated. Laaraibi et al. [175] developed a time-invariant model which uses a relaxation parameter to account for the viscoelastic effect. Mersch et al. [174] developed a model using transverse and longitudinal viscoelastic parameters to model a similar CBSR material. Both models show promise towards creating a more comprehensive physical model. However, the both models aren't tested for a randomised range of input strain signals.

## 3.2 Methods

The core experimental part of this chapter will be described from composite fabrication through to simultaneous strain tensile tests and resistance measurements. This is followed by the analysis data for resistance-strain phenomena, to quantitatively match the phenomena these to black-box and viscoelastic models.

### 3.2.1 Composite Fabrication

The CBSR composite was composed of Vulcan XC-72 CB powder (Fuel Cell Store, Bryan, USA) and two part Pt cured Dragon Skin 10 NV SR (SmoothOn, Macungie, USA). The CB powder has an average particle size of 50 nm and typical bulk density of 96 kg/m<sup>3</sup>. This grade of SR was chosen due to the following characteristics low elastic modulus,  $E$ , of 186 kPa tensile strength,  $\sigma_Y$ , of 2.75 MPa, and a low mixed viscosity,  $\eta$ , of 6,000 cps [176]. This  $E$  value is within the range of human skin tissue and the low  $\eta$  facilitates material processing in potential future applications with additive manufacturing.

The volume resistivity of pure CB powder itself is between  $10^{-1}$  and  $10^2 \Omega \cdot \text{cm}$  depending on how densely the particles are packed and the purity of the CB [52]. The ability of a CB matrix embedded within a highly insulative SR substrate to become conductive is determined mainly by the dispersion of the CB particles, and the tunneling that occurs between conductive CB and insulative SR bodies within the material volume [52, 165]. The composite being created must be highly conductive without compromising the elastic modulus and yield strength of the material. From percolation theory observed in literature [52] there is a threshold volume percentage of CB required to ensure that conductivity is maintained with certainty throughout the composite volume within the linear volume resistivity region. The percolation threshold for composite used in this work was difficult to predict due to the unknown configurations of agglomerations and dispersion of CB particles within the composite material. Empirically it was found that a CB volume percentage of 7.5% or greater meant the composite material had a resistivity of less than 3.5 k $\Omega \cdot \text{cm}$  consistently with the fabrication method used.

The first fabrication step was to mix the CB nano-powder with part A of the liquid SR using a KK-50S planetary mixer (Kurabo, Osaka, Japan). A mixing function was used with specific rotational velocities and times for each axis, which was well suited towards de-aeration and viscous particle mixing. The composite mixture was then mixed with the cross-linker part B of the liquid SR using the same planetary mixing function to ensure adequate dispersion of the CB particles throughout the SR volume.

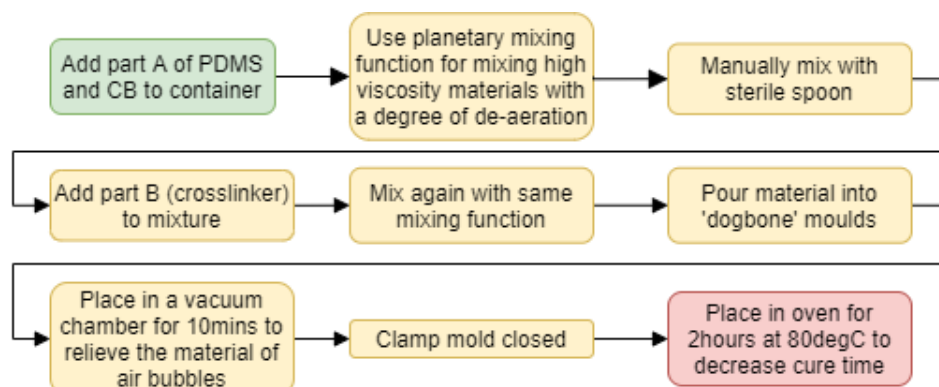


FIGURE 3.2: The steps involved in creating the CBSR composite material

For the fabrication of the CBSR specimens, a standard dog-bone shaped mould was developed for the mixed CBSR to cure in, based on ASTM standard D412 [177]. Before the mould was clamped shut the composite filled mould was immediately placed in a vacuum chamber for ten minutes to de-aerate the still liquid, curing CBSR mixture. The specimen was placed in a lab oven at a temperature of 80 °C for a two hours to accelerate curing. It has been shown that an increase in curing temperature for two part SR increases elastic moduli and decreases yield strength [178, 179].

### 3.2.2 Material Imaging

To determine how the microstructure may effect the macro-behaviour observed in the following electro-mechanical testing of the material, various optical imaging methods were used, including optical microscopy, scanning electron microscopy (SEM), and Raman spectroscopy.

The initial step was to observe the fabricated CBSR composite specimen using a stereoscopic microscope to view the internal structure of the CBSR composite specimens as shown in Figure 3.3.

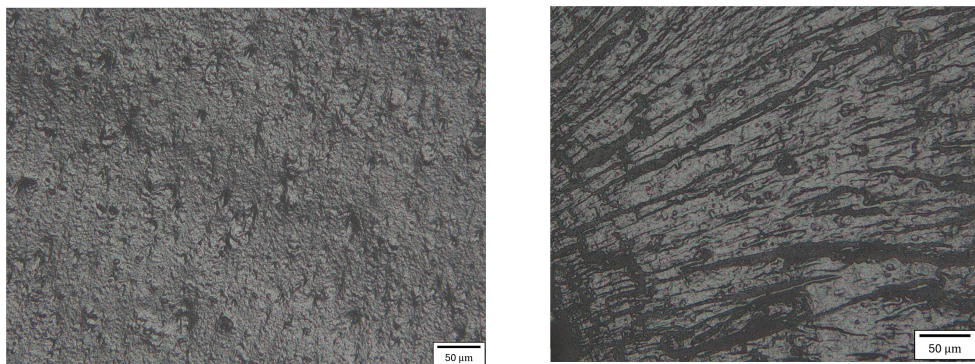


FIGURE 3.3: Microscope images at x20 magnification of a CBSR specimens with cross-sections made by; Left: Cutting with a scalpel. Right: Inducing an embrittlement fracture.

It is known in literature that preparing flat planar surfaces through elastomer composites for micro- and nano-scoptic imaging is non-trivial [180]. Due to the silicone material elasticity and a low embrittlement point of -60 to -70 °C , traditional polymer composite specimen machining methods cannot be used if a flat surface is desired. Because of the lack of water content in the CBSR composite traditional biological specimen preparations methods are also not feasible.

Two methods were trialled to prepare the cross-sectional surface of the specimen for imaging, a scalpel cut and an induced embrittlement fracture. The scalpel cut was completed at room temperature conditions aligned vertically with the specimen. The induced embrittlement fracture used required extreme cooling by pouring liquid nitrogen over the specimen for 2 minutes, then snapping the specimen in two.

The induced embrittlement fracture shown in Figure 3.3 shows a very rough surface finish due to the many localised stress concentrations formed around voids and CB particles in the composite, and the non-crystallinity of the elastomer. The scalpel incision method showed an improved surface finish with a low amplitude undulating surface finish.

To observe smaller features such as voids and CB particle dispersion within the CBSR specimen the Apreo 2S FEG-SEM (Thermo Fisher Scientific, Waltham, USA) was used. Initially the CB particles were imaged validating their nominal primary particle size and displaying the

agglomerated structure as shown in Figure 3.4. The nominal particle size was found to be  $48 \pm 20$  nm randomly sampling and averaging over 30 particles observed via SEM images. The top surface edge of the CBSR specimens were imaged to highlight the difference in surface roughnesses. Finally the dispersion of the CB particles was attempted, however due to surface charging of the relatively highly insulative silicone matrix the image resolution was limited as shown in 3.4.

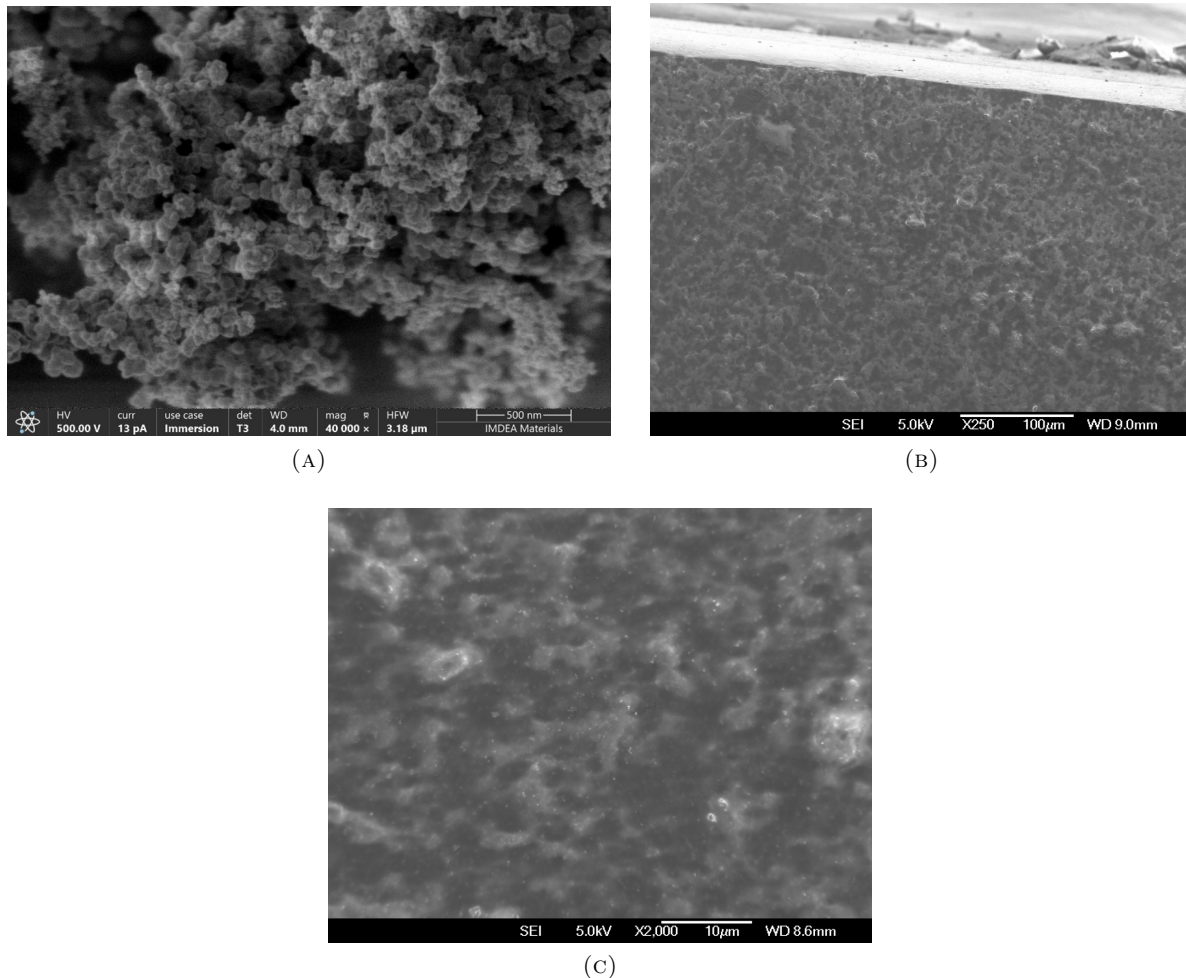


FIGURE 3.4: SEM images of; (A): CB agglomerated particles  $\times 40,000$ . (B): CBSR cross-section top surface edge site 1  $\times 250$ . (C): CBSR cross-section site 1  $\times 2000$ .

When measuring CBSR specimen for bulk electrical properties a reliable electrical connection to the material's conductive matrix is necessary. Obtaining high conductivity connection between the measurement electrodes and the material volume was investigated. The surface of the cured CBSR specimen is smooth and has proven highly insulative upon measurement, indicating that there is a thin insulative silicone film around the edges of the specimen as shown in Figure 3.4b. This surface insulation film existed in each side of the specimen, potentially indicating that the viscosity of the SR matrix is high enough to prevent the CB nanoparticles from settling on the bottom surface of the mould used. The white dots shown in Figure 3.4c represent carbon particles throughout the SR matrix. Resolution was limited due to the insulative SR matrix charging from the electron beam. This resolution discrepancy is apparent when comparing to the more conductive CB particles in Figure 3.4a.

To determine the presence and dispersion of CB particles on the surface of the CBSR specimens a inVia confocal Raman microscope (Renishaw, Wotton-under-Edge, United Kingdom) was used. A 532 nm laser with a was used in the Raman microscope. Several surface and cross-sectional images were taken showing a considerable difference in the CB-SR ratio as shown in Figure 3.5. The prominent  $1350\text{ cm}^{-1}$  and  $1600\text{ cm}^{-1}$  intensity peaks indicate the presence of CB and the prominent  $490\text{ cm}^{-1}$ ,  $2906\text{ cm}^{-1}$ , and  $2965\text{ cm}^{-1}$  peaks indicate the presence of SR [181, 182].

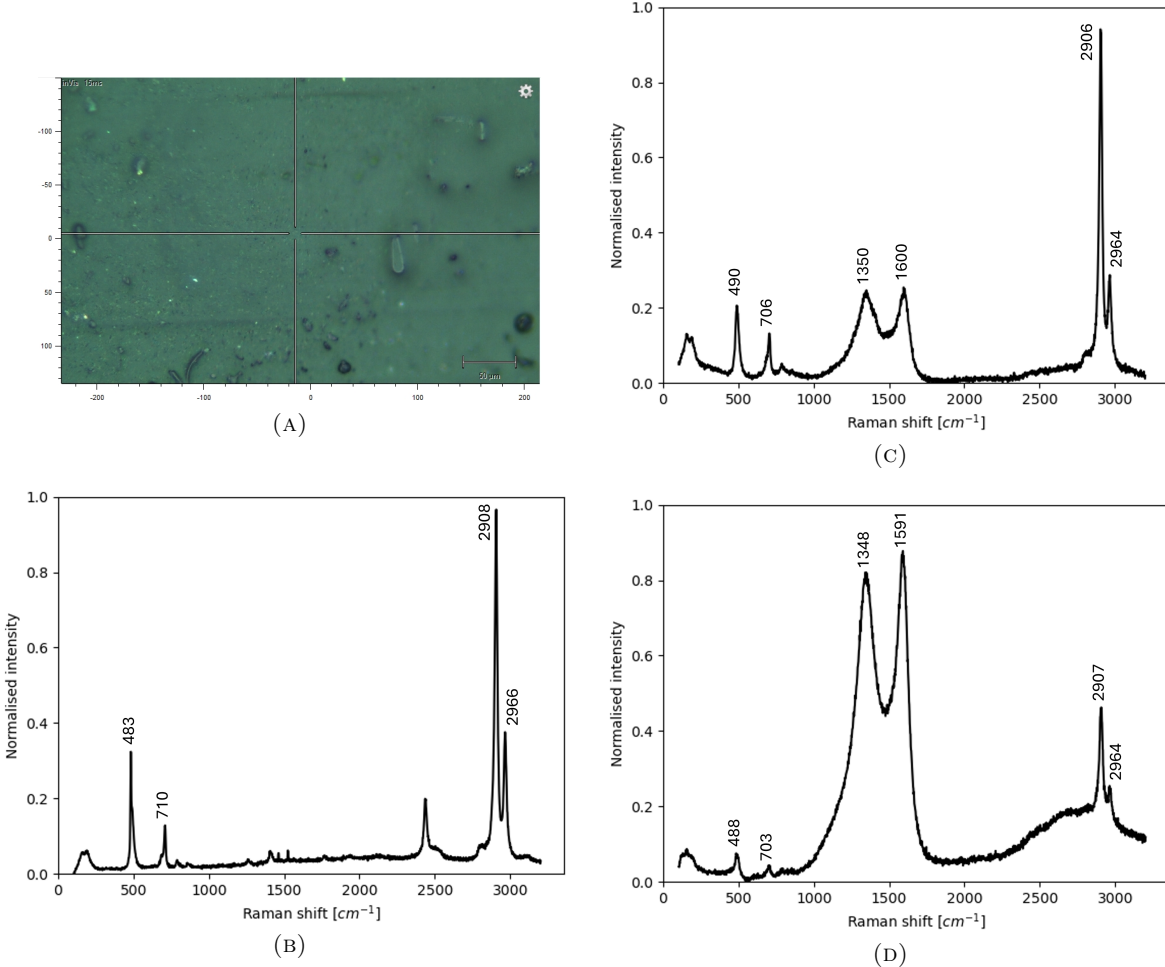


FIGURE 3.5: (A): Typical screenshot from the focused Raman microscope. Normalised Raman spectrum of (B) the plain SR. (C) the top surface of CBSR specimen. (D) the cross-sectional surface of CBSR specimen.

These plots in Figures 3.5b - 3.5d show that surface electrodes will have a smaller chance of obtaining a reliable connection to the conductive network to the internal the CBSR composite, due to the low CB particle content measured at the surfaces on the specimens.

### 3.2.3 Stress-Strain-Resistance Measurement

A custom test measurement device was made for measuring the desired characteristics of the CBSR material, so that parameters driving the data collection such as the current source and strain profile could be easily customised to suit the experiment. The strain, stress, and resistivity of the specimen were measured in parallel. The setup included the use of a 500 g TAL221 loadcell (HT Sensor Technology Co. Limited., Xi'an, China) in combination with a linear actuator stage driven by a NEMA23 stepper motor and a 2634B Keithley source measurement

unit (SMU) (Tektronix, Beaverton, USA). The loadcell was found to have a resolution of  $\pm 30$  mN and the linear actuator stage used a G201x micro-stepper controller (Geckodrive, Santa Ana, USA) allowing for  $40 \mu\text{m}$  steps.

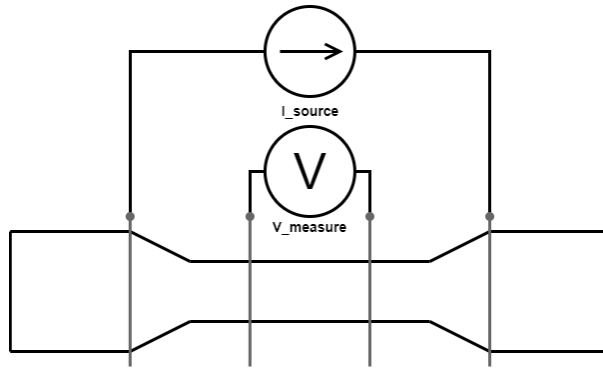


FIGURE 3.6: The composite dog-bone test specimen pierced by 4 metal pin electrodes. The outer and inner electrodes connected to an SMU current source and voltmeter respectively

The four-wire method uses four pin electrodes as seen in Figure 3.6. The four-wire method applies a constant current source through the outer electrodes and uses a voltmeter on the inner two electrode to determine the resistance of the specimen. The four-wire electrode configuration exhibited a larger signal-to-noise-ratio (SNR) compared to the two-wire alternative for resistance measurements. Four-wire pin electrodes were selected because they resulted in minimal specimen deformation, exhibited a high measurement SNR, no slip, and the electrode can pierce through the specimen which ensured a constant electrode impedance. The inner pin electrodes were symmetric about the centre and placed 20 mm apart with the outer pin electrodes being 40 mm apart as shown in Figure 3.7.

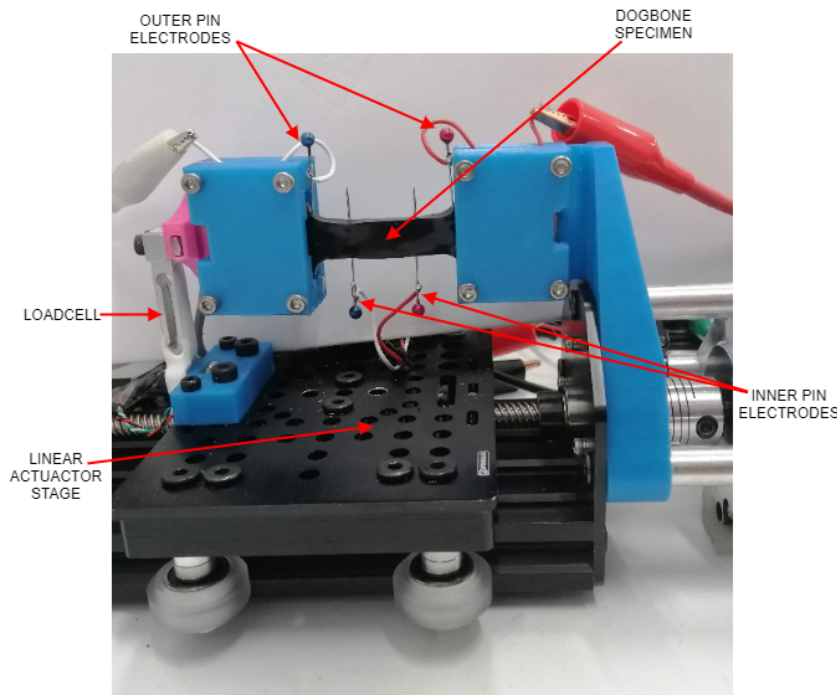


FIGURE 3.7: Photo of test measurement setup

The dogbone specimen was held in place using clamps with an a 3D pyramidal array surface. The specimen clamp strain was calculated using the specimen Poisson's ratio and the maximum expected tensile experiment strain; to ensure the specimen would not slip, and ensure minimal deformation to the specimen.

The measurements were completed using controlled sinusoidal, saw-tooth, and pulse trains of strain to ensure repeatability of the models were consistent across varying experimental parameters. If this material is used as a sensor the model fitted to the stress relaxation must hold over many consecutive tensile strain events. As these materials are intended as large strain sensors, the main strains tested in this work were ranged between 0 and 30%, with a strain-rates ranging from 0 to  $6.67 \% \cdot s^{-1}$ .

All data was captured through serial interfaces and logged on a PC with a python-based program. An open source G-code platform GRBL was used to control the motion of the linear actuator. The PyVISA library was used to obtain all of the measurement data and to send commands to measurement devices. A calibration procedure ensured that the stress and strain of the specimen was always zero'd before each experiment. The functional architecture of the system is shown in Figure 3.8.

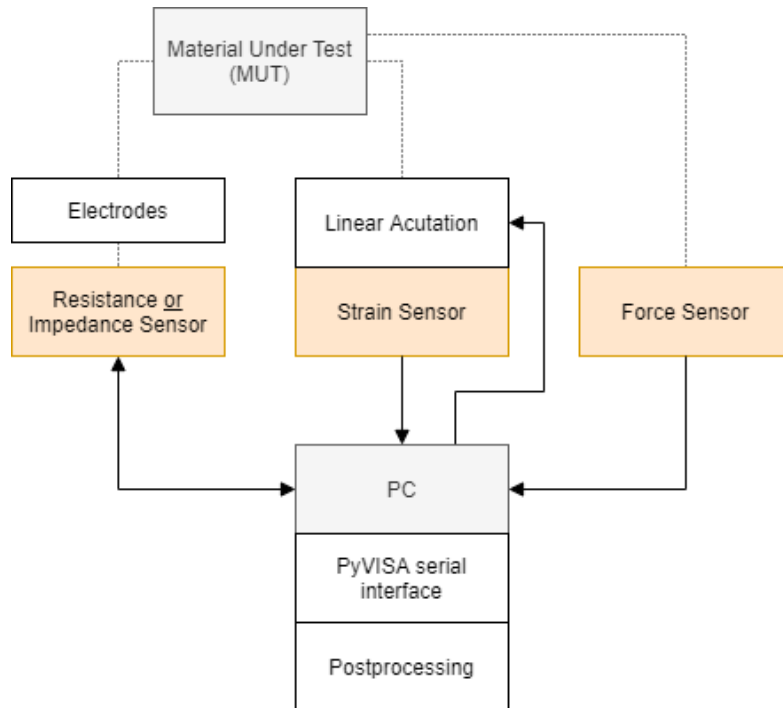


FIGURE 3.8: System architecture for the electromechanical tensile test rig showing data/physical connections

### 3.3 Results and Analysis

The CBSR composite material has shown complex nonlinear behaviour in previous literature as discussed in Section 3.1, hence a piece-wise approach to modelling the CBSR composite has been taken to describe the electromechanical dynamic behaviours of the material. To understand the transient behaviour of CPECs several dynamic repeatable electromechanical characteristics of CBSR have been classified and mathematical representations fitted. This section aims to provide repeatable mathematical relationships for various phenomena towards creating an overarching model which combines each of the phenomena.

### 3.3.1 Stress-Strain and Viscoelasticity

All of the specimens fabricated indicated a degree of viscoelasticity shown by the hysteresis seen when loading and unloading the material with 30% tensile strain in Figure 3.9. The 0, 7.5, and 10 w.t.% CB specimens have average elastic moduli, as measured in the loading phase, of 205.2 kPa, 321.4 kPa, and 342.1 kPa, respectively.

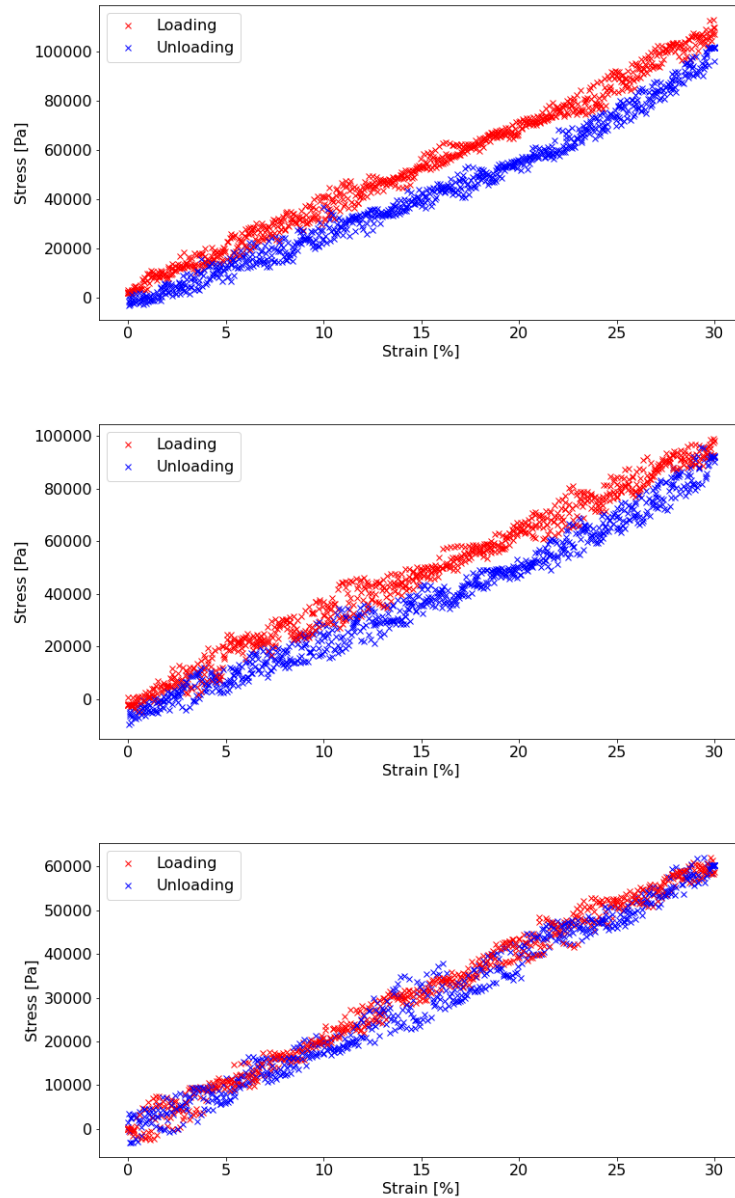


FIGURE 3.9: The loading and unloading of 30% strain on a composite test specimens with CB weight percentages from top to bottom of 10%, 7.5%, and 0% with data collected over five loading and unloading cycles

### 3.3.2 Quasi-Static Tensile Resistance-Strain

To understand how the material could be used for a low-frequency response application the underlying steady-state relationship between resistance and strain was found by producing a

quasi-static linear resistance-strain formula for strains between 0 to 30% strain. Data was gathered using steady-state measurements from four separate tensile strain pulses performed on the same CBSR specimen as shown in Figure 3.10.

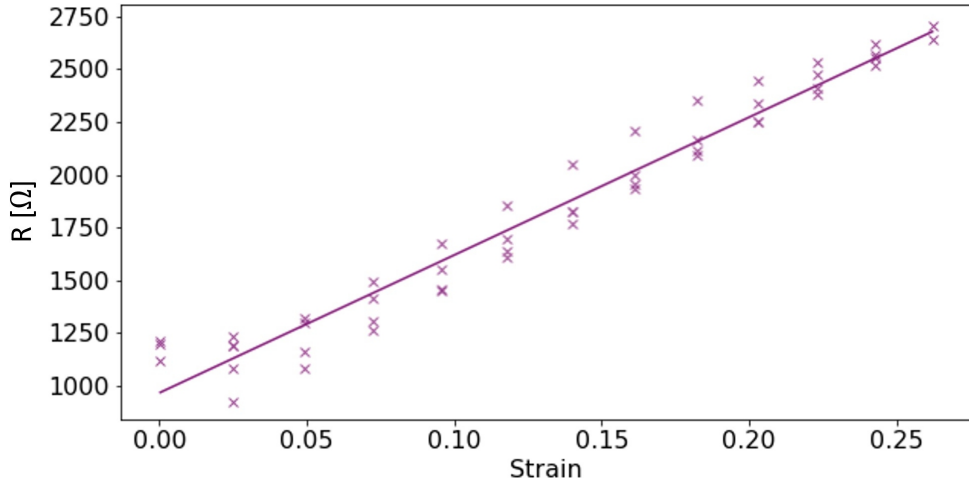


FIGURE 3.10: Linear quasi-static resistance-strain fit for 7.5 w.t.% CBSR specimen

The fitted parameters for the linear quasi-static model are given in Equation 3.2.

$$R = 6530 \cdot \varepsilon + 970 \quad (3.2)$$

### 3.3.3 Dynamic Resistance-Strain-Rate Response

When using this material as a tensile strain sensor many applications will require a strain-rate superseding the capabilities of the quasi-static model given in Section 3.3.2 due to the resistive relaxation in the material characterised in Section 3.3.5. The dynamic characteristics of the CBSR material is investigated to find a relationship between the strain-rate and resistance. Several saw-tooth strain signal experiments were completed using four different strain-rates of 1.67, 3.33, 5, and 6.67  $\text{%.s}^{-1}$ . To avoid measuring a time-dependent relationship in stead of the desired strain-rate dependent relationship, each set of different strain-rates were repeated as shown in Figure 3.11.

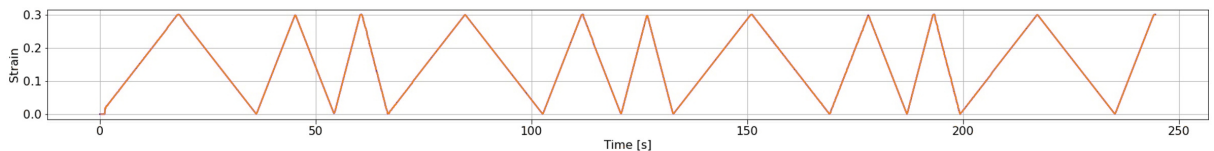


FIGURE 3.11: Strain input waveform for investigating strain-rate dependent resistance

The resulting resistance response exhibits a shoulder peak phenomena where a second peak is developed when suddenly decreasing the strain-rate. The resistance response is shown in Figure 3.12.

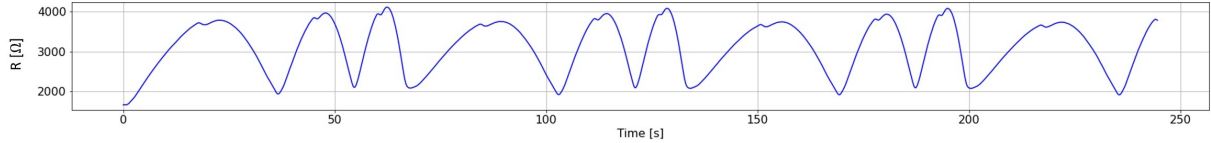


FIGURE 3.12: Resistance response from saw-tooth strain input Figure 3.11.

Hysteresis loops were used in Figure 3.13 to show resistance offset as a function of the strain-speed and simultaneously displaying the resistance hysteresis loops of different strain speeds.

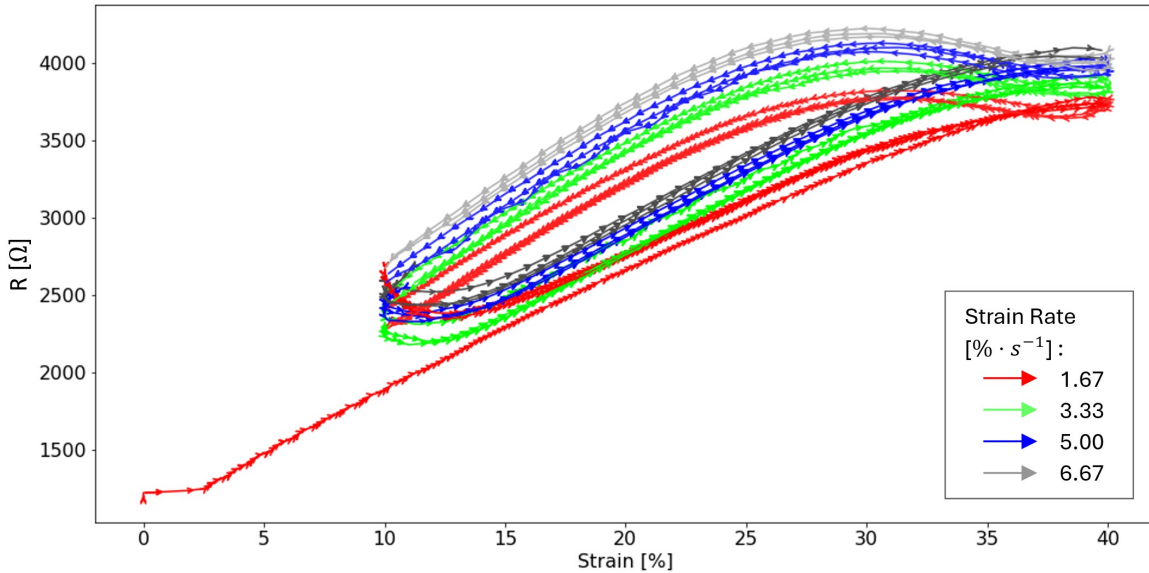


FIGURE 3.13: Resistance vs strain hysteresis loops from a saw-tooth strain input.

The material was pre-strained to mitigate non-linear effects that may arise near 0% strain. Using the  $1.67 \text{ \%}\cdot\text{s}^{-1}$  strain-rate as a reference the average resistance offset of the other three strain-rates tested were calculated as shown in Table 3.1.

TABLE 3.1: Strain-rate dynamic resistance offset comparison. Using S1 as the reference resistance loop.

Strain-rate #	S1	S2	S3	S4
$\dot{\varepsilon} [\text{\%}\cdot\text{s}^{-1}]$	1.67	3.33	5.00	6.67
$\Delta R_{S1} [\text{\%}]$	0	+5.0	+8.3	+10.7

### 3.3.4 Falling Edge Strain-Rate-Resistance

A narrow peak in the measured resistance has been observed in the collected data when during a falling edge. This peak is not present in the stress plot shown in Figure 3.14, hence is a proposed characteristic of electrical behaviour only as a function of strain as the change in resistance is assumed to be primarily due to conductive particle motion.

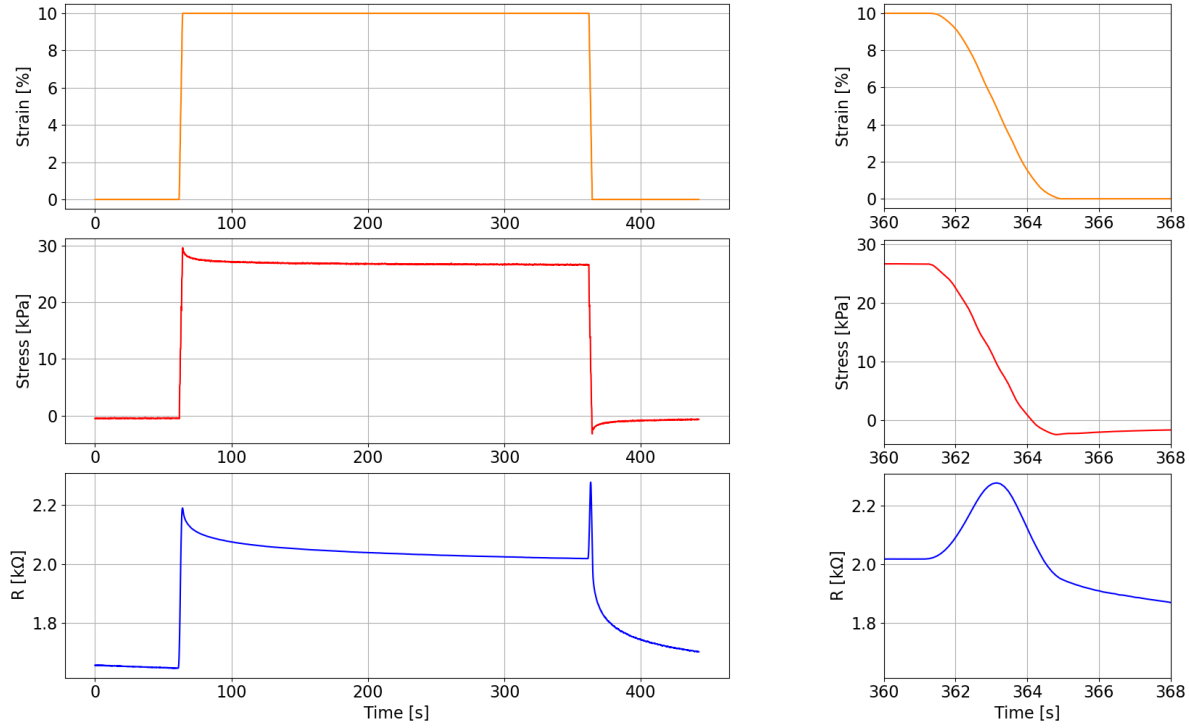


FIGURE 3.14: Left: Singular tensile strain pulse with resulting stress and resistance response.  
Right: Zoomed to highlight falling edge shoulder phenomena.

A parameter fit study has been completed to determine the resistance peak amplitude can be determined with a range of strain-rates. We can see a repeated phenomena in Figure 3.15 whereby the derivative of the resistance signal seems to be equal to the strain curve. The resistance peak curve,  $R_p$ , can be modelled with a second order polynomial. When differentiated, this peak gives a linear function in a similar form of the linear strain curve seen in Figure 3.15. Hence we form Equation 3.3 which relates resistance to strain as a function of time.

$$\frac{dR_p}{dt} = J(\varepsilon) \cdot t + c \quad (3.3)$$

where  $J$  is a function of strain,  $\varepsilon(t)$ , and  $c$  is an offset bias determined by the initial strain condition.

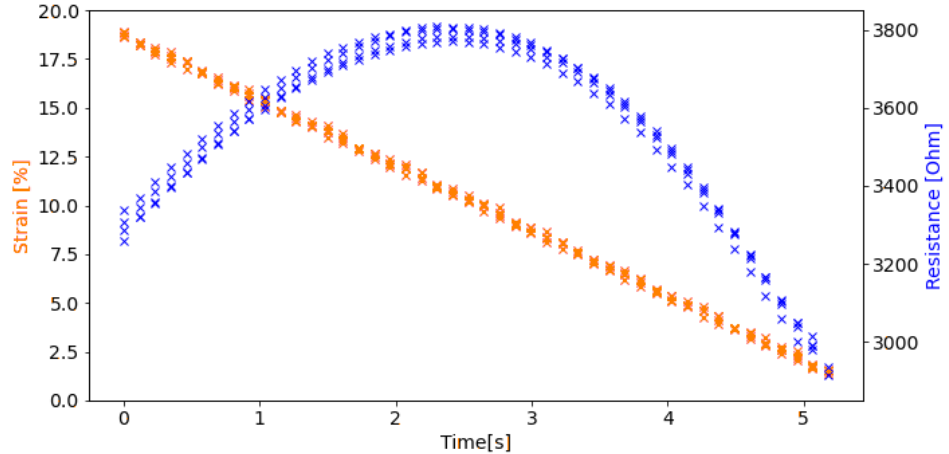


FIGURE 3.15: Strain-rate resistance relationship showing the specimen returning to a 0% tensile strain state from 10% at a strain-rate of  $3.33\%\cdot s^{-1}$  from four tests for a 7.5% CBSR specimen

To show the strain-rate resistance relationship, more strain pulse train tests of 20% strain were completed. Using 20% strain allowed observation of sufficient data points to observe a trend. The pulses had four repetitions with a range of strain-rates,  $\dot{\varepsilon}(t)$ , of 1.67, 3.33, 5.00, and  $6.67\%\cdot s^{-1}$ . Using a 7.5 w.t.% CBSR specimen we obtain a relationship that agrees with the strain resistance component equation 3.3. As  $\dot{\varepsilon}(t)$  increases through strain-rates in parallel with the magnitude of the resistance peak relative to the previous steady state of value resistance. Two formulae are fitting to the linear strain and resistance peak features given by Equations 3.4 and 3.5 respectively.

$$\varepsilon = A \cdot t + B \quad (3.4)$$

$$R_{peak} = C \cdot (t - D)^2 + E \quad (3.5)$$

The resulting plots fitting of the averaged data points for the strain and resistance peak curves are given in Figure 3.16.

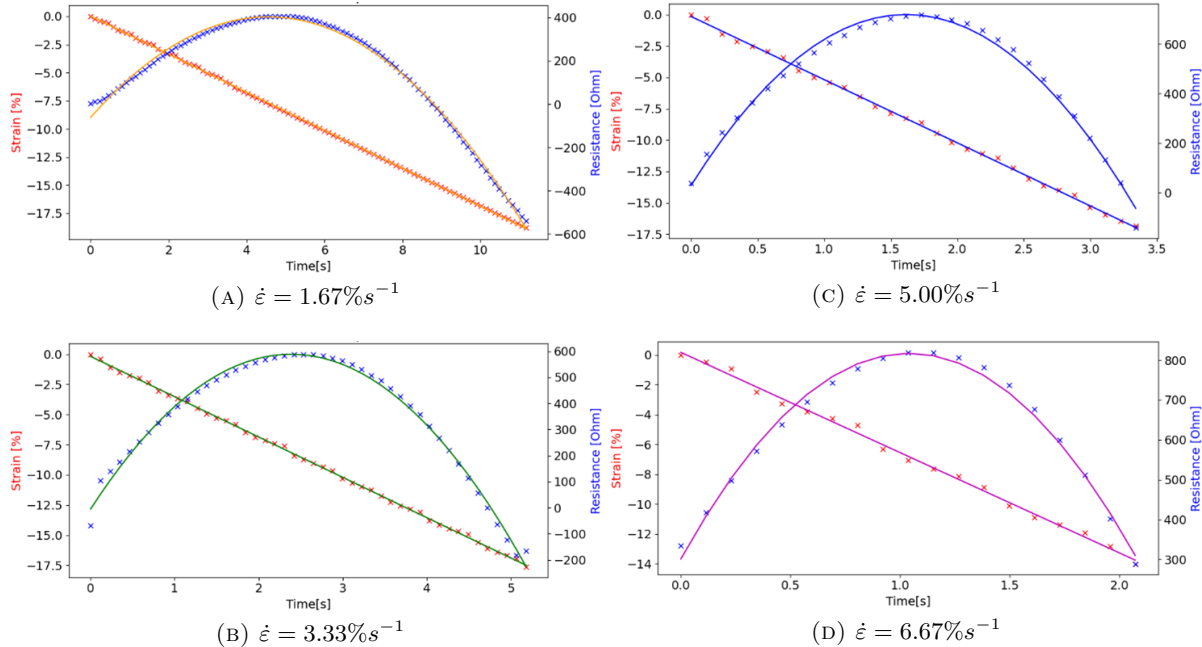


FIGURE 3.16: Fitting curves to a range of different tensile falling edge strain strain-rates.

TABLE 3.2: The fitted parameters for relationship between the specimen tensile strain-rate the resulting resistance peak for a strain signal falling edge.

Strain rate [%/s]	— 1.67	— 3.33	— 5.00	— 6.67
A ( $\times 10^3$ )	-16.83 $\pm$ 0.09	-33.40 $\pm$ 0.02	-50.34 $\pm$ 0.36	-66.82 $\pm$ 0.37
B ( $\times 10^3$ )	-0.45 $\pm$ 0.93	-0.69 $\pm$ 1.20	-1.77 $\pm$ 1.72	-0.13 $\pm$ 2.15
C	-22.10 $\pm$ 0.55	-103.19 $\pm$ 2.30	-250.40 $\pm$ 9.95	-478.81 $\pm$ 32.87
D	4.58 $\pm$ 0.02	2.37 $\pm$ 0.02	1.60 $\pm$ 0.06	1.12 $\pm$ 0.05
E	403.27 $\pm$ 13.52	586.87 $\pm$ 23.46	711.96 $\pm$ 7.19	809.21 $\pm$ 26.46

### 3.3.5 Resistive Relaxation Fitting

The initial model chosen to fit the stress and resistive relaxation data was the generalised Maxwell body model shown in Figure 3.1 with  $n = 3$  cascading elements using Equation 3.6 to fit the model. Fitting the data using Levenberg–Marquardt non-linear least square algorithm over 30 data sets showed an instability with the algorithm using this model. When feeding the previously fitted stress relaxation model parameters as initial conditions for the fitting of the next stress relaxation data set, the values of the parameters diverged exhibiting signs of overfitting. This divergence of the model parameters gave a large standard deviation showing the model was changing significantly each iteration of fitting. Hence a more simple model using Equation 3.1 with  $n = 2$  was used to fit the stress relaxation data to Equation 3.7 with lower standard deviation of the model constants. Conversely when the resistive relaxation model analogous to stress relaxation model, shown in Equation 3.8, was fitted to the resistive relaxation data there was a stable fit with a better goodness of fit.

The decay time constants of the two models are different with the resistance having an longer overall decay which can clearly be seen in Figure 3.17. Below in stress relaxation models  $G_{1,2}(t)$ , shown in Equation 3.6 and 3.7, the constants  $a_{0-3}$  and  $\tau_{S1-S3}$  represent the components of magnitude and time decay of the stress relaxation, respectively.

$$G_1(t) = a_0 + a_1 e^{-t/\tau_{S1}} + a_2 \cdot e^{-t/\tau_{S2}} + a_3 \cdot e^{-t/\tau_{S3}} \quad (3.6)$$

$$G_2(t) = a_0 + a_1 \cdot e^{-t/\tau_{S1}} + a_2 \cdot e^{-t/\tau_{S2}} \quad (3.7)$$

Analogously for the resistive relaxation function  $H(t)$ , the constants  $b_{0-3}$  and  $\tau_{R1-R3}$  represent the components of magnitude and time decay of the resistive relaxation, respectively.

$$H(t) = b_0 + b_1 \cdot e^{-t/\tau_{R1}} + b_2 \cdot e^{-t/\tau_{R2}} + b_3 \cdot e^{t/\tau_{R3}} \quad (3.8)$$

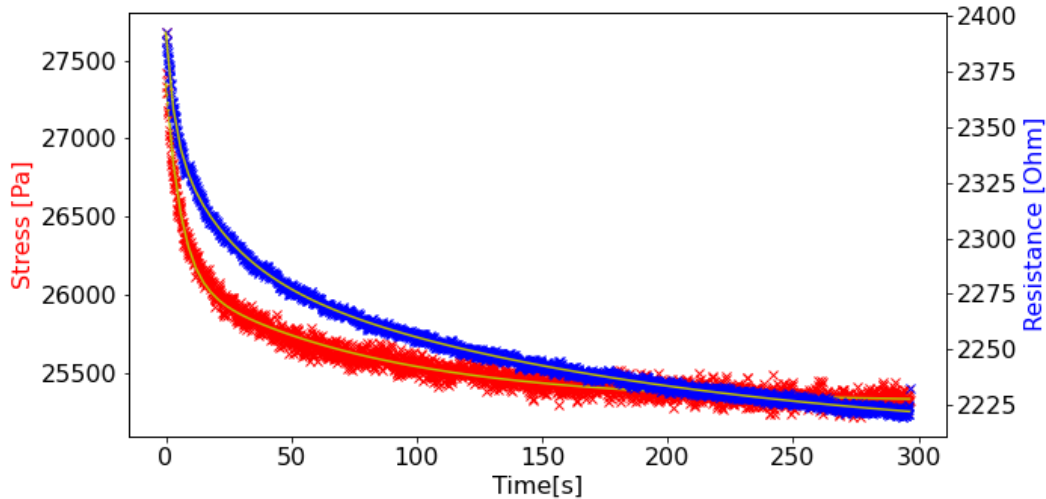


FIGURE 3.17: Comparing the relaxation decay time constants of stress and resistance for a 7.5 w.t.% CBSR composite after a 10% strain step input and fitting generalised maxwell body models to each.

The mean magnitude and decay time constants for the resistance and stress relaxations using 30 relaxation periods to fit the models to are given in table 3.5.

TABLE 3.3: Fitted constants and their mean,  $\mu$ , standard deviation values for 0%, 7.5%, and 10% CBSR composite specimens using Equation 3.7.

#### Stress Model Parameters

0 % CB Specimen	
Parameter	$\mu$
$a_0$	$20344 \pm 42$
$a_1$	$387 \pm 60$
$a_2$	$527 \pm 58$
$\tau_{S1}$	$72.1 \pm 23.5$
$\tau_{S2}$	$5.8 \pm 1.5$
7.5 w.t.% CB Specimen	
Parameter	$\mu$
$a_0$	$25363 \pm 33$
$a_1$	$802 \pm 43$
$a_2$	$1242 \pm 52$
$\tau_{S1}$	$71.0 \pm 9.5$
$\tau_{S2}$	$5.8 \pm 0.7$
10 w.t.% CB Specimen	
Parameter	$\mu$
$a_0$	$32303 \pm 165$
$a_1$	$1071 \pm 54$
$a_2$	$1649 \pm 47$
$\tau_{S1}$	$84.1 \pm 10.6$
$\tau_{S2}$	$6.5 \pm 0.7$

TABLE 3.4: Fitted constants and their mean,  $\mu$ , and standard deviation values for 0%, 7.5%, and 10% CBSR composite specimens using Equation 3.8.

<b>Resistance Model Parameters</b>	
7.5 w.t.% CB Specimen	
Parameter	$\mu$
$b_0$	$2154 \pm 52$
$b_1$	$81.1 \pm 5.4$
$b_2$	$56.4 \pm 3.7$
$b_3$	$42.2 \pm 3.4$
$\tau_{R1}$	$181.1 \pm 33.6$
$\tau_{R2}$	$22.8 \pm 3.8$
$\tau_{R3}$	$3.5 \pm 0.6$
10 w.t.% CB Specimen	
Parameter	$\mu$
$b_0$	$1650 \pm 97$
$b_1$	$55.2 \pm 8.9$
$b_2$	$77.4 \pm 12.2$
$b_3$	$38.4 \pm 9.5$
$\tau_{R1}$	$169.6 \pm 61.7$
$\tau_{R2}$	$21.9 \pm 9.7$
$\tau_{R3}$	$3.0 \pm 1.6$

### 3.3.6 Resistance-Stress Relationship

To display the non-linear relationship between the stress and calculated resistance within the material they are plotted against each other over 30 sequential relaxation periods of 300s. The non-linear relationship between stress and resistance changes over time for each relaxation as shown in Figure 3.18, where the data for the first relaxation is displayed in green and the last relaxation in blue.

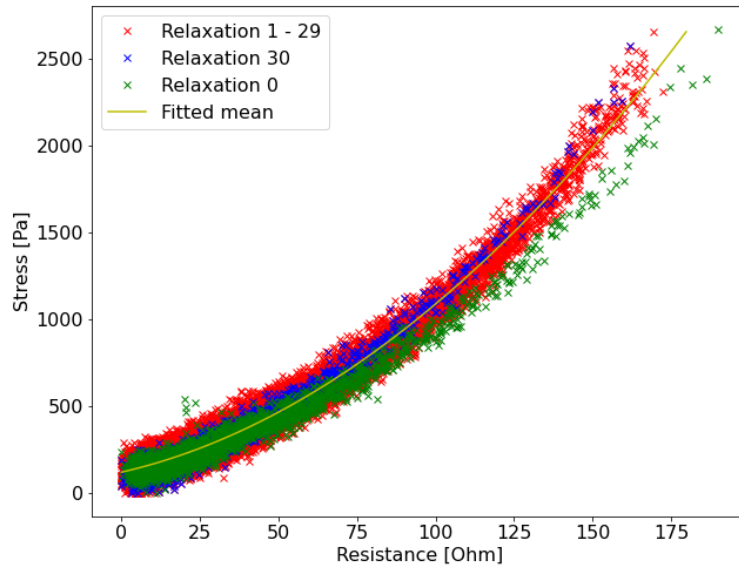


FIGURE 3.18: Comparing resistance and stress relaxation data against each other occurring during 30 pulses of a 10% strain step input for a 7.5 w.t.% CBSR composite

The stress-resistive relaxation data was fitted to a generic second order polynomial of the form,

$$\sigma(R) = aR^2 + bR + c \quad (3.9)$$

where  $\sigma$  is stress,  $R$  is the calculated resistance. When fit to the latter 15 cycles of a 30 cycle 10% strain pulse train of stress relaxation data we get the constant values for  $a$ ,  $b$  and  $c$ .

TABLE 3.5: Fitted constants and their mean,  $\mu$ , standard deviation,  $\sigma$ , and coefficient of variation,  $CV$ , values for 7.5%, and 10% CBSR composite specimens using Equation 3.9

7.5 w.t.% CB Specimen		
Parameter	$\mu$	
$a$	0.055	0.006
$b$	4.15	1.06
$c$	121.8	16.3
10 w.t.% CB Specimen		
Parameter	$\mu$	
$a$	0.098	0.007
$b$	6.37	0.76
$c$	155.8	38.8

### 3.4 Discussion

This work has successfully uncovered several mathematical relationships between stress, strain, and resistance. The repeatability has also been display graphically and calculating the variance

of the fitted models given. This section analyses the results given in the previous sections and highlights limitations of the experiments given.

### 3.4.1 Fabrication

In this work, mixing has been performed using a planetary mixer. It has been shown in other works [52, 183] that other mixing methods, such as using a sonication bath and the addition of solvents, can yield better particle dispersion. A higher degree of CB particle dispersion has also been shown to alter the viscoelastic creep properties [183], and is therefore likely to affect the time constant of resistance.

Composite imaging and experimentation showed the existence of a thin insulative film on the composite surface inhibiting the use surface electrodes to give a good electrical connection to the percolated CB network. The imaging also showed the existence of voids in the micron scale which contribute towards the material viscoelasticity. The optimisation of particle dispersion and investigation into the effects of void dispersion and sizing could give insight into maximising the material gauge factor.

When characterising the reference pure SR material, the elastic modulus was larger than the 186.2 kPa elastic modulus specified by the manufacturer, likely due to the heat assisted curing process used [178].

### 3.4.2 Quasi-static Tensile Resistance-Strain

The quasi-static linear model given show promise for using the composite CBSR material for applications requiring a low frequency response sensor. This also gives a good steady-state part of a more complex model which includes the non-linear and time-dependent dynamics.

### 3.4.3 Dynamic Resistance-Strain-Rate Response

Increasing strain-rates were shown to increase the offsets in resistance over a range of strains as shown in Figure 3.13. Showing the existence of a repeatable relationship between strain-rate and resistance, for constant strain rates. For strain acceleration different phenomena arose, such as the shoulder phenomena.

### 3.4.4 Falling Edge Strain-Rate-Resistance

A 'falling edge' resistance shoulder phenomena was observed and is clearly seen in Figures 3.12 and 3.14. This is a result of a change in strain rate. The amplitude of this peak was shown to increase with an increasing change in strain-rate from a steady state strain. The shoulder phenomena may exist on the rising edge of the strain adding to the resistive relaxation response however this was not easily distinguishable. In previous literature, the effects of the strain-rate and sudden change in strain-rate on apparent resistance of the CBSR material has not been modelled or shown. Another characteristic of the falling edge shoulder phenomena is the apparent positive correlation between the strain magnitude prior to the falling edge and the amplitude of the shoulder phenomena, as shown below in Appendix B. Another characteristic of note is that the shoulder phenomena is almost not present on a falling edge that goes from a tensile (positive) strain to a small compressive (negative) strain which is also shown in Figure B.1.

### 3.4.5 Resistive Relaxation Fitting

The generalised Maxwell model has been applied to predict the stress relaxation of the CBSR composite and analogously the resistive relaxation seen for a positive strain step input. The data gathered show that the stress relaxation time constant values decrease with an increasing CB percentage, indicating that all constants in Equations 3.8 and 3.7 are also functions of CB percentage. The repeatability of this stress relaxation for strain step inputs shows promise to use of this material in controlled environments, such as factory production lines, where there are known periodic strain step inputs. An application for the resistive relaxation decay time characterisation could be for timer with a soft robotic system.

One aim of this work was to prove the hypothesis that the stress relaxation time constant is different to that of the observed resistive relaxation and able to be modelled mathematically. The apparent difference in time constants and the fitting of the data to two different equations show that the stress relaxation is not linearly related to the resistive relaxation shown clearly in Figure 3.17.

### 3.4.6 Resistance-Stress Relationship

A common hypothesis for the resistive relaxation phenomena is that it may be correlated to the resistive relaxation. This work found that the relationship between the two variables, resistance and stress, during relaxation events was non-linear and time-dependent. This non-linearity was found to have a good fit to a second order polynomial as shown in Figure 3.18. The Mullin's effect was evident in the results and a time-dependence where the concavity of the polynomial fitted increased after the first strain pulse.

### 3.4.7 Viscoelasticity

The hysteresis loop seen in the 10 w.t.% CB sample has a larger hysteresis loop showing that there is increased viscous/damping compared with the other two specimens percentages of CB. The pure SR specimen had no discernible hysteresis from the data as shown in Figure 3.9. The difference in hysteresis and hence viscoelastic properties, across the specimens leads to different stress relaxation properties across the three different percentages of CB composite materials in this work.

### 3.4.8 Repeatability

The resistive relaxation model must be predictable over many strain cycles for use within high-stretch strain sensor applications. If the resistive relaxation changes over time this needs to be modelled. Each test sequence showed that there was a downward trend in the calculated magnitude of resistance for each pulse over time.

The physical phenomena driving this downward trend in resistance magnitude was theorised to have two possible causes. The first cause being; the accumulation of charge within material over time generated by current source, due to the CBSR material having an RC-network-like behaviour. The second potential cause being; the gradual alignment of the CB particle network due to the electrostatic attraction of CB chains. This could be tested by increasing the current used and observing the gradient of the downward trend.

The charging theory was mitigated by using an alternating polarity measurement technique. The reversible current source was switched at 10 Hz dampeden this downward trend, however the downward trend in resistance was still observed as shown in Figure 3.19. An example of an experiment with the previous non-switched DC current is shown in Appendix Figures B.2 and B.3 for comparison.

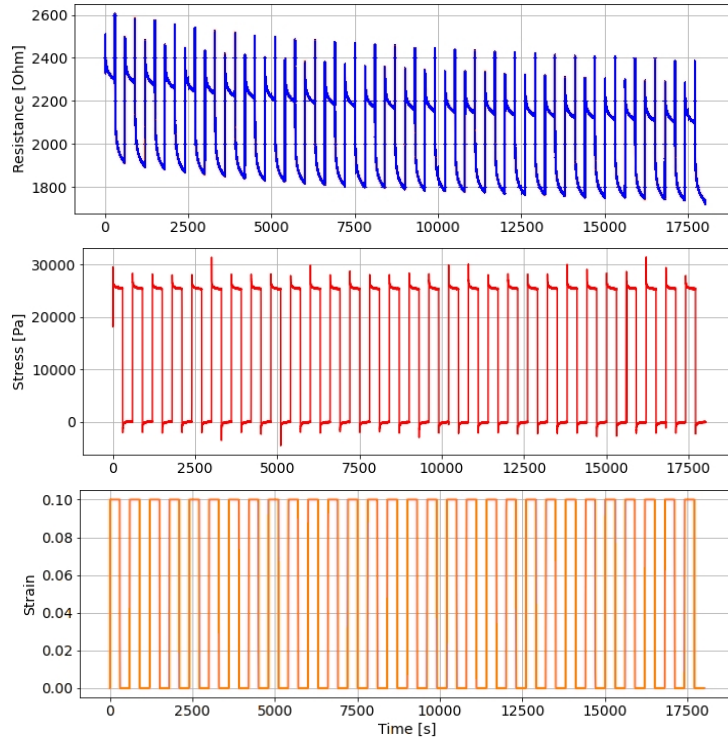


FIGURE 3.19: A typical test sequence of a 30 pulse strain train recording the calculated resistance and stress of a 7.5 w.t.% CBSR composite

### 3.4.9 Further Discussion and Future Work

It must be noted that for fitting the resistive relaxation, stress-resistive relaxation and the falling edge phenomena the data was translated in the xy axes for for ease of the regression algorithm fitting.

A sufficiently high current source value was required to ensure a SNR that would not hinder data analysis. There seemed to be a wetting current threshold where the SNR dropped as shown by the 20  $\mu$ A resistance pulse response in Figure 3.20.

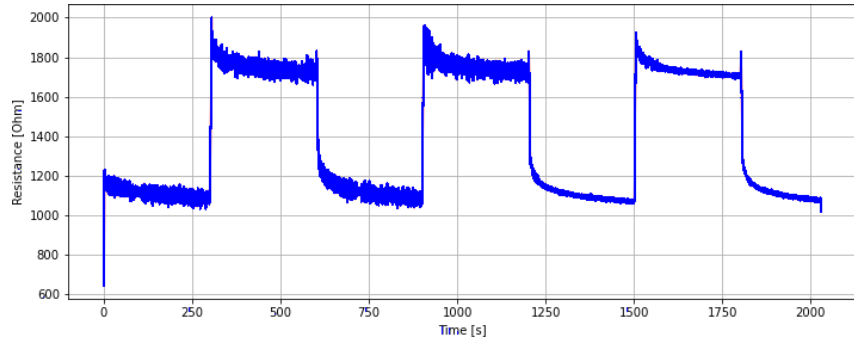


FIGURE 3.20: Three identical 15% strain pulses at three different current values ,in order,  $10\mu\text{A}$ ,  $15\mu\text{A}$ , and  $20\mu\text{A}$ .

A limitation of using this material as a strain sensor is the non-linearity of the material above a certain strain value, at which the composite's resistivity diverges towards a highly insulative value within the giga-ohms range. This non-linear behaviour of CBSR can be used as a mechanically activated switching device [158]. If modelled, this non-linearity could extend the range of strains that can be measured.

The consideration of temperature and strain history [14] could be used in further research to characterise a CBSR-based strain sensor for a range of application environments.

Future work includes creating a model that incorporates all of the behaviours shown in this work so that an accurate inverse model can be created to use the material as a strain sensor. To capture all of these phenomena models that can capture and recreate time-dependent phenomena such as recurrent neural networks (RNNs) could be used.

### 3.5 Conclusions

The CBSR material used in this work provided exaggerated non-linear effects compared to literature where these non-ideal phenomena are often quashed and ignored. The relationships discussed in this work could be used to define a CBSR-based strain sensor models and show the expected behaviours in the composite material for different strain application scenarios.

In order to improve the accuracy of dynamic strain measurements with CBSR composites a stress and analogous resistive relaxation model was formed. The generalised Maxwell model, Equation 3.7 was used to fit to the stress relaxation data for three specimen with CB weight percentages of 0, 7.5% and 10%. The variation in the fitted stress relaxation parameters was higher than the resistive relaxation parameters. All of the stress relaxation model parameters increased with increasing weight percentage of CB, indicating an increase in viscoelasticity. The resistive relaxation time constant and offset parameters both decreased with increasing CB wt%. However the change in these parameters is not large and more experimentation with various CB weight percentages would be required to create a model of how the relaxation changes with CB wt%. The standard deviation of parameters increased with increasing CB wt%.

With the models developed we have shown that the apparent resistive relaxation can be modelled, which will enable more accurate estimation of dynamic strain when these materials are applied as sensors.

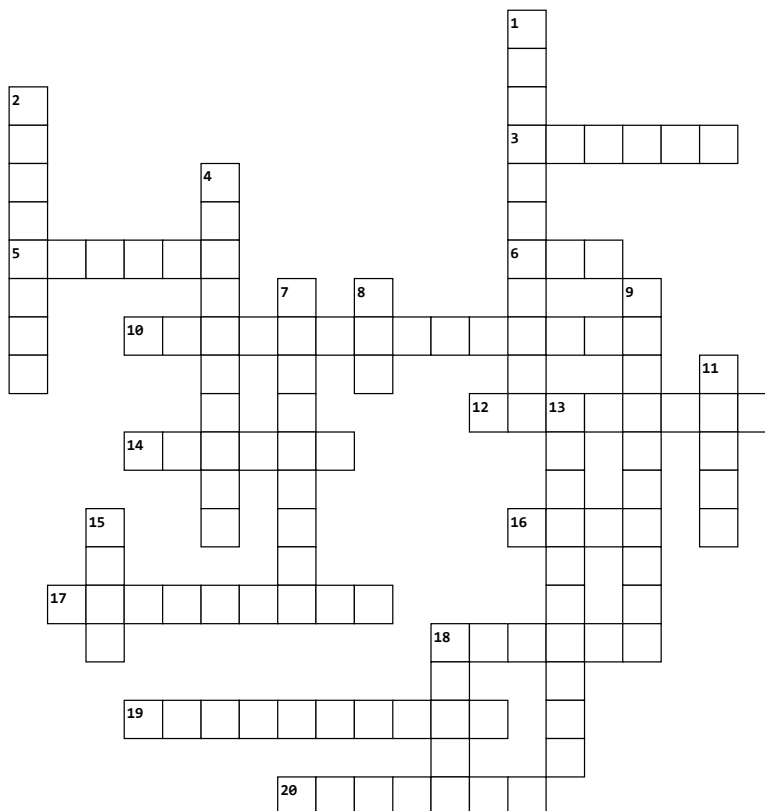
Many repeatable behaviours of the CBSR material have been found in this chapter which have not been elucidated in previous literature. Mathematical relationships between parameters

stress, strain, and resistance have been developed. These mathematical relationships may be related to physical phenomena occurring within the viscoelastic material, however this work has not found a generalised model that can be inverted to accurately obtain a stress or strain given a resistance input. Future work will look into non-linear modelling of the material by using various methods. One method of interest being recurrent neural networks (RNNs), due to its ability to model time-dependent data.

# Appendix A

## Thesis Crossword

### Tired of Marking? CROSSWORD



#### Across

- 3. Motivating emotion of a PhD student
- 5. This thesis is provided almost free of ...
- 6. Time constant symbol
- 10. Touch and change it's electrical properties
- 12. Motor-like
- 14. Soot
- 16. Texture
- 17. Curvy. Difficult to solve.
- 18. Epsilon is for permittivity and ...
- 19. You often ... while wearing a lab coat
- 20. Scottish Physicist who loves waves.

#### Down

- 1. Linearised model that mitigates time
- 2. A great elastomer
- 4. Meat of a capacitor sandwich
- 7. Mixed material
- 8. Want to solve a mesh? Use ...
- 9. Viscoelastic phenomena and massage type
- 11. A long book
- 13. Image slice
- 15. A couch potato would ... out
- 18. Some people have a sixth one

## Appendix B

# Strain-Stress-Resistance Experiments

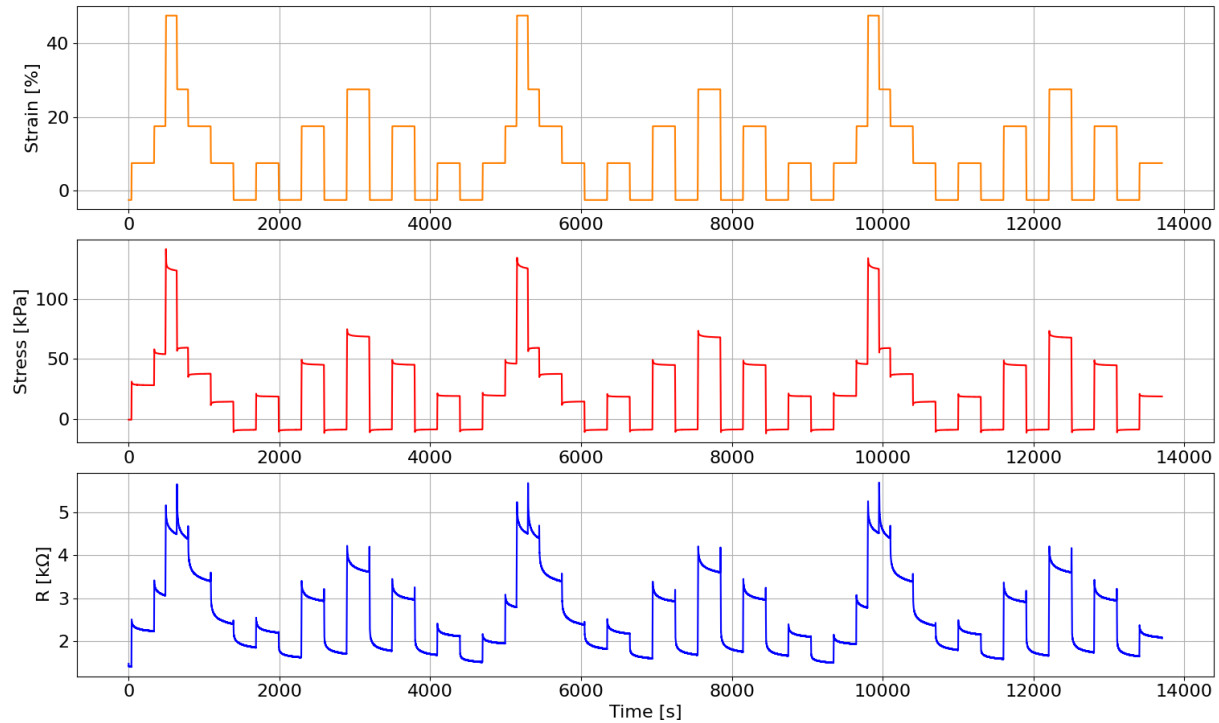


FIGURE B.1: Strain test sequence showing the shoulder phenomena correlation for varying magnitudes of strain for a 7.5 wt% CBSR specimen dogbone sample. This experiment had an unintentional offset of 1 mm, however this showed a drastic decrease shoulder phenomena when the falling edge is crossing the x-axis.

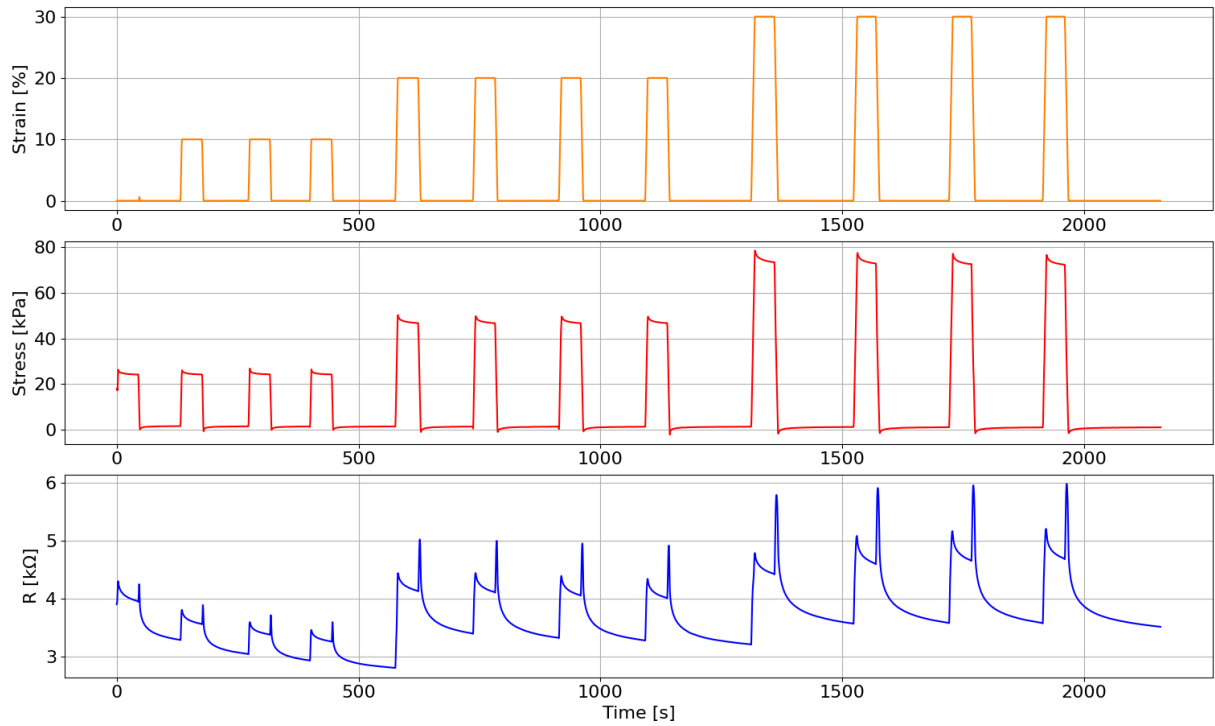


FIGURE B.2: Strain test sequence showing the shoulder phenomena correlation for varying magnitudes of strain for a 7.5 wt% CBSR specimen dogbone sample. This experiment used DC measurements, so the macro downward trend in resistance is more obvious than other experimental data given in this work with used a switched AC signal.

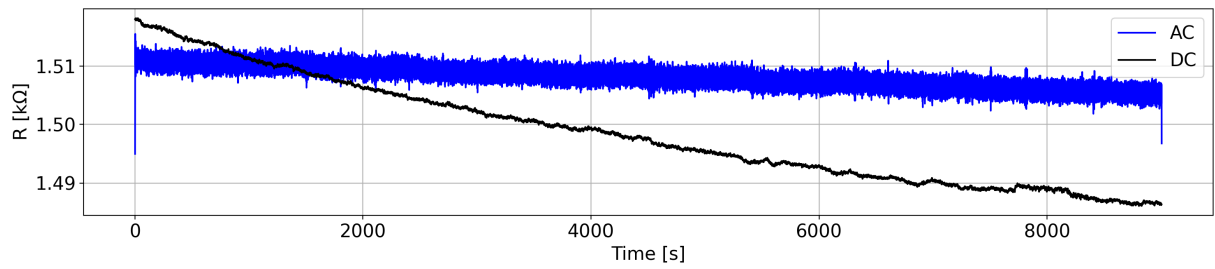


FIGURE B.3: AC vs DC downward trend in resistance for an unstrained 7.5 wt% CBSR composite dogbone specimen.

## **Appendix C**

### **Chapter Title**

# Bibliography

- [1] Meejin Kim and Sukwon Lee. Fusion poser: 3d human pose estimation using sparse imus and head trackers in real time. *Sensors*, 22:4846, 6 2022. ISSN 1424-8220. doi: 10.3390/S22134846. URL <https://www.mdpi.com/1424-8220/22/13/4846>.
- [2] Ryo Eguchi, Brendan Michael, Matthew Howard, and Masaki Takahashi. Shift-adaptive estimation of joint angle using instrumented brace with two stretch sensors based on gaussian mixture models. *IEEE Robotics and Automation Letters*, 5:5881–5888, 10 2020. ISSN 23773766. doi: 10.1109/LRA.2020.3010486.
- [3] Logan Thomas Chatfield. A hybrid assist-as-needed elbow exoskeleton for stroke rehabilitation. 2021. doi: 10.26021/11321. URL <https://hdl.handle.net/10092/102273>.
- [4] Ben O'Brien, Todd Gisby, and Iain A. Anderson. Stretch sensors for human body motion. volume 9056, pages 254–262. SPIE, 3 2014. ISBN 9780819499820. doi: 10.1117/12.2046143. URL <https://www.spiedigitallibrary.org/conference-proceedings-of-spie/9056/905618/Stretch-sensors-for-human-body-motion/10.1117/12.2046143.full>.
- [5] XSENSOR. Xsensor — wheelchair seating. URL <https://www.xsensor.com/solutions-and-platform/csm/wheelchair-seating>.
- [6] PressureProfile. Tactile sensors for robotic applications — pps, 2023. URL <https://pressureprofile.com/robotics>.
- [7] PowerOn. Poweron: Update of the "super sensitive" - robotik-insider.de. URL <https://mrk-blog.de/en/PowerON-Update-of-the-super-sensitive/>.
- [8] Tekscan. Thin-film pressure sensors — tekscan. URL [https://www.tekscan.com/thin-film-pressure-sensors?utm\\_source=google&utm\\_medium=cpc&utm\\_term=pressure+sensors&utm\\_content=eta7&utm\\_campaign=pressure&gad\\_source=1&gclid=CjwKCAiApuCrBhAuEiwA8VJ6Jt-4kVuEinAM6-jd72DwnWxvPCQus\\_Md7xr2i\\_bD0sIWg7SK7aw6nRoCuk0QAvD\\_BwE](https://www.tekscan.com/thin-film-pressure-sensors?utm_source=google&utm_medium=cpc&utm_term=pressure+sensors&utm_content=eta7&utm_campaign=pressure&gad_source=1&gclid=CjwKCAiApuCrBhAuEiwA8VJ6Jt-4kVuEinAM6-jd72DwnWxvPCQus_Md7xr2i_bD0sIWg7SK7aw6nRoCuk0QAvD_BwE).
- [9] SensorProducts. Tactilus — compression force sensing resistor (fsr) — force sensing resistors — force sensing resistors — tactilus — surface pressure indicator — mapping — force sensing and profiling. URL <https://www.sensorprod.com/tactilus.php>.
- [10] Joseph Teran, Silvia Blemker, Victor Ng-Thow-Hing, and R. Fedkiw. Finite volume methods for the simulation of skeletal muscle. pages 68–74, June 2003.
- [11] Wang Yanjie and Takushi Sugino. Ionic polymer actuators: Principle, fabrication and applications. July 2018.

- [12] Nicholas Kellaris, Vidyacharan Gopaluni Venkata, Garrett M. Smith, Shane K. Mitchell, and Christoph Keplinger. Peano-hasel actuators: Muscle-mimetic, electrohydraulic transducers that linearly contract on activation. *Science Robotics*, 3(14):3276, 1 2018. ISSN 24709476. doi: 10.1126/scirobotics.aar3276. URL <http://robotics.sciencemag.org/jbr/i>.
- [13] Yu-Jin Park, Seong Hwan Kim, Tae-Hoon Lee, Ae-Ri Cha, Gi-Woo Kim, and Seung-Bok Choi. Design analysis of a magnetorheological elastomer based bush mechanism. volume 10595, March 2018. URL <https://doi.org/10.1117/12.2318795>.
- [14] Y.C. Fung. *Biomechanics - Mechanical Properties of Living Tissues*. Springer Verlag, second edition, 1993. ISBN 0-387-97947-6. Pg 568.
- [15] Yann Roudaut, Aurélie Lonigro, Bertrand Coste, Jizhe Hao, Patrick Delmas, and Marcel Crest. Touch sense: functional organization and molecular determinants of mechanosensitive receptors. *Channels (Austin, Tex.)*, 6:234–245, 7 2012. ISSN 1933-6950. doi: 10.4161/CHAN.22213. URL <https://www.ncbi.nlm.nih.gov/pmc/articles/pmid/23146937/?tool=EBIhttps://europepmc.org/article/pmc/3508902>.
- [16] Francesco Stella and Josie Hughes. The science of soft robot design: A review of motivations, methods and enabling technologies. *Frontiers in Robotics and AI*, 9:1059026, 1 2023. ISSN 22969144. doi: 10.3389/FROBT.2022.1059026/BIBTEX.
- [17] Yongchang Zhang, Pengchun Li, Jiale Quan, Longqiu Li, Guangyu Zhang, and Dekai Zhou. Progress, challenges, and prospects of soft robotics for space applications. *Advanced Intelligent Systems*, 5:2200071, 3 2023. ISSN 2640-4567. doi: 10.1002/AISY.202200071. URL <https://onlinelibrary.wiley.com/doi/full/10.1002/aisy.202200071https://onlinelibrary.wiley.com/doi/abs/10.1002/aisy.202200071https://onlinelibrary.wiley.com/doi/10.1002/aisy.202200071>.
- [18] Florian Hartmann, Melanie Baumgartner, Martin Kaltenbrunner, F Hartmann, M Baumgartner, and M Kaltenbrunner. Becoming sustainable, the new frontier in soft robotics. *Advanced Materials*, 33:2004413, 5 2021. ISSN 1521-4095. doi: 10.1002/ADMA.202004413. URL <https://onlinelibrary.wiley.com/doi/full/10.1002/adma.202004413https://onlinelibrary.wiley.com/doi/abs/10.1002/adma.202004413https://onlinelibrary.wiley.com/doi/10.1002/adma.202004413>.
- [19] Oncay Yasa, Yasunori Toshimitsu, Mike Y. Michelis, Lewis S. Jones, Miriam Filippi, Thomas Buchner, and Robert K. Katzschmann. An overview of soft robotics. *Annual Review of Control, Robotics, and Autonomous Systems*, 6:1–29, 5 2023. ISSN 25735144. doi: 10.1146/ANNUREV-CONTROL-062322-100607/CITE/REFWORKS. URL <https://www.annualreviews.org/content/journals/10.1146/annurev-control-062322-100607>.
- [20] Mariangela Manti, Vito Cacucciolo, and Matteo Cianchetti. Stiffening in soft robotics: A review of the state of the art. *IEEE Robotics and Automation Magazine*, 23:93–106, 9 2016. ISSN 10709932. doi: 10.1109/MRA.2016.2582718.
- [21] Chidanand Hegde, Jiangtao Su, Joel Ming Rui Tan, Ke He, Xiaodong Chen, and Shlomo Magdassi. Sensing in soft robotics. *ACS Nano*, 17:15277–15307, 8 2023. ISSN 1936086X. doi: 10.1021/ACSNANO.3C04089/ASSET/IMAGES/LARGE/NN3C04089\_0013.JPG. URL <https://pubs.acs.org/doi/full/10.1021/acsnano.3c04089>.
- [22] Cosimo Della-Santina, Christian Duriez, and Daniela Rus. Model-based control of soft robots: A survey of the state of the art and open challenges. *IEEE Control Systems*, 43:30–65, 6 2023. ISSN 1941000X. doi: 10.1109/MCS.2023.3253419.

- [23] Costanza Armanini, Frederic Boyer, Anup Teejo Mathew, Christian Duriez, and Federico Renda. Soft robots modeling: A structured overview. *IEEE Transactions on Robotics*, 6 2023. ISSN 19410468. doi: 10.1109/TRO.2022.3231360.
- [24] S. Murugesan. An overview of electric motors for space applications. *IEEE Transactions on Industrial Electronics and Control Instrumentation*, IECI-28:260–265, 1981. ISSN 00189421. doi: 10.1109/TIECI.1981.351050.
- [25] T. Ashuri, A. Armani, R. Jalilzadeh Hamidi, T. Reasnor, S. Ahmadi, and K. Iqbal. Biomedical soft robots: current status and perspective. *Biomedical engineering letters*, 10:369–385, 8 2020. ISSN 2093-985X. doi: 10.1007/S13534-020-00157-6. URL <https://pubmed.ncbi.nlm.nih.gov/32864173/>.
- [26] F. Branz and A. Francesconi. Experimental evaluation of a dielectric elastomer robotic arm for space applications. *Acta Astronautica*, 133:324–333, 4 2017. ISSN 0094-5765. doi: 10.1016/J.ACTAASTRO.2016.11.007.
- [27] Alessandro Bruschi, Davide Maria Donati, Peter Choong, Enrico Lucarelli, and Gordon Wallace. Dielectric elastomer actuators, neuromuscular interfaces, and foreign body response in artificial neuromuscular prostheses: A review of the literature for an in vivo application. *Advanced Healthcare Materials*, 10:2100041, 7 2021. ISSN 2192-2659. doi: 10.1002/ADHM.202100041. URL <https://onlinelibrary.wiley.com/doi/full/10.1002/adhm.202100041>  
<https://onlinelibrary.wiley.com/doi/abs/10.1002/adhm.202100041>  
<https://onlinelibrary.wiley.com/doi/10.1002/adhm.202100041>.
- [28] Todd A. Gisby, Benjamin M. Obrien, and Iain A. Anderson. Self sensing feedback for dielectric elastomer actuators. *Applied Physics Letters*, 102, 5 2013. ISSN 00036951. doi: 10.1063/1.4805352/26744. URL [/aip/apl/article/102/19/193703/26744/Self-sensing-feedback-for-dielectric-elastomer](https://aip.org/article/102/19/193703/26744/Self-sensing-feedback-for-dielectric-elastomer).
- [29] Samuel Rosset, Benjamin M. O'Brien, Todd Gisby, Daniel Xu, Herbert R. Shea, and Iain A. Anderson. Self-sensing dielectric elastomer actuators in closed-loop operation. *Smart Materials and Structures*, 22:104018, 9 2013. ISSN 0964-1726. doi: 10.1088/0964-1726/22/10/104018. URL <https://iopscience.iop.org/article/10.1088/0964-1726/22/10/104018>  
<https://iopscience.iop.org/article/10.1088/0964-1726/22/10/104018/meta>.
- [30] Xiqiang Liu, Li Wang, Guidong Chen, al, Joseph W Lowdon, Kasper Eersels, Bart van Grinsven, G Rizzello, D Naso, A York, and S Seelecke. Closed loop control of dielectric elastomer actuators based on self-sensing displacement feedback. *Smart Materials and Structures*, 25:035034, 2 2016. ISSN 0964-1726. doi: 10.1088/0964-1726/25/3/035034. URL <https://iopscience.iop.org/article/10.1088/0964-1726/25/3/035034>  
<https://iopscience.iop.org/article/10.1088/0964-1726/25/3/035034/meta>.
- [31] Weiyang Huang, Guozheng Kang, and Pengyu Ma. Uniaxial electro-mechanically coupled cyclic deformation of vhb 4905 dielectric elastomer: Experiment and constitutive model. *Journal of Materials Engineering and Performance*, pages 1–16, 4 2023. ISSN 15441024. doi: 10.1007/S11665-023-08179-8/FIGURES/17. URL <https://link.springer.com/article/10.1007/s11665-023-08179-8>.
- [32] Wan Hasbullah MohdIsa, Andres Hunt, and S. Hassan HosseinNia. Sensing and self-sensing actuation methods for ionic polymer–metal composite (ipmc): A review. *Sensors* 2019, Vol. 19, Page 3967, 19:3967, 9 2019. ISSN 1424-8220. doi: 10.3390/

- S19183967. URL <https://www.mdpi.com/1424-8220/19/18/3967/htm> <https://www.mdpi.com/1424-8220/19/18/3967>.
- [33] John A. McGrath and Jouni Uitto. Anatomy and organization of human skin. *Rook's Textbook of Dermatology: Eighth Edition*, 1:1–53, 5 2010. doi: 10.1002/9781444317633. CH3. URL <https://onlinelibrary.wiley.com/doi/full/10.1002/9781444317633.ch3> <https://onlinelibrary.wiley.com/doi/abs/10.1002/9781444317633.ch3> <https://onlinelibrary.wiley.com/doi/10.1002/9781444317633.ch3>.
- [34] Guillaume Landry, Katia Parodi, Joachim E Wildberger, al, Mikaël Simard, Arthur Lalonde, Hugo Bouchard, Gurpreet Singh, and Arnab Chanda. Mechanical properties of whole-body soft human tissues: a review. *Biomedical Materials*, 16:062004, 10 2021. ISSN 1748-605X. doi: 10.1088/1748-605X/AC2B7A. URL <https://iopscience.iop.org/article/10.1088/1748-605X/ac2b7a> <https://iopscience.iop.org/article/10.1088/1748-605X/ac2b7a/meta>.
- [35] Holger J. Klein, Richard M. Fakin, Pascal Ducommun, Thomas Giesen, Pietro Giovanoli, and Maurizio Calcagni. Evaluation of cutaneous spatial resolution and pressure threshold secondary to digital nerve repair. *Plastic and Reconstructive Surgery*, 137:1203–1212, 2016. ISSN 00321052. doi: 10.1097/PRS.0000000000002023. URL [https://journals.lww.com/plasreconsurg/fulltext/2016/04000/evaluation\\_of\\_cutaneous\\_spatial\\_resolution\\_and.20.aspx](https://journals.lww.com/plasreconsurg/fulltext/2016/04000/evaluation_of_cutaneous_spatial_resolution_and.20.aspx).
- [36] Judith Krotoski, Sidney Weinstein, and Curt Weinstein. Testing sensibility, including touch-pressure, two-point discrimination, point localization, and vibration. *Journal of Hand Therapy*, 6:114–123, 4 1993. ISSN 0894-1130. doi: 10.1016/S0894-1130(12)80292-4.
- [37] Aisling Ní Annaidh, Karine Bruyère, Michel Destrade, Michael D. Gilchrist, and Mélanie Otténo. Characterization of the anisotropic mechanical properties of excised human skin. *Journal of the Mechanical Behavior of Biomedical Materials*, 5:139–148, 1 2012. ISSN 1751-6161. doi: 10.1016/J.JMBBM.2011.08.016.
- [38] Krisakorn Khaothong, J C H Goh, and C T Lim. In vivo measurements of the mechanical properties of human skin and muscle by inverse finite element method combined with the indentation test. *IFMBE Proceedings*, 31 IFMBE:1467–1470, 2010. ISSN 1433-9277. doi: 10.1007/978-3-642-14515-5\_374. URL [https://link.springer.com/chapter/10.1007/978-3-642-14515-5\\_374](https://link.springer.com/chapter/10.1007/978-3-642-14515-5_374).
- [39] Y. Zheng and A. F.T. Mak. Effective elastic properties for lower limb soft tissues from manual indentation experiment. *IEEE Transactions on Rehabilitation Engineering*, 7: 257–267, 9 1999. ISSN 10636528. doi: 10.1109/86.788463.
- [40] Brian Holt, Anubhav Tripathi, and Jeffrey Morgan. Viscoelastic response of human skin to low magnitude physiologically relevant shear. *Journal of biomechanics*, 41:2689, 8 2008. ISSN 00219290. doi: 10.1016/J.JBIOMECH.2008.06.008. URL [/pmc/articles/PMC2584606/](https://pmc/articles/PMC2584606/) [pmc/articles/PMC2584606/?report=abstract](https://pmc/articles/PMC2584606/?report=abstract) <https://www.ncbi.nlm.nih.gov/pmc/articles/PMC2584606/>.
- [41] Cameron H. Parvini, Alexander X. Cartagena-Rivera, and Santiago D. Solares. Viscoelastic parameterization of human skin cells characterize material behavior at multiple timescales. *Communications Biology* 2022 5:1, 5:1–11, 1 2022. ISSN 2399-3642. doi: 10.1038/s42003-021-02959-5. URL <https://www.nature.com/articles/s42003-021-02959-5>.

- [42] Mélanie Ottenio, Doris Tran, Aisling Ní Annaidh, Michael D. Gilchrist, and Karine Bruyère. Strain rate and anisotropy effects on the tensile failure characteristics of human skin. *Journal of the Mechanical Behavior of Biomedical Materials*, 41:241–250, 1 2015. ISSN 1751-6161. doi: 10.1016/J.JMBBM.2014.10.006.
- [43] Karen A. Newell. *Wound Closure*, pages 313–341. W.B. Saunders, 2 edition, 1 2007. ISBN 9781416030010. doi: 10.1016/B978-1-4160-3001-0.50027-7.
- [44] Sharad P. Paul. Biodynamic excisional skin tension lines for surgical excisions: untangling the science. *Annals of The Royal College of Surgeons of England*, 100:330, 4 2018. ISSN 00358843. doi: 10.1308/RCSANN.2018.0038. URL [/pmc/articles/PMC5958865/](https://www.ncbi.nlm.nih.gov/pmc/articles/PMC5958865/)?report=abstract<https://www.ncbi.nlm.nih.gov/pmc/articles/PMC5958865/>.
- [45] Davide Deflorio, Massimiliano Di Luca, and Alan M. Wing. Skin and mechanoreceptor contribution to tactile input for perception: A review of simulation models. *Frontiers in Human Neuroscience*, 16:862344, 6 2022. ISSN 16625161. doi: 10.3389/FNHUM.2022.862344/BIBTEX.
- [46] Hirotake Yokota, Naofumi Otsuru, Rie Kikuchi, Rinako Suzuki, Sho Kojima, Kei Saito, Shota Miyaguchi, Yasuto Inukai, and Hideaki Onishi. Establishment of optimal two-point discrimination test method and consideration of reproducibility. *Neuroscience Letters*, 714:134525, 1 2020. ISSN 0304-3940. doi: 10.1016/J.NEULET.2019.134525.
- [47] Rochelle Ackerley, Ida Carlsson, Henric Wester, Håkan Olausson, and Helena Backlund Wasling. Touch perceptions across skin sites: differences between sensitivity, direction discrimination and pleasantness. *Frontiers in Behavioral Neuroscience*, 8, 2 2014. ISSN 16625153. doi: 10.3389/FNBEH.2014.00054. URL [/pmc/articles/PMC3928539/](https://www.ncbi.nlm.nih.gov/pmc/articles/PMC3928539/)?report=abstract<https://www.ncbi.nlm.nih.gov/pmc/articles/PMC3928539/>.
- [48] Nicholas D.J. Strzalkowski, Robyn L. Mildren, and Leah R. Bent. Neurophysiology of tactile perception: A tribute to steven hsiao: Thresholds of cutaneous afferents related to perceptual threshold across the human foot sole. *Journal of Neurophysiology*, 114:2144, 8 2015. ISSN 15221598. doi: 10.1152/JN.00524.2015. URL <https://www.ncbi.nlm.nih.gov/pmc/articles/PMC4595609/>.
- [49] Mohsin I. Tiwana, Stephen J. Redmond, and Nigel H. Lovell. A review of tactile sensing technologies with applications in biomedical engineering. *Sensors and Actuators A: Physical*, 179:17–31, 6 2012. ISSN 0924-4247. doi: 10.1016/J.SNA.2012.02.051.
- [50] Lei Sun, Shuwen Jiang, Yao Xiao, and Wanli Zhang. Realization of flexible pressure sensor based on conductive polymer composite via using electrical impedance tomography. *Smart Materials and Structures*, 29:055004, 3 2020. ISSN 0964-1726. doi: 10.1088/1361-665X/AB75A3. URL <https://iopscience-iop-org.ezproxy.canterbury.ac.nz/article/10.1088/1361-665X/ab75a3><https://iopscience-iop-org.ezproxy.canterbury.ac.nz/article/10.1088/1361-665X/ab75a3/meta>.
- [51] Yun Lu, Weina He, Tai Cao, Haitao Guo, Yongyi Zhang, Qingwen Li, Ziqiang Shao, Yulin Cui, and Xuetong Zhang. Elastic, conductive, polymeric hydrogels and sponges. *Scientific Reports* 2014 4:1, 4:1–8, 7 2014. ISSN 2045-2322. doi: 10.1038/srep05792. URL <https://www.nature.com/articles/srep05792>.
- [52] Michael E. Spahr, Raffaele Gilardi, and Daniele Bonacchi. *Carbon Black for Electrically Conductive Polymer Applications*, pages 375–400. Springer, Cham, 2017. doi: 10.

- 1007/978-3-319-28117-9\_32. URL [https://link.springer.com/referenceworkentry/10.1007/978-3-319-28117-9\\_32](https://link.springer.com/referenceworkentry/10.1007/978-3-319-28117-9_32).
- [53] Patricia Hazelton, Mengguang Ye, and Xianfeng Chen. *Introduction to Conducting Polymers*. 2023. doi: 10.1021/bk-2023-1438.ch001. URL <https://pubs.acs.org/sharingguidelines>.
- [54] Yong Lae Park, Carmel Majidi, Rebecca Kramer, Phillip Brard, and Robert J. Wood. Hyperelastic pressure sensing with a liquid-embedded elastomer. *Journal of Micromechanics and Microengineering*, 20:125029, 11 2010. ISSN 0960-1317. doi: 10.1088/0960-1317/20/12/125029. URL <https://iopscience.iop.org/article/10.1088/0960-1317/20/12/125029> <https://iopscience.iop.org/article/10.1088/0960-1317/20/12/125029/meta>.
- [55] Taekeon Jung and Sung Yang. Highly stable liquid metal-based pressure sensor integrated with a microfluidic channel. *Sensors* 2015, Vol. 15, Pages 11823–11835, 15:11823–11835, 5 2015. ISSN 1424-8220. doi: 10.3390/S150511823. URL <https://www.mdpi.com/1424-8220/15/5/11823>.
- [56] Daehan Kim, Sung Hwan Kim, and Joong Yull Park. Floating-on-water fabrication method for thin polydimethylsiloxane membranes. *Polymers*, 11:1264, 8 2019. ISSN 20734360. doi: 10.3390/polym11081264. URL [/pmc/articles/PMC6722912/?report=abstract](https://pmc/articles/PMC6722912/?report=abstract) <https://www.ncbi.nlm.nih.gov/pmc/articles/PMC6722912/>.
- [57] Hyunwoo Yuk, Teng Zhang, German Alberto Parada, Xinyue Liu, and Xuanhe Zhao. Skin-inspired hydrogel-elastomer hybrids with robust interfaces and functional microstructures. *Nature communications*, 7:12028, 6 2016.
- [58] K. Park, H. Yuk, M. Yang, J. Cho, H. Lee, and J. Kim. A biomimetic elastomeric robot skin using electrical impedance and acoustic tomography for tactile sensing. *Science Robotics*, 7:7187, 6 2022. ISSN 24709476. doi: 10.1126/SCIROBOTICS.ABM7187/ SUPPL\_FILE/SCIROBOTICS.ABM7187\_MOVIES\_S1\_TO\_S4.ZIP. URL <https://www.science.org/doi/10.1126/scirobotics.abm7187>.
- [59] Haofeng Chen, Xuanxuan Yang, Jialu Geng, Gang Ma, and Xiaojie Wang. A skin-like hydrogel for distributed force sensing using an electrical impedance tomography-based pseudo-array method. *ACS Applied Electronic Materials*, 3 2023. ISSN 2637-6113. doi: 10.1021/ACSAELM.2C01394. URL <https://pubs.acs.org/doi/abs/10.1021/acsaelm.2c01394>.
- [60] Shuoyan Xu, Zigan Xu, Ding Li, Tianrui Cui, Xin Li, Yi Yang, Houfang Liu, and Tianling Ren. Recent advances in flexible piezoresistive arrays: Materials, design, and applications. *Polymers* 2023, Vol. 15, Page 2699, 15:2699, 6 2023. ISSN 2073-4360. doi: 10.3390/POLYM15122699. URL <https://www.mdpi.com/2073-4360/15/12/2699> <https://www.mdpi.com/2073-4360/15/12/2699>.
- [61] Kyoseung Sim, Zhouyu Rao, Zhanan Zou, Faheem Ershad, Jianming Lei, Anish Thukral, Jie Chen, Qing An Huang, Jianliang Xiao, and Cunjiang Yu. Metal oxide semiconductor nanomembrane-based soft unnoticeable multifunctional electronics for wearable human-machine interfaces. *Science advances*, 5, 8 2019. ISSN 2375-2548. doi: 10.1126/SCIADV. AAV9653. URL <https://pubmed.ncbi.nlm.nih.gov/31414044/>.
- [62] Yuting Zhu, Kean Aw, and Tim Giffney. Dielectric elastomer-based multi-location capacitive sensor. pages 84–95, 12 2021. URL <https://researchspace.auckland.ac.nz/handle/2292/60603>.

- [63] Guanhao Liang, Yancheng Wang, Deqing Mei, Kailun Xi, and Zichen Chen. Flexible capacitive tactile sensor array with truncated pyramids as dielectric layer for three-axis force measurement. *Journal of Microelectromechanical Systems*, 24:1510–1519, 10 2015. ISSN 10577157. doi: 10.1109/JMEMS.2015.2418095.
- [64] Youcan Yan, Zhe Hu, Zhengbao Yang, Wenzhen Yuan, Chaoyang Song, Jia Pan, and Yajing Shen. Soft magnetic skin for super-resolution tactile sensing with force self-decoupling. *Science Robotics*, 6:8801, 2 2021. ISSN 24709476. doi: 10.1126/SCIROBOTICS.ABC8801/SUPPLFILE/ABC8801\_SM.PDF. URL <https://www.science.org/doi/10.1126/scirobotics.abc8801>.
- [65] Gihun Lee, Hyunjin Kim, and Inkyu Park. A mini review of recent advances in optical pressure sensor. *Journal of Sensor Science and Technology*, 32:22–30, 2023. ISSN pISSN 1225-5475/eISSN 2093-7563. doi: <http://dx.doi.org/10.46670/JSST.2023.32.1.22>.
- [66] Dana Hughes and Nikolaus Correll. Texture recognition and localization in amorphous robotic skin. *Bioinspiration & Biomimetics*, 10:055002, 9 2015. ISSN 1748-3190. doi: 10.1088/1748-3190/10/5/055002. URL <https://iopscience.iop.org/article/10.1088/1748-3190/10/5/055002><https://iopscience.iop.org/article/10.1088/1748-3190/10/5/055002/meta>.
- [67] Golezar Gilanizadehdizaj, Kean C. Aw, Jonathan Stringer, and Debes Bhattacharyya. Facile fabrication of flexible piezo-resistive pressure sensor array using reduced graphene oxide foam and silicone elastomer. *Sensors and Actuators A: Physical*, 340:113549, 6 2022. ISSN 0924-4247. doi: 10.1016/J.SNA.2022.113549.
- [68] Ya Fei Fu, Feng Lian Yi, Jin Rui Liu, Yuan Qing Li, Ze Yu Wang, Gang Yang, Pei Huang, Ning Hu, and Shao Yun Fu. Super soft but strong e-skin based on carbon fiber/carbon black/silicone composite: Truly mimicking tactile sensing and mechanical behavior of human skin. *Composites Science and Technology*, 186:107910, 1 2020. ISSN 0266-3538. doi: 10.1016/J.COMPSCITECH.2019.107910.
- [69] Kun Yang, Xinkai Xia, Fan Zhang, Huanzhou Ma, Shengbo Sang, Qiang Zhang, and Jianlong Ji. Implementation of a sponge-based flexible electronic skin for safe human–robot interaction. *Micromachines*, 13:1344, 8 2022. ISSN 2072666X. doi: 10.3390/MI13081344/S1. URL <https://www.mdpi.com/2072-666X/13/8/1344><https://www.mdpi.com/2072-666X/13/8/1344>.
- [70] Jonathan Rossiter and Toshiharu Mukai. A novel tactile sensor using a matrix of leds operating in both photoemitter and photodetector modes. *Proceedings of IEEE Sensors*, 2005:994–997, 2005. doi: 10.1109/ICSENS.2005.1597869.
- [71] Sho Shimadera, Kei Kitagawa, Koyo Sagehashi, Yoji Miyajima, Tomoaki Niiyama, and Satoshi Sunada. Speckle-based high-resolution multimodal soft sensing. *Scientific Reports* 2022 12:1, 12:1–11, 7 2022. ISSN 2045-2322. doi: 10.1038/s41598-022-17026-0. URL <https://www.nature.com/articles/s41598-022-17026-0>.
- [72] Marc Ramuz, Benjamin C.K. Tee, Jeffrey B.H. Tok, and Zhenan Bao. Transparent, optical, pressure-sensitive artificial skin for large-area stretchable electronics. *Advanced Materials*, 24:3223–3227, 6 2012. ISSN 1521-4095. doi: 10.1002/ADMA.201200523. URL <https://onlinelibrary.wiley.com/doi/full/10.1002/adma.201200523><https://onlinelibrary.wiley.com/doi/abs/10.1002/adma.201200523><https://onlinelibrary.wiley.com/doi/10.1002/adma.201200523>.
- [73] R. D. Keynes, David J. Aidley, and Christopher L.-H Huang. *Nerve and Muscle*. Cambridge University Press, 4 edition, 2011. ISBN 9780511853067.

- [74] Robert A Cross. Myosin mechanical ratchet. *Proc Natl Acad Sci USA*, 103(24):8911, 6 2006. URL <http://www.pnas.org/content/103/24/8911.abstract>.
- [75] R Mcn. Alexander and H C Bennet-Clark. Storage of elastic strain energy in muscle and other tissues. *Nature*, 265(5590):114–117, 1977. URL <https://www.scopus.com/inward/record.uri?eid=2-s2.0-0017338764&doi=10.1038%2F265114a0&partnerID=40&md5=1e1abd16ddee92cca4a7a8e6a33940f9>. Cited By :466;br/;Export Date: 10 May 2020;br/;Cited By :466;br/;Export Date: 10 May 2020.
- [76] Robert Full and Kenneth Meijer. *Metrics of Natural Muscle Function*, chapter Metrics of Natural Muscle Function, pages 73–89. SPIE, 3 2004. doi: 10.1117/3.547465. ch3. URL <http://ebooks.spiedigitallibrary.org/content.aspx?doi=10.1117/3.547465.ch3>.
- [77] Mihai Duduta, Ehsan Hajiesmaili, Huichan Zhao, Robert J. Wood, and David R. Clarke. Realizing the potential of dielectric elastomer artificial muscles. *Proceedings of the National Academy of Sciences of the United States of America*, 116(30679271):2476–2481, February 2019. ISSN 0027-8424. doi: 10.1073/pnas.1815053116. URL <https://www.pnas.org/content/116/7/2476><https://www.ncbi.nlm.nih.gov/pmc/articles/PMC6377461/>. 30679271[pmid];PMC6377461[pmcid];30679271[pmid];PMC6377461[pmcid].
- [78] Nicholas P Smith, Christopher J Barclay, and Denis S Loiselle. The efficiency of muscle contraction. *Progress in Biophysics and Molecular Biology*, 88(1):1–58, 2005. ISSN 0079-6107. URL <http://www.sciencedirect.com/science/article/pii/S0079610703001081>.
- [79] Archibald Vivian Hill. The heat of shortening and the dynamic constants of muscle. *Proceedings of the Royal Society of London. Series B - Biological Sciences*, 126(843):136–195, 1938. doi: 10.1098/rspb.1938.0050. URL <https://royalsocietypublishing.org/doi/pdf/10.1098/rspb.1938.0050>.
- [80] Morufu Olusola Ibitoye, Nur Azah Hamzaid, Nazirah Hasnan, Ahmad Khairi Abdul Wahab, and Glen M. Davis. Strategies for rapid muscle fatigue reduction during fes exercise in individuals with spinal cord injury: A systematic review. *PloS one*, 11:e0149024, 2016.
- [81] Milos R. Popovic and T. Adam Thrasher. *Neuroprostheses*. *Encyclopedia of Biomaterials and Biomedical Engineering*, 2004. doi: DOI:10.1081/E-EBBE120013941. URL <http://toronto-fes.ca/publications/2004Popovic.pdf>.
- [82] Knut Schmidt Nielsen. *Animal Physiology: Adaptation and Environment*. Cambridge University Press, 5 edition, 2002. ISBN 521 57098. URL [https://books.google.co.nz/books?id=hcw2AAAAQBAJ&printsec=frontcover&redir\\_esc=y#v=onepage&q&f=false](https://books.google.co.nz/books?id=hcw2AAAAQBAJ&printsec=frontcover&redir_esc=y#v=onepage&q&f=false).
- [83] Katie L. Meadmore, Timothy A. Exell, Emma Hallewell, Ann Marie Hughes, Chris T. Freeman, Mustafa Kutlu, Valerie Benson, Eric Rogers, and Jane H. Burridge. The application of precisely controlled functional electrical stimulation to the shoulder, elbow and wrist for upper limb stroke rehabilitation: a feasibility study. *Journal of neuroengineering and rehabilitation*, 11, 6 2014. ISSN 1743-0003. doi: 10.1186/1743-0003-11-105. URL <https://pubmed.ncbi.nlm.nih.gov/24981060/>.
- [84] Chris Freeman, Tim Exell, Katie Meadmore, Emma Hallewell, and Ann Marie Hughes. Computational models of upper-limb motion during functional reaching tasks for application in fes-based stroke rehabilitation. *Biomedizinische Technik. Biomedical engineering*,

- 60:179–191, 6 2015. ISSN 1862-278X. doi: 10.1515/BMT-2014-0011. URL <https://pubmed.ncbi.nlm.nih.gov/25355246/>.
- [85] Edmund F. Hodkin, Yuming Lei, Jonathan Humby, Isabel S. Glover, Supriyo Choudhury, Hrishikesh Kumar, Monica A. Perez, Helen Rodgers, and Andrew Jackson. Automated fes for upper limb rehabilitation following stroke and spinal cord injury. *Ieee Transactions on Neural Systems and Rehabilitation Engineering*, 26:1067, 5 2018. ISSN 15344320. doi: 10.1109/TNSRE.2018.2816238. URL [/pmc/articles/PMC6051484/](https://pmc/articles/PMC6051484/)?report=abstract<https://www.ncbi.nlm.nih.gov/pmc/articles/PMC6051484/>.
- [86] Dejan B. Popovic. Advances in functional electrical stimulation (fes). *Journal of Electromyography and Kinesiology*, 24:795–802, 12 2014. ISSN 1050-6411. doi: 10.1016/J.JELEKIN.2014.09.008.
- [87] Guangqiang Ma, Xiaojun Wu, Lijin Chen, Xin Tong, and Weiwei Zhao. Characterization and optimization of elastomeric electrodes for dielectric elastomer artificial muscles. *Materials* 2020, Vol. 13, Page 5542, 13(1908508):5542, 12 2020. ISSN 1996-1944. doi: 10.3390/MA13235542. URL <https://www.mdpi.com/1996-1944/13/23/5542>  
<https://www.mdpi.com/1996-1944/13/23/5542>
- [88] Raphael Neuhaus, Nima Zahiri, Jan Petrs, Yasaman Tahouni, Jörg Siegert, Ivica Kolaric, Hanaa Dahy, and Thomas Bauernhansl. Integrating ionic electroactive polymer actuators and sensors into adaptive building skins – potentials and limitations. *Frontiers in Built Environment*, 6:546334, 7 2020. ISSN 22973362. doi: 10.3389/FBUIL.2020.00095 /BIBTEX. URL [www.frontiersin.org](http://www.frontiersin.org).
- [89] Daniel Segalman, Walter Witkowski, D Adolf, and Mohsen Shahinpoor. Theory and application of electrically controlled polymeric gels. *Smart Materials and Structures*, 1: 95, 1 1999.
- [90] Mohsen Shahinpoor. *Ionic Polymer Metal Composites (IPMCs)*. Smart Materials Series. The Royal Society of Chemistry, 2016. ISBN 978-1-78262-720-3.
- [91] Masahiro Homma and Yoshio Nakano. Development of electro-driven polymer gel/platinum composite membranes. *Kagaku Kogaku Ronbunshu*, 25(6):1010–1014, 1999. ISSN 13499203. doi: 10.1252/kakoronbunshu.25.1010.
- [92] Raymond Liu. In situ electrode formation on a nafion membrane by chemical platinization. *Journal of The Electrochemical Society*, 139(1):15, 1992. ISSN 0013-4651. URL <http://dx.doi.org/10.1149/1.2069162>.
- [93] James D Carrico, Nicklaus W Traeden, Matteo Aureli, and Kam K Leang. Fused filament 3d printing of ionic polymer-metal composites (ipmcs). *Smart Materials and Structures*, 24(12):125021, 11 2015. doi: 10.1088/0964-1726/24/12/125021. URL <https://doi.org/10.1088%2F0964-1726%2F24%2F12%2F125021>.
- [94] Mohsen Shahinpoor and Kwang J. Kim. Ionic polymer-metal composites: Iii. modeling and simulation as biomimetic sensors, actuators, transducers, and artificial muscles. *Smart Materials and Structures*, 13(6):1362–1388, 12 2004. ISSN 09641726. doi: 10.1088/0964-1726/13/6/009. URL <https://www.scopus.com/inward/record.uri?eid=2-s2.0-10444275650&doi=10.1088%2f0964-1726%2f13%2f6%2f009&partnerID=40&md5=87202eb3f7394ab27e1da783d00c7386>.

- [95] Barbar Akle and Donald J. Leo. Electromechanical transduction in multilayer ionic transducers. *Smart Materials and Structures*, 13(5):1081–1089, 10 2004. ISSN 09641726. doi: 10.1088/0964-1726/13/5/014. URL <https://www.scopus.com/inward/record.uri?eid=2-s2.0-5744242938&doi=10.1088%2f0964-1726%2f13%2f5%2f014&partnerID=40&md5=65de150f898f2264f18c2ad0633e2f74>.
- [96] Yan Xu, Gang Zhao, Changshun Ma, and Zhuangzhi Sun. Research on preparation and stacking performance of ipmc. *Journal of Biomimetics, Biomaterials and Biomedical Engineering*, 21(1):45–53, 2014. ISSN 22969845. doi: 10.4028/www.scientific.net/JBBBE.21.45. URL <https://www.scopus.com/inward/record.uri?eid=2-s2.0-84906851147&doi=10.4028%2fwww.scientific.net%2fJBBBE.21.45&partnerID=40&md5=ab1a439c97294fdb8d0bcf59ad4d5edb>.
- [97] Shuxiang Guo, T Fukuda, K Kosuge, F Arai, K Oguro, and M Negoro. Micro catheter system with active guide wire-structure, experimental results and characteristic evaluation of active guide wire catheter using icpf actuator. In *1994 5th International Symposium on Micro Machine and Human Science Proceedings*, page 191, 1994.
- [98] Akio Kodaira, Kinji Asaka, Tetsuya Horiuchi, Gen Endo, Hiroyuki Nabae, and Koichi Suzumori. Ipmc monolithic thin film robots fabricated using a multi-layer casting process. *IEEE Robotics and Automation Letters*, 4(2):1335–1342, 4 2019. ISSN 23773766. doi: 10.1109/LRA.2019.2895398.
- [99] Yi Chu Chang and Won Jong Kim. Aquatic ionic-polymer-metal-composite insectile robot with multi-dof legs. *IEEE/ASME Transactions on Mechatronics*, 18(2):547–555, April 2013. ISSN 10834435. doi: 10.1109/TMECH.2012.2210904.
- [100] Joel J. Hubbard, Maxwell Fleming, Viljar Palmre, David Pugal, Kwang J. Kim, and Kam K. Leang. Monolithic ipmc fins for propulsion and maneuvering in bioinspired underwater robotics. *IEEE Journal of Oceanic Engineering*, 39(3):540–551, July 2014. ISSN 03649059. doi: 10.1109/JOE.2013.2259318.
- [101] Jasim Khawwaf, Jinchuan Zheng, Hai Wang, and Zhihong Man. Practical model-free robust control design for an underwater ipmc actuator. In *2019 Chinese Control Conference (CCC)*, volume 2019-July, pages 3214–3219. IEEE Computer Society, 7 2019. ISBN 9789881563972. doi: 10.23919/ChiCC.2019.8866467.
- [102] E. Acome, S. K. Mitchell, T. G. Morrissey, M. B. Emmett, C. Benjamin, M. King, M. Radakovitz, and C. Keplinger. Hydraulically amplified self-healing electrostatic actuators with muscle-like performance. *Science*, 359(6371):61–65, 1 2018. ISSN 10959203. doi: 10.1126/science.aa06139. URL <http://science.sciencemag.org/>.
- [103] Christoph Keplinger, Tiefeng Li, Richard Baumgartner, Zhigang Suo, and Siegfried Bauer. Harnessing snap-through instability in soft dielectrics to achieve giant voltage-triggered deformation. *Soft Matter*, 8(2):285–288, 1 2012. ISSN 1744683X. doi: 10.1039/c1sm06736b. URL [www.rsc.org/advances](http://www.rsc.org/advances).
- [104] Charles Manion, Dinesh Patel, Mark Fuge, and Sarah Bergbrieter. Modeling and evaluation of additive manufacturedhasel actuators. n.d. URL [https://softcontrol.mit.edu/sites/default/files/documents/SRMCIROS18\\_paper\\_13.pdf](https://softcontrol.mit.edu/sites/default/files/documents/SRMCIROS18_paper_13.pdf).
- [105] Shane K Mitchell, Xingrui Wang, Eric Acome, Trent Martin, Khoi Ly, Nicholas Kellaris, Vidyacharan Gopaluni Venkata, and Christoph Keplinger. An easy-to-implement toolkit to create versatile and high-performance hasel actuators for untethered soft robots. *Advanced Science*, 6(14):1900178, 7 2019. ISSN 2198-3844. doi: 10.1002/advs.201900178. URL <https://doi.org/10.1002/advs.201900178>. doi: 10.1002/advs.201900178.

- [106] Yang Liu, Meng Gao, Shengfu Mei, Yanting Han, and Jing Liu. Ultra-compliant liquid metal electrodes with in-plane self-healing capability for dielectric elastomer actuators. *Applied Physics Letters*, 103:64101, 8 2013. ISSN 0003-6951. URL <https://ui.adsabs.harvard.edu/abs/2013ApPhL.103f4101L>.
- [107] John A Rogers. A clear advance in soft actuators. *Science*, 341:968–969, 8 2013. ISSN 0036-8075. URL <https://ui.adsabs.harvard.edu/abs/2013Sci...341..968R>.
- [108] A Bele, C Tugui, M Asandulesa, D Ionita, L Vasiliu, G Stiubianu, M Iacob, C Racles, and M Cazacu. Conductive stretchable composites properly engineered to develop highly compliant electrodes for dielectric elastomer actuators. *Smart Materials and Structures*, 27(105005), 2018. URL <https://www.scopus.com/inward/record.uri?eid=2-s2.0-85054609457&doi=10.1088%2F1361-665X%2Faad977&partnerID=40&md5=37f280185c3e3f3c2bf1196fd522e256>. Cited By :1 Export Date: 8 May 2020.
- [109] Jose Enrico Q Quinsaat, Mihaela Alexandru, Frank A Nuesch, Heinrich Hofmann, Andreas Borgschulte, and Dorina M Opris. Highly stretchable dielectric elastomer composites containing high volume fractions of silver nanoparticles. *Journal of Materials Chemistry A*, 3(28):14675–14685, 2015. ISSN 2050-7488. URL <http://dx.doi.org/10.1039/C5TA03122B>.
- [110] S. Hau, G. Rizzello, and S. Seelecke. A novel dielectric elastomer membrane actuator concept for high-force applications. *Extreme Mechanics Letters*, 23:24–28, 2018. ISSN 2352-4316. URL <http://www.sciencedirect.com/science/article/pii/S2352431618301019>.
- [111] G. Kovacs, L. During, S. Michel, and G. Terrasi. Stacked dielectric elastomer actuator for tensile force transmission. *Sensors and Actuators A: Physical*, 155(2):299–307, 2009. ISSN 0924-4247. URL <http://www.sciencedirect.com/science/article/pii/S0924424709004002>.
- [112] F. Carpi and D. De Rossi. Small-strain modeling of helical dielectric elastomer actuators. *IEEE/ASME Transactions on Mechatronics*, 17(5706367):318–325, 2012. URL <https://www.scopus.com/inward/record.uri?eid=2-s2.0-84856316362&doi=10.1109%2fTMECH.2010.2100403&partnerID=40&md5=8aa3bd1f53656c405a8280ab884c829f>.
- [113] S. Pfeil, K. Katzer, A. Kanan, J. Mersch, M. Zimmermann, M. Kaliske, and G. Gerlach. A biomimetic fish fin-like robot based on textile reinforced silicone. *Micromachines*, 11(298):1–16, 2020. URL <https://www.scopus.com/inward/record.uri?eid=2-s2.0-85082725099&doi=10.3390%2fmci11030298&partnerID=40&md5=db2d25c45e87089b0ce501ad2e885d2a>.
- [114] M. Ghilardi, H. Boys, P. Torok, J. J. C. Busfield, and F. Carpi. Smart lenses with electrically tuneable astigmatism. *Scientific Reports*, 9(16127), 2019. URL <https://www.scopus.com/inward/record.uri?eid=2-s2.0-85074625641&doi=10.1038%2fs41598-019-52168-8&partnerID=40&md5=8fc861d90be73fbb8e0c212a2800ca84>.
- [115] H. Amin and S. F. M. Assal. Design methodology of a spring roll dielectric elastomer-based actuator for a hand rehabilitation system. In *2018 IEEE International Conference on Mechatronics and Automation (ICMA)*, pages 997–1002, 2018.
- [116] J. H. Park, A. El Atrache, D. Kim, and E. Divo. Optimization of helical dielectric elastomer actuator with additive manufacturing. volume 10594, 2018. URL <https://www.scopus.com/inward/record.uri?eid=2-s2.0-85050800758&doi=10.1117%2f12.2296720&partnerID=40&md5=89fe2bcddc403d953bb74c5cee2acad0>.

- [117] David McCoul, Samuel Rosset, Samuel Schlatter, and Herbert Shea. Inkjet 3d printing of uv and thermal cure silicone elastomers for dielectric elastomer actuators. *Smart Materials and Structures*, 26(12):125022, 2017. ISSN 1361665X. doi: 10.1088/1361-665X/aa9695. URL <http://dx.doi.org/10.1088/1361-665X/aa9695>.
- [118] K. Jung, K. J. Kim, and H. R. Choi. A self-sensing dielectric elastomer actuator. *Sensors and Actuators, A: Physical*, 143(2):343–351, 2008. URL <https://www.scopus.com/inward/record.uri?eid=2-s2.0-41349085167&doi=10.1016%2fj.sna.2007.10.076&partnerID=40&md5=93777dd3b85b4884763060bebeab2b4b>.
- [119] N. C. Goulbourne, E. M. Mockensturm, and M. I. Frecker. Electro-elastomers: Large deformation analysis of silicone membranes. *International Journal of Solids and Structures*, 44(9):2609–2626, 2007. ISSN 0020-7683. URL <http://www.sciencedirect.com/science/article/pii/S002076830600312X>.
- [120] Mark R Jolly, J David Carlson, Beth C Munoz, and Todd A Bullions. The magnetoviscoelastic response of elastomer composites consisting of ferrous particles embedded in a polymer matrix. *Journal of Intelligent Material Systems and Structures*, 7(6):613–622, 11 1996. ISSN 1045-389X. doi: 10.1177/1045389X9600700601. URL <https://doi.org/10.1177/1045389X9600700601>. doi: 10.1177/1045389X9600700601.
- [121] Holger Bose, Raman Rabindranath, and Johannes Ehrlich. Soft magnetorheological elastomers as new actuators for valves. *Journal of Intelligent Material Systems and Structures*, 23(9):989–994, 1 2012. ISSN 1045-389X. doi: 10.1177/1045389x11433498. URL <https://doi.org/10.1177/1045389X11433498>. doi: 10.1177/1045389X11433498.
- [122] Nurul Liyana Burhannuddin, Nur Azmah Nordin, Saiful Amri Mazlan, Siti Aishah Abdul Aziz, Seung Bok Choi, Noriyuki Kuwano, Nurhazimah Nazmi, and Norhasnidawani Johari. Effects of corrosion rate of the magnetic particles on the field-dependent material characteristics of silicone based magnetorheological elastomers. *Smart Materials and Structures*, 29, 8 2020. ISSN 1361665X. doi: 10.1088/1361-665X/AB972C.
- [123] Qi Ge, Zhiqin Li, Zhaolong Wang, Kavin Kowsari, Wang Zhang, Xiangnan He, Jianlin Zhou, and Nicholas X. Fang. Projection micro stereolithography based 3d printing and its applications. *International Journal of Extreme Manufacturing*, 2:022004, 6 2020. ISSN 2631-7990. doi: 10.1088/2631-7990/AB8D9A. URL <https://iopscience.iop.org/article/10.1088/2631-7990/ab8d9a> <https://iopscience.iop.org/article/10.1088/2631-7990/ab8d9a/meta>.
- [124] Mohammadreza Lalegani Dezaki and Mahdi Bodaghi. Magnetorheological elastomer-based 4d printed electroactive composite actuators. *Sensors and Actuators A: Physical*, 349:114063, 1 2023. ISSN 0924-4247. doi: 10.1016/J.SNA.2022.114063.
- [125] Hannes Krueger, Mohammad Vaezi, and Shoufeng Yang. 3d printing of magnetorheological elastomers(mres)smart materials. volume 0, pages 213–218. Pro-AM, May 2014. ISBN 9789810904463. doi: 10.3850/978-981-09-0446-3\_088.
- [126] Yakub F. Ismail M. A. Unuh H, Muhamad P and Z. Tanasta. Experimental validation to a prototype magnetorheological (mr) semi-active damper for c-class vehicle. *IJAME*, 16(3):7034–7047, 2019.
- [127] Bing Chen, Xuan Zhao, Hao Ma, Ling Qin, and Wei-Hsin Liao. Design and characterization of a magneto-rheological series elastic actuator for a lower extremity exoskeleton. *Smart Materials and Structures*, 26(10):105008, 2017. ISSN 1361-665X. URL <http://dx.doi.org/10.1088/1361-665X/aa8343>.

- [128] Gregory J. Hiemenz, Young Tai Choi, and Norman M. Wereley. Semi-active control of vertical stroking helicopter crew seat for enhanced crashworthiness. *Journal of Aircraft*, 44(3):1031–1034, 5 2007. ISSN 15333868. doi: 10.2514/1.26492. URL <https://arc.aiaa.org/doi/abs/10.2514/1.26492>.
- [129] D. D.L. Chung. A critical review of piezoresistivity and its application in electrical-resistance-based strain sensing. *Journal of Materials Science* 2020 55:32, 55:15367–15396, 8 2020. ISSN 1573-4803. doi: 10.1007/S10853-020-05099-Z. URL <https://link.springer.com/article/10.1007/s10853-020-05099-z>.
- [130] Manuela Hindermann Bischoff and Françoise Ehrburger-Dolle. Electrical conductivity of carbon black–polyethylene composites: Experimental evidence of the change of cluster connectivity in the ptc effect. *Carbon*, 39:375–382, 3 2001. ISSN 0008-6223. doi: 10.1016/S0008-6223(00)00130-5.
- [131] Hwa Kim, Kwangsik Park, and Moo Yeol Lee. Biocompatible dispersion methods for carbon black. *Toxicological Research*, 28:209, 12 2012. ISSN 19768257. doi: 10.5487/TR.2012.28.4.209. URL [/pmc/articles/PMC3834425/](https://www.ncbi.nlm.nih.gov/pmc/articles/PMC3834425/)?report=abstract<https://www.ncbi.nlm.nih.gov/pmc/articles/PMC3834425/>.
- [132] Abhinav Priyadarshi, Mohammad Khavari, Tungky Subroto, Paul Prentice, Koulis Pericleous, Dmitry Eskin, John Durodola, and Iakovos Tzanakis. Mechanisms of ultrasonic de-agglomeration of oxides through in-situ high-speed observations and acoustic measurements. *Ultrasonics Sonochemistry*, 79:1350–4177, 11 2021. ISSN 18732828. doi: 10.1016/J.ULTSONCH.2021.105792. URL [/pmc/articles/PMC8524947/](https://www.ncbi.nlm.nih.gov/pmc/articles/PMC8524947/)?report=abstract<https://www.ncbi.nlm.nih.gov/pmc/articles/PMC8524947/>.
- [133] Olga Kudryashova, Alexander Vorozhtsov, and Pavel Danilov. Deagglomeration and coagulation of particles in liquid metal under ultrasonic treatment. 44:543–549, 2019. doi: 10.24425/aoa.2019.129269.
- [134] Sen Chen, Hong Zhang Wang, Rui Qi Zhao, Wei Rao, and Jing Liu. Liquid metal composites. *Matter*, 2:1446–1480, 6 2020. ISSN 25902385. doi: 10.1016/J.MATT.2020.03.016/ASSET/C68E26BB-43B4-42B7-A3E9-03E41C92A992/MAIN.ASSETS/GR8.JPG. URL <http://www.cell.com/article/S2590238520301296/fulltext>?report=abstract[https://www.cell.com/matter/abstract/S2590-2385\(20\)30129-6](https://www.cell.com/matter/abstract/S2590-2385(20)30129-6).
- [135] Sven Pegel, Petra Pötschke, Gudrun Petzold, Ingo Alig, Sergej M. Dudkin, and Dirk Lellinger. Dispersion, agglomeration, and network formation of multiwalled carbon nanotubes in polycarbonate melts. *Polymer*, 49:974–984, 2 2008. ISSN 0032-3861. doi: 10.1016/J.POLYMER.2007.12.024.
- [136] Samuel Rosset, Oluwaseun A. Ararom, Samuel Schlatter, and Herbert R. Shea. Fabrication process of silicone-based dielectric elastomer actuators. *Journal of Visualized Experiments*, page 53423, 2 2016. ISSN 1940087X. doi: 10.3791/53423. URL [www.jove.com?url=https://www.jove.com/video/53423](https://www.jove.com?url=https://www.jove.com/video/53423).
- [137] Chaima Fekiri, Ho Chan Kim, and In Hwan Lee. 3d-printable carbon nanotubes-based composite for flexible piezoresistive sensors. *Materials*, 13:1–12, 12 2020. doi: 10.3390/MA13235482.
- [138] A. K. Bastola, M. Paudel, and L. Li. Development of hybrid magnetorheological elastomers by 3d printing. *Polymer*, 149:213–228, 8 2018. ISSN 00323861. doi: 10.1016/j.polymer.2018.06.076.

- [139] Samta Sapra, Aniket Chakraborty, Suresh Nuthalapati, Anindya Nag, David W. Inglis, Subhas Chandra Mukhopadhyay, and Mehmet Ercan Altinsoy. Printed, wearable e-skin force sensor array. *Measurement*, 206:112348, 1 2023. ISSN 0263-2241. doi: 10.1016/J.MEASUREMENT.2022.112348.
- [140] Ming Li, Sujie Chen, Boyu Fan, Bangyuan Wu, and Xiaojun Guo. Printed flexible strain sensor array for bendable interactive surface. *Advanced Functional Materials*, 30:2003214, 8 2020. ISSN 16163028. doi: 10.1002/adfm.202003214. URL <https://onlinelibrary-wiley-com.ezproxy.canterbury.ac.nz/doi/full/10.1002/adfm.202003214> <https://onlinelibrary-wiley-com.ezproxy.canterbury.ac.nz/doi/abs/10.1002/adfm.202003214> <https://onlinelibrary-wiley-com.ezproxy.canterbury.ac.nz/doi/10.1002/adfm.2020>.
- [141] Jianan Yi, Frank Babick, Carsten Strobel, Samuel Rosset, Luca Ciarella, Dmitry Borin, Katherine Wilson, Iain Anderson, Andreas Richter, and E. F. Markus Henke. Characterizations and inkjet printing of carbon black electrodes for dielectric elastomer actuators. *ACS Applied Materials and Interfaces*, 15:41992–42003, 9 2023. ISSN 19448252. doi: 10.1021/ACSAM.3C05444/ASSET/IMAGES/LARGE/AM3C05444\_0009.JPG. URL <https://pubs.acs.org/doi/full/10.1021/acsam.3c05444>.
- [142] Daewon Kim, Jang Ho Park, Eduardo Divo, and Abdullah El Atrache. Optimization of helical dielectric elastomer actuator with additive manufacturing. volume 10594, page 32. SPIE, 3 2018. ISBN 9781510616844. doi: 10.1117/12.2296720. URL <https://www.spiedigitallibrary.org/conference-proceedings-of-spie/10594/2296720/Optimization-of-helical-dielectric-elastomer-actuator-with-additive-manufacturing/10.1117/12.2296720.full>.
- [143] Jeong Hun Kim, Ji Young Hwang, Ha Ryeon Hwang, Han Seop Kim, Joong Hoon Lee, Jae Won Seo, Ueon Sang Shin, and Sang Hoon Lee. Simple and cost-effective method of highly conductive and elastic carbon nanotube/polydimethylsiloxane composite for wearable electronics. *Scientific Reports*, 8:54853, 12 2018. ISSN 20452322. doi: 10.1038/s41598-017-18209-w. URL [www.nature.com/scientificreports.](http://www.nature.com/scientificreports/)
- [144] Bettina Fasolt, Micah Hodgins, Gianluca Rizzello, and Stefan Seelecke. Effect of screen printing parameters on sensor and actuator performance of dielectric elastomer (de) membranes. *Sensors and Actuators A: Physical*, 265:10–19, 10 2017. ISSN 0924-4247. doi: 10.1016/J.SNA.2017.08.028.
- [145] Di Wu, Mengni Wei, Rong Li, Tao Xiao, Shen Gong, Zhu Xiao, Zhenghong Zhu, and Zhou Li. A percolation network model to predict the electrical property of flexible cnt/pdms composite films fabricated by spin coating technique. *Composites Part B: Engineering*, 174:107034, 2019. ISSN 13598368. doi: 10.1016/j.compositesb.2019.107034.
- [146] L. Flandin, J. Y. Cavaille, Y. Brechet, and R. Dendievel. Characterization of the damage in nanocomposite materials by a.c. electrical properties: experiment and simulation. *Journal of Materials Science*, 34:1753–1759, 4 1999. ISSN 1573-4803. doi: 10.1023/A:1004546806226. URL <https://link.springer.com/article/10.1023/A:1004546806226>.
- [147] Pan Song and Yong Zhang. Vertically aligned carbon nanotubes/graphene/cellulose nanofiber networks for enhancing electrical conductivity and piezoresistivity of silicone rubber composites. *Composites Science and Technology*, 222:109366, 5 2022. ISSN 0266-3538. doi: 10.1016/J.COMPSCITECH.2022.109366.

- [148] Melika Eklund and Nellie Kjäll. Silicone-based carbon black composite for epidermal electrodes. 12 2019. URL <http://uu.diva-portal.org/smash/get/diva2:1384429/FULLTEXT02.pdf>.
- [149] Yuanzhen Wang, Chensheng Xu, Timotheus Jahnke, Wolfgang Verestek, Siegfried Schmauder, and Joachim P. Spatz. Microstructural modeling and simulation of a carbon black-based conductive polymer - a template for the virtual design of a composite material. *ACS Omega*, 7:28820–28830, 8 2022. ISSN 24701343. doi: 10.1021/AC SOME GA.2C01755/ASSET/IMAGES/LARGE/AO2C01755\_0009.JPEG. URL <https://pubs.acs.org/doi/full/10.1021/acsomega.2c01755>.
- [150] R. Neffati and J. M.C. Brokken-Zijp. Electric conductivity in silicone-carbon black nanocomposites: percolation and variable range hopping on a fractal. *Materials Research Express*, 6:125058, 11 2019. ISSN 2053-1591. doi: 10.1088/2053-1591/AB58FD. URL <https://iopscience.iop.org/article/10.1088/2053-1591/ab58fdhttps://iopscience.iop.org/article/10.1088/2053-1591/ab58fd/meta>.
- [151] D. Bloor, A. Graham, E. J. Williams, P. J. Laughlin, and D. Lussey. Metal-polymer composite with nanostructured filler particles and amplified physical properties. *Applied Physics Letters*, 88:102103, 3 2006. ISSN 00036951. doi: 10.1063/1.2183359/902621. URL [/aip/apl/article/88/10/102103/902621/Metal-polymer-composite-with-nanostructured-filler](https://aip.org/doi/10.1063/1.2183359/902621).
- [152] Lingyan Duan, Sirui Fu, Hua Deng, Qin Zhang, Ke Wang, Feng Chen, and Qiang Fu. The resistivity-strain behavior of conductive polymer composites: stability and sensitivity. *Journal of Materials Chemistry A*, 2: 17085–17098, 9 2014. ISSN 2050-7496. doi: 10.1039/C4TA03645J. URL <https://pubs.rsc.org/en/content/articlehtml/2014/ta/c4ta03645jhttps://pubs.rsc.org/en/content/articlelanding/2014/ta/c4ta03645j>.
- [153] Rui Zhang, Mark Baxendale, and Ton Peijs. Universal resistivity-strain dependence of carbon nanotube/polymer composites. *Physical Review B - Condensed Matter and Materials Physics*, 76:195433, 11 2007. ISSN 10980121. doi: 10.1103/PHYSREVB.76.195433/FIGURES/6/MEDIUM. URL <https://journals.aps.org/prb/abstract/10.1103/PhysRevB.76.195433>.
- [154] Leonel P. Madrid, Carlos A. Palacio, Arnaldo Matute, and Carlos A. Parra Vargas. Underlying physics of conductive polymer composites and force sensing resistors (fsrs) under static loading conditions. *Sensors (Basel, Switzerland)*, 17, 9 2017. ISSN 14248220. doi: 10.3390/S17092108. URL [/pmc/articles/PMC5621037//pmc/articles/PMC5621037/?report=abstracthttps://www.ncbi.nlm.nih.gov/pmc/articles/PMC5621037/](https://www.ncbi.nlm.nih.gov/pmc/articles/PMC5621037/?report=abstracthttps://www.ncbi.nlm.nih.gov/pmc/articles/PMC5621037/).
- [155] Ning Hu, Yoshifumi Karube, Cheng Yan, Zen Masuda, and Hisao Fukunaga. Tunneling effect in a polymer/carbon nanotube nanocomposite strain sensor. *Acta Materialia*, 56: 2929–2936, 8 2008. ISSN 1359-6454. doi: 10.1016/J.ACTAMAT.2008.02.030.
- [156] C. Grimaldi and I. Balberg. Tunneling and nonuniversality in continuum percolation systems. *Physical Review Letters*, 96:066602, 2 2006. ISSN 10797114. doi: 10.1103/PHYSREVLETT.96.066602/FIGURES/2/MEDIUM. URL <https://journals.aps.org/prl/abstract/10.1103/PhysRevLett.96.066602>.
- [157] M Lacasse, V Duchaine, and C Gosselin. Characterization of the electrical resistance of carbon-black-filled silicone: Application to a flexible and stretchable robot skin. pages 4842–4848, 5 2010. doi: 10.1109/ROBOT.2010.5509283.

- [158] E. F.M. Henke, Katherine E. Wilson, and I. A. Anderson. Modeling of dielectric elastomer oscillators for soft biomimetic applications. *Bioinspiration and Biomimetics*, 13:046009, 6 2018. ISSN 17483190. doi: 10.1088/1748-3190/aac911. URL <https://doi.org/10.1088/1748-3190/aac911>.
- [159] Yanju Liu, Liwu Liu, Zhen Zhang, and Jinsong Leng. Dielectric elastomer film actuators: Characterization, experiment and analysis. *Smart Materials and Structures*, 18:095024, 7 2009. ISSN 09641726. doi: 10.1088/0964-1726/18/9/095024. URL <https://iopscience-iop-org.ezproxy.canterbury.ac.nz/article/10.1088/0964-1726/18/9/095024><https://iopscience-iop-org.ezproxy.canterbury.ac.nz/article/10.1088/0964-1726/18/9/095024/meta>.
- [160] Federico Carpi, Stanisa Raspovic, Gabriele Frediani, and Danilo De Rossi. Real-time control of dielectric elastomer actuators via bioelectric and biomechanical signals. *Polymer International*, 59:422–429, 3 2010. ISSN 09598103. doi: 10.1002/pi.2757. URL <http://doi.wiley.com/10.1002/pi.2757>.
- [161] Yasuhiro Mouri, Yuta Murai, Yoshiko Yabuki, Takumi Kato, Hideki Ohmae, Yoshihiro Tomita, Shunta Togo, Yinlai Jiang, and Hiroshi Yokoi. Development of new flexible dry electrode for myoelectric sensor using conductive silicone. pages 478–482. Institute of Electrical and Electronics Engineers Inc., 1 2019. ISBN 9781538673553. doi: 10.1109/CBS.2018.8612280. URL <https://ieeexplore-ieee-org.ezproxy.canterbury.ac.nz/document/8612280>.
- [162] S. L. Wang, P. Wang, and T. H. Ding. Development of wireless compressive/relaxation-stress measurement system integrated with pressure-sensitive carbon black-filled silicone rubber-based sensors. *Sensors and Actuators, A: Physical*, 157:36–41, 1 2010. ISSN 09244247. doi: 10.1016/j.sna.2009.11.037.
- [163] VishayPG. Strain gage selection: Criteria, procedures, recommendations - tech note, 5 2018. URL [www.micro-measurements.com](http://www.micro-measurements.com).
- [164] Dinesh Maddipatla, Binu B. Narakathu, Mohammed M. Ali, Amer A. Chlaihawi, and Massood Z. Atashbar. Development of a novel carbon nanotube based printed and flexible pressure sensor. Institute of Electrical and Electronics Engineers Inc., 4 2017. ISBN 9781509032020. doi: 10.1109/SAS.2017.7894034.
- [165] Luheng Wang and Yanyan Han. Compressive relaxation of the stress and resistance for carbon nanotube filled silicone rubber composite. *Composites Part A: Applied Science and Manufacturing*, 47:63–71, 4 2013. ISSN 1359835X. doi: 10.1016/j.compositesa.2012.11.018.
- [166] C Racles, M Asandulesa, V Tiron, C Tugui, N Vornicu, Ciubotaru B, M Mičušík, M Omastova, A Vasiliu, and C Ciomaga. Elastic composites with pdms matrix and polysulfone-supported silver nanoparticles as filler. *Polymer*, 217, 3 2021. URL <https://www-scopus-com.ezproxy.canterbury.ac.nz/record/display.uri?eid=2-s2.0-85100376139&origin=resultslist&sort=plf-f&src=s&st1=&st2=&sid=f91c46950ff68c208c50319781176f3e&sot=b&sdt=b&sl=37&s=TITLE-ABS-KEY+%28metal+silicone+sensor%29&relpos=4&citeCnt=0&s>.
- [167] Shoji Fukushima, Tatsuya Kasai, Yumi Umeda, Makoto Ohnishi, Toshiaki Sasaki, and Michiharu Matsumoto. Carcinogenicity of multi-walled carbon nanotubes: Challenging issue on hazard assessment. *Journal of Occupational Health*, 60:10–30, 2018. ISSN 13489585. doi: 10.1539/joh.17-0102-RA. URL <https://doi.org/10.1539/joh.17-0102-RA>.

[/pmc/articles/PMC5799097//pmc/articles/PMC5799097/?report=abstract](https://www.ncbi.nlm.nih.gov/pmc/articles/PMC5799097/?report=abstract)<https://www.ncbi.nlm.nih.gov/pmc/articles/PMC5799097/>.

- [168] Zannatul Ferdous and Abderrahim Nemmar. Health impact of silver nanoparticles: A review of the biodistribution and toxicity following various routes of exposure. *International Journal of Molecular Sciences*, 21, 4 2020. ISSN 14220067. doi: 10.3390/ijms21072375. URL [/pmc/articles/PMC7177798//pmc/articles/PMC7177798/?report=abstract](https://www.ncbi.nlm.nih.gov/pmc/articles/PMC7177798/?report=abstract)<https://www.ncbi.nlm.nih.gov/pmc/articles/PMC7177798/>.
- [169] L. J. Rausch, E. C. Bisinger, and A. Sharma. Carbon black should not be classified as a human carcinogen based on rodent bioassay data. *Regulatory Toxicology and Pharmacology*, 40:28–41, 8 2004. ISSN 02732300. doi: 10.1016/j.yrtph.2004.04.004.
- [170] Tim Giffney, Estelle Bejanin, Agee S. Kurian, Jadranka Travas-Sejdic, and Kean Aw. Highly stretchable printed strain sensors using multi-walled carbon nanotube/silicone rubber composites. *Sensors and Actuators, A: Physical*, 259:44–49, 6 2017. ISSN 09244247. doi: 10.1016/j.sna.2017.03.005.
- [171] Harish Devaraj, Tim Giffney, Adeline Petit, Mahtab Assadian, and Kean Aw. The development of highly flexible stretch sensors for a robotic hand. *Robotics*, 7, 9 2018. ISSN 22186581. doi: 10.3390/robotics7030054.
- [172] J Kost, A Foux, and M Narkis. Quantitative model relating electrical resistance, strain, and time for carbon black loaded silicone rubber - proquest. *Polymer Engineering and Science*, 34:1628, 11 1994. ISSN 00323888. URL <https://search-proquest-com.ezproxy.canterbury.ac.nz/docview/218606740/citation/EA6C174C0ED84FDAPQ/1?accountid=14499>.
- [173] Peng Wang, Feng Xu, Ding Tianhuai, and Qin Yuanzhen. Time dependence of electrical resistivity under uniaxial pressures for carbon black/polymer composites. *Journal of Materials Science*, 39:4937–4939, 2004. URL <http://search.proquest.com.ezproxy.canterbury.ac.nz/docview/2259673740?accountid=14499>. |b|From Duplicate 4 (|j|Time dependence of electrical resistivity under uniaxial pressures for carbon black/polymer composites|i| - Wang, Peng; Xu, Feng; Tianhuai, Ding; Yuanzhen, Qin)|br|/i|/b|/br/|b|Copyright - Journal of Materials Science is a copyright of Springer, (2004). All Rights Reserved; Last updated - 2019-07-19.
- [174] Johannes Mersch, Hans Winger, Andreas Nocke, Chokri Cherif, and Gerald Gerlach. Experimental investigation and modeling of the dynamic resistance response of carbon particle-filled polymers. *Macromolecular Materials and Engineering*, 305, 10 2020. ISSN 14392054. doi: 10.1002/MAME.202000361.
- [175] Laaraibi Abdo-Rahmane Anas, Guruvan Jodin, Damien Hoareau, Nicolas Bideau, and Florence Razan. Flexible dynamic pressure sensor for insole based on inverse viscoelastic model — enhanced reader. *IEEE Sensors Journal*, 7:7634–7643, 4 2023.
- [176] SmoothOn. Dragon skin™ 10 nv product information — smooth-on, inc., 2 2021. URL <https://www.smooth-on.com/products/dragon-skin-10-nv/>.
- [177] ASTM. D412-16 standard test methods for vulcanized rubber and thermoplastic elastomers—tension, 2020. URL [https://compass.astm.org/EDIT/html\\_annot.cgi?D412+16](https://compass.astm.org/EDIT/html_annot.cgi?D412+16).
- [178] I. D. Johnston, D. K. McCluskey, C. K.L. Tan, and M. C. Tracey. Mechanical characterization of bulk sylgard 184 for microfluidics and microengineering. *Journal of Micromechanics and Microengineering*, 24:035017,

- 2 2014. ISSN 0960-1317. doi: 10.1088/0960-1317/24/3/035017. URL <https://iopscience.iop.org/article/10.1088/0960-1317/24/3/035017> <https://iopscience.iop.org/article/10.1088/0960-1317/24/3/035017/meta>.
- [179] Yuhong Wu, Frederick J. McGarry, Bisheng Zhu, John R. Keryk, and Dimitris E. Katsoulis. Temperature effect on mechanical properties of toughened silicone resins. *Polymer Engineering Science*, 45:1522–1531, 11 2005. ISSN 1548-2634. doi: 10.1002/PEN.20423. URL <https://onlinelibrary.wiley.com/doi/full/10.1002/pen.20423> <https://onlinelibrary.wiley.com/doi/abs/10.1002/pen.20423> <https://4spepublications.onlinelibrary.wiley.com/doi/10.1002/pen.20423>.
- [180] Jie Luo. Machining of elastomers. 2005.
- [181] Miroslawa Pawlyta, Jean Noël Rouzaud, and Stanislaw Duber. Raman microspectroscopy characterization of carbon blacks: Spectral analysis and structural information. *Carbon*, 84:479–490, 4 2015. ISSN 0008-6223. doi: 10.1016/J.CARBON.2014.12.030.
- [182] RamanLife. Pdms raman spectrum — raman for life, 2024. URL <https://ramanlife.com/library/pdms-raman/>.
- [183] Hui Xu, Li Xiu Gong, Xu Wang, Li Zhao, Yong Bing Pei, Gang Wang, Ya Jun Liu, Lian Bin Wu, Jian Xiong Jiang, and Long Cheng Tang. Influence of processing conditions on dispersion, electrical and mechanical properties of graphene-filled-silicone rubber composites. *Composites Part A: Applied Science and Manufacturing*, 91:53–64, 12 2016. ISSN 1359835X. doi: 10.1016/j.compositesa.2016.09.011.